

**Different Strategies to Improve Drug Tissue Selectivity for Better  
Efficacy/Toxicity Profile**

by

**Hongxiang Hu**

A dissertation submitted in partial fulfillment  
of the requirements for the degree of  
Doctor of Philosophy  
(Pharmaceutical Sciences)  
in The University of Michigan  
2022

Doctoral Committee:

Professor Duxin Sun, Chair  
Associate Professor Wei Cheng  
Associate Professor James Moon  
Professor Shaomeng Wang

Hongxiang Hu

[hongxhu@umich.edu](mailto:hongxhu@umich.edu)

ORCID iD: [0000-0002-6221-7462](https://orcid.org/0000-0002-6221-7462)

© Hongxiang Hu 2022

## **DEDICATION**

*For my mother,  
Thank you for always considering the worst scenarios for me.  
I know that even if I fail everything, I am still valuable to you.*

## ACKNOWLEDGMENTS

Firstly, I would like to express my sincere gratitude towards my advisor, Dr. Duxin Sun, for his continuous support and guidance during my doctoral program at the University of Michigan. Dr. Sun, thank you for culturing my critical thinking skills and teaching me how to be an independent researcher. Your passion for science and care for students will always inspire me and benefits me all my life. It is my honor to be your student.

Besides, I would also like to recognize my dissertation committee members including Dr. Wei Cheng, Dr. James Moon and Dr. Shaomeng Wang. Thank you for providing valuable suggestions to my research and challenging me as a presenter. I especially want to thank your patience for my late data meeting during this special period.

I also want to acknowledge my lab mates for their incredible support to my work and life. Specially, I want to thank Wei Gao for her continuous guidance to my research and contributions on the nanomedicine and STR project; Mady Traore, Ruiting Li, Hebao Yuan and Miao He for their contributions on the MMT5-14 project; Lipeng Dai for his contributions on the STR project; Chengyi Li, Djibo Mahamadou, Hongwei Chen, Ryan Clauson, Yudong Song, Nathan Truchan, Yingzi Bu, Lu Wang, and other lab members for their help to my research and life. Thanks for all of you to accompany me through an important life journey and leave me a period of precious memories.

There are still many others I need to be grateful for. I want to thank my classmates, teachers, roommates, friends who played sports with me, heavy snow in Ann Arbor, squirrels who came for food every day and all other memorable things. I thank my life here.

## TABLE OF CONTENTS

DEDICATION .....	ii
ACKNOWLEDGMENTS .....	iii
LIST OF FIGURES .....	vi
LIST OF TABLES .....	ix
ABSTRACT .....	x
CHAPTER I – Introduction: Drug Tissue Selectivity Deserves More Attention .....	1
Bibliography .....	7
CHAPTER II - Nanomedicine of BCL-2/BCL-X <sub>L</sub> Inhibitors Improve Tissue Targeting, Reduce Platelet Toxicity and Enhance Anticancer Efficacy in Myeloproliferative Neoplasm and Lymphoma .....	10
2.1 Abstract .....	10
2.2 Introduction .....	10
2.3 Results and Discussion .....	12
2.4 Conclusion .....	18
2.5 Experimental Section .....	19
2.6 Figures and Tables .....	25
2.7 Bibliography .....	41
CHAPTER III – Drug Optimization of Anti-SARS-Cov-2 Candidate to Improve Lung Targeting and Enhance Efficacy in Treatment of COVID-19 .....	44
3.1 Abstract .....	44
3.2 Introduction .....	44
3.3 Result and Discussion .....	46
3.4 Conclusion .....	51
3.5 Experimental Section .....	51
3.6 Figures and Tables .....	60

3.7 Bibliography.....	70
CHAPTER IV - Structure-Tissue Exposure/Selectivity Relationship (STR) May Correlate with Dose-Dependent Clinical Efficacy/Safety .....	72
4.1 Abstract .....	72
4.2 Introduction .....	72
4.3 Results and Discussion.....	76
4.4 Conclusion.....	87
4.5 Experimental Section .....	88
4.6 Figures and Tables .....	90
4.7 Bibliography.....	115
CHAPTER V - Conclusions .....	120

## LIST OF FIGURES

Figure 1.1 – Drug discovery and development process .....	2
Figure 1.2 – Drug exposure in the plasma as a surrogate of therapeutic exposure in targeted tissue may mislead the selection of drug candidate to clinical trials .....	3
Figure 2.1 – High physicochemical stability of nano-1252 .....	26
Figure 2.2 – Nano-1252 decreased platelet toxicity due to fast distribution of formulation and limited generation of APG-1244 in circulation system .....	27
Figure 2.3 – Nano-1252 altered biodistribution pattern of clinical-1252 and enhanced spleen and BM selectivity .....	28
Figure 2.4 – Establishment of tumor model with disease progression occurred in spleen and BM.....	29
Figure 2.5 – Enhanced anti-tumor efficacy of nano-1252 in MPNs and mantle cell lymphoma mice model.....	30
Figure 2.S1 – Preparation and characterization of nano-1252.....	31
Figure 2.S2 – Low physical stability of abraxane and chemical stability of clinical-1252 .....	32
Figure 2.S3 – Microscope images of blood cells and platelets for clinical-1252 (a) and nano-1252 (b) at 4 hr or 24 hr.....	33
Figure 2.S4 – Complete blood count (CBC) analysis of clinical-1252 and nano-1252 ....	34
Figure 2.S5 – Tissue distribution of clinical-1252 and nano-1252.....	35
Figure 2.S6 – Tissue distribution of clinical-1252 and nano-1252 in fat pad, fat pad without lymph nodes (fat pad/wo LNs) and lymph nodes (LNs) .....	36
Figure 2.S7 – Confocal images of the fluorescent nano-1252 distribution in spleens from BALB/c mice, BALB/c mice depleted with macrophages and NOD SCID mice .....	37
Figure 2.S8 – Establishment of tumor model with disease progression in spleen and BM .....	39

Figure 2.S9 – Cytotoxicity of nano-1252 combined with other drugs against lymphoma or MPNs cell lines .....	40
Figure 3.1 – Synthesis of remdesivir analogs and their improved in-vitro and in-vivo stability.....	61
Figure 3.2 – MMT5-14 and MMT5-15 achieved higher drug concentration and active metabolite, NTP in blood and lung .....	62
Figure 3.3 – MMT5-14 not only increased tissue exposure but also increased the tissue selectivity of both prodrug and active metabolite NTP in the lung, spleen and blood ....	63
Figure 3.4 – MMT5-14 increased epithelial cells uptake and in-vitro antiviral activity .	64
Figure 3.S1 – Concentration-time profile in collected tissues from hamsters (n=2) after administration of remdesivir, MMT5-14_albumin or MMR5-14_CD .....	65
Figure 3.S2 – Average AUC of collected tissues from hamsters after administration of remdesivir, MMT5-14_albumin or MMT5-14_CD (10 mg/kg).....	68
Figure 3.S3 – Mean of weight change of hamsters after administration of MMT5-14_alubmin or MMT5-14_CD (10 mg/kg, QD for 9 days in total).....	69
Figure 4.1 – Drug exposure in the plasma was not correlated with drug exposure in the target tissue among seven SERMs with different or similar chemical structures .....	91
Figure 4.2 – Drug exposure in the tissue, not in the plasma, was correlated with drug clinical efficacy/safety .....	92
Figure 4.3 – Drug tissue selectivity is a critical parameter that tips the balance of dose-dependent efficacy/toxicity .....	93
Figure 4.4 – Slight structure modification altered drug exposure and selectivity in tissues despite similar exposure in the plasma .....	94
Figure 4.5 – Slight structure modification altered drug exposure and selectivity in both plasma and tissues .....	95
Figure 4.6 – An enhanced tumor accumulation of small molecular drug compared to normal tissue .....	96
Figure 4.7 – Molecular structure descriptors influence drug exposure in tissues .....	97
Figure 4.S1 – The concentration-time curve of 7 SERMS in 18 different tissues of MMTV-PyMT transgenic mice with spontaneous breast cancer .....	98



Figure 4.S2 – Tissue AUC of 7 SERMS in 18 different tissues of MMTV-PyMT transgenic mice with spontaneous breast cancer .....	99
Figure 4.S3 – Analysis the similarity of 7 SERMs .....	99
Figure 4.S4 – Slight structure modification altered drug exposure and selectivity in tissues for tamoxifen, toremifene, afimoxifene and droloxifene .....	100
Figure 4.S5 – Slight structure modification altered drug exposure and selectivity in tissues for lasofoxifene and nafoxidine .....	101
Figure 4.S6 – Univariate feature analysis of collected descriptors in different tissues from mice administered by iv and oral .....	102
Figure 5.1 – Summary of Chapter II .....	122
Figure 5.2 – Summary of Chapter III.....	123
Figure 5.3 – Summary of Chapter IV .....	124

## LIST OF TABLES

Table 3.1 – In-vitro stability half-life time for remdesivir and its analogs .....	69
Table 3.S1 – Average AUC of cellular uptake in Calu-3 and HUVEC cells after incubation with remdesivir or MMT5-14 (10 uM) during 2-12 hr .....	69
Table 4.1 – Summary of plasma and target tissues distribution kinetic parameters .....	103
Table 4.2 – Physicochemical properties among SERMs with similar structure .....	103
Table 4.S1 – Summary of the indications and status of 7 SERMs .....	104
Table 4.S2 – Clinical efficacy and adverse reactions of Toremifene (60 mg QD) and Tamoxifen (20 mg QD) in prevention of breast cancer (STAR trail).....	105
Table 4.S3 – Tissue AUC, ng·h/(ml or g), after oral administration of 7 SERMS on MMTV-PyMT transgenic mice with spontaneous breast cancer .....	106
Table 4.S4 – AUC <sub>tissue</sub> /AUC <sub>plasma</sub> ratio after oral administration of 7 SERMS on MMTV-PyMT transgenic mice with spontaneous breast cancer .....	107
Table 4.S5 – Comparison of 3-fold AUC of Raloxifene and AUC of Tamoxifen in fatpad, tumor and bone .....	107
Table 4.S6 – Comparison of 3-fold AUC of Toremifene and AUC of Tamoxifen in fatpad, tumor, liver, lung and stomach .....	107
Table 4.S7 – Tissue AUC, ng·h/(ml or g), after i.v administration of 7 SERMS on MMTV-PyMT transgenic mice with spontaneous breast cancer .....	108
Table 4.S8 – Descriptors collected from RDKit, an open-source cross-platform cheminformatics toolkit, among SERMs with similar structures .....	109

## ABSTRACT

Despite tremendous efforts being devoted to improving drug discovery and development, the clinical failure rate remains high (>90% phase I onwards), particularly due to efficacy and safety issues. Based on the current strategies, drug candidates with optimized pre-clinical efficacy or toxicity and favorable plasma pharmacokinetics (PK) parameters are preferred for clinical studies. However, drug plasma exposure is not sufficient to represent the in vivo behavior and may mislead the selection of drug candidates for clinical trials. Furthermore, the importance of drug tissue exposure or selectivity, which is related to drug accumulation in disease- or toxicity-related tissues, continues to be ignored. In this study, we attempted to improve drug discovery from the perspective of altering drug tissue exposure and selectivity. In the first project (Chapter II), an albumin-based nanoformulation was prepared for BCL-2/BCL-XL inhibitors to improve tissue targeting, reduce platelet toxicity, and enhance anticancer efficacy in myeloproliferative neoplasms (MPNs) and lymphoma. Since the BCL-XL pathway is critical to the survival of platelets in blood, dual BCL-2/BCL-XL inhibitors can cause rapid thrombocytopenia in the circulation system. By altering the formulation of the compound, we aimed to alter its biodistribution via 1) a lower exposure in the blood to reduce platelet toxicity, and 2) similar or even a higher exposure in the target tissues (spleen and bone marrow, BM) to maintain or increase its efficacy. Subsequently, an albumin-based nanoformulation was successfully developed; owing to its high formulation stability, large amounts of nanoparticles were trapped in the spleen and BM, resulting in their high accumulation in these tissues and low concentration in the circulation system. Nanomedicine comprising the BCL-2/BCL-XL inhibitor substantially decreased platelet toxicity, prolonged the survival rate, delayed paralysis occurrence, and reduced tumor infiltration in the spleen and BM compared to the clinical formulation. In the second project (Chapter III), the

anti-SARS-CoV-2 small molecule remdesivir was optimized to improve lung targeting and enhance its efficacy against COVID-19. Although approved by the FDA in October 2020, the controversial efficacy of remdesivir in several clinical studies (GS-US-540-5773, GS-US-540-5774, WHO Solidarity trial) limited its wide administration. To improve the clinical potential of remdesivir, we modified its structure to increase lung accumulation without altering its anti-viral activity. Our lead compound, MMT5-14, achieved a 200-fold higher parent drug concentration in the target tissues (e.g., lung) and approximately 5-fold higher amount of active form (triphosphate form) than remdesivir. Moreover, owing to its high chemical stability, MMT5-14 showed a 4- to 7-fold higher uptake by HUVECs and lung epithelial cells (Calu-3) than remdesivir, with 4- to 8-fold enhanced anti-SARS-CoV-2 activities in Vero-E6 cells survival assay and virus titer reduction assay. In the third project (Chapter IV), the structure-tissue exposure or selectivity relationship (STR) was studied using a series of selective estrogen receptor modulators (SERMs). Results showed that drug exposure in the plasma was not correlated with drug exposure in the target tissues (tumor, fatpad, and bone), which was associated with clinical efficacy and safety. A slight structural modification altered drug exposure and selectivity in tissues despite similar drug exposure in the plasma. The STR may be correlated with clinical efficacy and safety, which might impact the success rate of drug development. Overall, this study highlights the importance of employing tissue selectivity as a parameter in the early stages of drug discovery and development.

## **CHAPTER I – Introduction: Drug Tissue Selectivity Deserves More Attention**

**Clinical failure rate remained high (>90% Phase I onwards) during drug development.** Drug discovery and development processes comprise different steps, including target identification (disease model establishment, target identification, and target validation), compound screening (visual screening and high-throughput screening [HTS]), lead optimization and pre-clinical tests (structure-activity relationship [SAR], drug-like property analysis, solubility, permeability, adsorption, distribution, metabolism, excretion/ADME, plasma PK, efficacy, and toxicity), investigational new drug application (IND), clinical trials (Phase I, II, and III), and final submission to launch (Figure 1.1)<sup>1-3</sup>. To obtain the licensing approval for a new medicine, more than 10,000 candidates need to be screened at the initial drug discovery step, which requires an average of 10–15 years and 1–2 billion dollars<sup>1</sup>. Clinical studies are considered the most important step in confirming the dosage, efficacy, and toxicity of drugs in humans and take more than half of the effort (~1.5 year in Phase I, ~2.5 year in Phase II, ~2.5 year in Phase III), and cost (~15% in Phase I, ~21% in Phase II, ~26% in Phase III) in drug discovery and development<sup>1-3</sup>. However, more than 90% of drug candidates fail during clinical trials, and this low success probability remained unchanged during 2010–2017. After analysis of the clinical data in this period, efficacy (52%) and safety (24%) were found to be the two most important failure reasons<sup>4</sup>. This implies that some crucial aspects in the current strategy to select compounds for clinical trials have been overlooked, particularly those related to efficacy and safety issues.

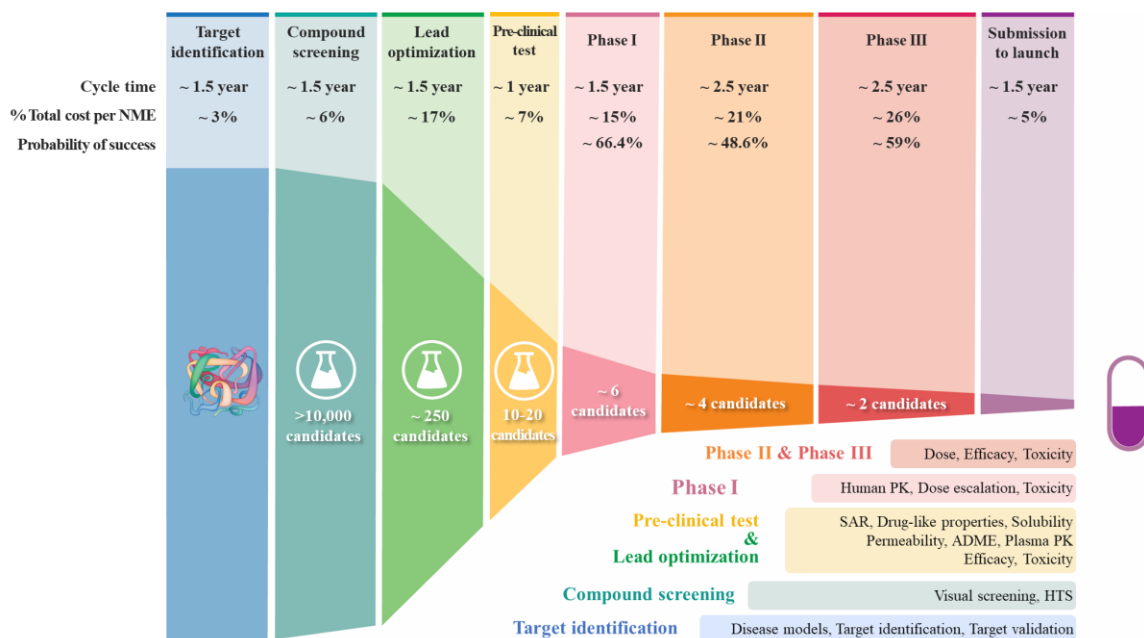


Figure 1.1 Drug discovery and development process. NME is abbreviated for new molecular entity, HTS for high throughput screening, SAR for structure-activity relationship, PK for pharmacokinetics and ADME for adsorption, distribution, metabolism, and excretion.

### **Drug candidates with optimized pre-clinical efficacy/toxicity and favorable plasma pk parameters are preferred in clinical studies.**

Based on the current strategy for selecting drug candidates for clinical trials, two major attributes of compounds are optimized to achieve 1) high specificity and potency against the target and 2) favorable drug-like properties, which are assessed on the basis of biopharmaceutics and PK (solubility, permeability, ADME/F, such as  $K_a$ , AUC,  $C_{max}$ , CL,  $T_{1/2}$ , and V)<sup>6,7</sup>. Tremendous efforts have been devoted to improving these two drug properties. The strategies used include virtual computation screening aided by artificial intelligence (AI) to select the best scaffold<sup>7-9</sup>; HTS (protein- or cell-based) to improve efficiency and specificity of hits; SAR analysis to obtain lead compounds with high affinity and specificity ( $K_i$  or  $IC_{50}$  in the level of nM or pM)<sup>3</sup>; genotoxicity studies to assess the carcinogenic potential<sup>10</sup>; “rule of 5” and biopharmaceutical classification system (BCS) to analyze drug-like properties<sup>6</sup>; preclinical pharmacokinetic studies to select clinical candidates with preferred bioavailability ( $F > 30\%$ ), half-life time ( $T_{1/2} > 4-6$  h) and clearance (CL,  $< 25\%$  hepatic blood flow Q)<sup>11</sup>. Drug candidates with a high plasma exposure and better plasma PK parameters are often selected for clinical studies, while

those with low exposure in the plasma are often eliminated without further development<sup>12</sup>.

**Drug plasma exposure is not sufficient to represent in vivo behavior and may mislead the selection of drug candidates for clinical trials.** The philosophy of using systemic exposure to predict the pharmacological effects is based on the well accepted “free drug hypothesis” assuming that the free drug concentration in tissues is equal to that in the plasma for permeable compounds at the pharmacokinetic steady state<sup>13, 14</sup>. However, this hypothesis can only be applied to a few small-molecule drugs, as various factors, such as membrane transporters, albumin-hitchhiking, and extracellular binding proteins, can cause asymmetric free drug distribution between the plasma and tissue<sup>15-17</sup>. Hence, systemic exposure as a driver of pharmacological effects has limited value in drug screening and optimization<sup>18</sup>. During drug optimization, drug candidates with high exposure in the plasma are often selected, which may have the desirable property of low elimination, or undesirable low tissue distribution that may result in low drug concentrations in the target tissues (Figure 1.2). In contrast, drugs with low plasma exposure are often eliminated, which may be due to their undesirable high elimination rates and low bioavailability, or high tissue distribution that may be preferred depending on the tissue exposure (Figure 1.2). Therefore, using pre-clinical plasma PK data to select drug candidates for clinical trials could be misleading; efficacy- or toxicity-related tissue exposure has been continuously overlooked and deserves more attention.

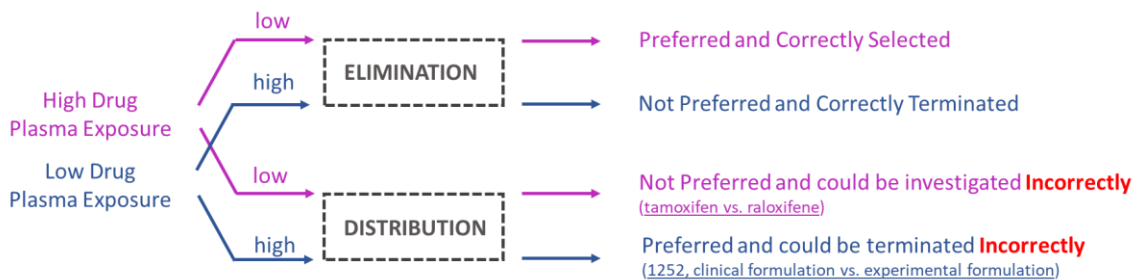


Figure 1.2. Drug exposure in the plasma as a surrogate of therapeutic exposure in targeted tissue may mislead the selection of drug candidate to clinical trials.

**Investigation of drug properties that influence tissue selectivity.** The purpose of my PhD studies was to investigate the importance of tissue selectivity in the drug discovery process and assess the properties of drugs that influence their distribution.

In the first example (Chapter II), we compared the tissue selectivity of different formulations of the same BCL-2/BCL-X<sub>L</sub> inhibitor, APG-1252. BCL2 family proteins (BCL-2 and BCL-X<sub>L</sub>) have been found to play important roles in the progression of lymphoma and myeloproliferative neoplasms<sup>19, 20</sup>. However, owing to the critical role of BCL-X<sub>L</sub> in the survival of platelets, BCL-2/BCL-X<sub>L</sub> inhibitors pose a risk of thrombocytopenia, which limits their clinical potential<sup>21, 22</sup>. APG-1252, as a new generation of BCL-2/BCL-X<sub>L</sub> inhibitors, is designed to have minimum selectivity to BCL-X<sub>L</sub> in the circulation system, but its selectivity increases after being metabolized in tissues<sup>23, 24</sup>. Although thrombocytopenia was relieved in clinical trials, APG-1252 caused a rapid reduction in platelet count at a high dosage (320 mg once per week)<sup>25</sup>. Unexpectedly, by changing the clinical formulation of APG-1252 (comprising surfactants such as PEG) to a nanoformulation, we observed a low blood/plasma exposure of the compound. The lower systemic exposure for the nanoformulation implied reduced platelet toxicity but also indicated that its efficacy could be limited due to a lower tissue exposure. However, in this case, we found that APG-1252 nanomedicine not only improved the safety of APG-1252 but also prolonged the survival rate, delayed paralysis occurrence, and reduced tumor infiltration in the spleen and BM compared to the clinical formulation. This could be attributed to different tissue selectivity. Even with a lower blood/plasma exposure, APG-1252 nanomedicine showed up to 20-fold higher accumulation in the target tissues such as the spleen and BM. This unique tissue distribution was further confirmed in different mouse species (BALB/c mice, BALB/c mice depleted of macrophages, and NOD SCID mice); we found that it was possibly caused by the mononuclear phagocyte systems (MPS) in these tissues. Confocal images of the spleen showed diffusive distribution of nanomedicine from the marginal zone to the red pulp and mantle cell zone. This example explains the importance of tissue selectivity investigation before clinical trials. Even for the same compound, a change in its formulation form could lead to different tissue accumulation patterns, which could be translated into its clinical efficacy or toxicity.



In the second experiment (Chapter III), we compared the tissue selectivity of similar antiviral molecules, remdesivir, and its analog, MMT5-14. Remdesivir, as the first anti-SARS-Cov-2 small molecule, was approved by the FDA in 2020<sup>26</sup> despite mediocre clinical results (GS-US-540-5773<sup>27</sup>, GS-US-540-5774<sup>28</sup>, and WHO Solidarity trial<sup>29</sup>). One of the major concerns about the unsatisfactory performance of remdesivir is its premature serum hydrolysis to nucleoside (NUC) metabolites such as GS-441524<sup>30</sup>. Remdesivir was initially designed to enhance cell permeability through the ProTide strategy (using phenol and L-alaninate ethylbutyl ester to cover the anionic phosphate moiety) and generate monophosphorylated nucleoside (NMP) using intracellular carboxyesterase 1 (CES 1) and phosphoramidases (HINT1-3)<sup>31, 32</sup>. Owing to the abundance of esterases and phosphatases in the serum, NUC is the predominant metabolite in the blood<sup>32, 33</sup>. Following the injection of remdesivir into nonhuman primates, the concentration of NUC in the serum was found to be over 100-fold higher than that of remdesivir<sup>32</sup>. The half-life of NUC, as assessed from its pharmacokinetic properties, in healthy adults was also over 20-fold higher than that of remdesivir (27 h vs. 1 h)<sup>32</sup>. The actual *in vivo* functioning compound NUC, instead of remdesivir, limited the formation of the pharmacologically active nucleoside triphosphate (NTP) metabolite GS-443902, leading to less potency against SARS-CoV-2. This finding made us wonder whether remdesivir analogs with increased stability can reduce the generation of NUC in the circulation system while generating more NTP *in vivo*. In this study, MMT5-14, our synthesized remdesivir analog, was selected for *in vivo* investigation because of its high stability in both plasma and liver microsomes from humans, hamsters, and mice. The blood/plasma exposure data demonstrated that MMT5-14 significantly delayed the degradation of prodrug and generated more NTP from the NMP pathway, with higher NTP concentrations in the blood. Our hypothesis seemed to match well with the results of blood/plasma exposure, and, based on this, higher NTP generation could be expected throughout the whole body. However, the tissue data did not meet our expectations, as a higher NTP exposure was only observed in the lungs, blood, and spleens from 23 samples. Further analysis revealed that the increased stability of MMT5-14 was generally unfavorable for NTP generation, and its high exposure in the blood, lung, and spleen was mainly caused by enhanced accumulation of the prodrug. Interestingly, in similar

compounds with different metabolic stability, different conclusions could be drawn depending on whether blood/plasma exposure only or composite tissue exposure was used. This is another example to demonstrate why blood/plasma exposure may mislead the selection of drug candidates for clinical trials. Lipid modification of antiviral drugs to increase metabolism stability has been shown to influence tissue distribution/selectivity.

In the third experiment (Chapter IV), we compared the tissue selectivity of different compounds with the same target i.e., selective estrogen receptor modulators (SERMs). SERMs are nonsteroidal indicators for breast cancer, osteoporosis, and menopausal symptoms<sup>34</sup>. We aimed to investigate the structure-tissue exposure or selectivity relationship (STR) using a series of SERMs with similar or different structures, molecular targets, and PK profiles in the plasma. We found that 1) in most cases, drug exposure in plasma was not correlated with drug exposure in the target tissues (tumor, fatpad, and bone); 2) drug exposure in tissues, not in the plasma, was correlated with drug clinical efficacy and safety. For instance, raloxifene showed more potent activity in the in vitro assays (ER binding affinity<sup>35</sup> and IC<sub>50</sub> against MCF-7/MDA-231 cells<sup>36</sup>) and similar drug exposure with tamoxifen while demonstrating lower anti-cancer efficacy (STAR trial); raloxifene is approved only for breast cancer prevention<sup>37</sup>. Such discrepancy would be more explainable if we consider the higher tissue selectivity that raloxifene showed in the target tissues, including tumors and fatpads; 3) slight structural changes altered drug tissue selectivity. Among the four SERMs with very similar chemical structures, tamoxifen, toremifene, afimoxifene, and droloxifene had similar drug exposure in the plasma or blood but distinct tissue exposure in most tissues, such as the brain, fat, fat pad, heart, intestine, kidney, liver, lung, muscle, pancreas, skin, spleen, stomach, tumor, and uterus. It is worth noting that slight structural modifications may also completely alter the exposure and selectivity in the plasma and various tissues (nafoxidine vs. lasofoxifene). Nafoxidine exposure was 2- to 3-fold higher in the plasma and 6- and 8-fold higher in the spleen and fat than lasofoxifene exposure; 4) correlation may exist between drug structure and tissue selectivity, as assessed using principal component analysis and the univariate feature assay. In this experiment, we investigated the STR through seven SERMs and found that even slight structural changes may alter drug selectivity in various tissues.

In summary, we investigated the influence of drug properties such as special formulation, long-lipid modification, and slight structural changes on tissue selectivity. Throughout our research, the importance of tissue exposure or selectivity has been taken into account while selecting drug candidates. To help reduce the current high clinical failure rate during drug development, investigation of drug tissue selectivity in the early stages should be considered.

## **Bibliography**

1. Hinkson, I.V., Madej, B. & Stahlberg, E.A. Accelerating Therapeutics for Opportunities in Medicine: A Paradigm Shift in Drug Discovery. *Frontiers in pharmacology* 11, 770 (2020).
2. Paul, S.M. et al. How to improve R&D productivity: the pharmaceutical industry's grand challenge. *Nature reviews. Drug discovery* 9, 203-214 (2010).
3. Takebe, T., Imai, R. & Ono, S. The Current Status of Drug Discovery and Development as Originated in United States Academia: The Influence of Industrial and Academic Collaboration on Drug Discovery and Development. *Clinical and translational science* 11, 597-606 (2018).
4. Dowden, H. & Munro, J. Trends in clinical success rates and therapeutic focus. *Nature reviews. Drug discovery* 18, 495-496 (2019).
5. Seruga, B., Ocana, A., Amir, E. & Tannock, I.F. Failures in Phase III: Causes and Consequences. *Clinical cancer research : an official journal of the American Association for Cancer Research* 21, 4552-4560 (2015).
6. Di, L., Kerns, E.H. & Carter, G.T. Drug-like property concepts in pharmaceutical design. *Current pharmaceutical design* 15, 2184-2194 (2009).
7. Hughes, J.P., Rees, S., Kalindjian, S.B. & Philpott, K.L. Principles of early drug discovery. *British journal of pharmacology* 162, 1239-1249 (2011).
8. Maia, E.H.B., Assis, L.C., de Oliveira, T.A., da Silva, A.M. & Taranto, A.G. Structure-Based Virtual Screening: From Classical to Artificial Intelligence. *Frontiers in chemistry* 8, 343 (2020).
9. Mak, K.K. & Pichika, M.R. Artificial intelligence in drug development: present status and future prospects. *Drug discovery today* 24, 773-780 (2019).
10. Custer, L.L. & Sweder, K.S. The role of genetic toxicology in drug discovery and optimization. *Current drug metabolism* 9, 978-985 (2008).
11. Davies, M. et al. Improving the Accuracy of Predicted Human Pharmacokinetics: Lessons Learned from the AstraZeneca Drug Pipeline Over Two Decades. *Trends in pharmacological sciences* 41, 390-408 (2020).
12. Yusof, I. & Segall, M.D. Considering the impact drug-like properties have on the chance of success. *Drug discovery today* 18, 659-666 (2013).
13. Bohnert, T. & Gan, L.S. Plasma protein binding: from discovery to development. *Journal of pharmaceutical sciences* 102, 2953-2994 (2013).

14. Zhang, D. et al. Drug Concentration Asymmetry in Tissues and Plasma for Small Molecule-Related Therapeutic Modalities. *Drug metabolism and disposition: the biological fate of chemicals* 47, 1122-1135 (2019).
15. Giacomini, K.M. et al. Membrane transporters in drug development. *Nature reviews. Drug discovery* 9, 215-236 (2010).
16. Abdallah, M. et al. Lymphatic targeting by albumin-hitchhiking: Applications and optimisation. *Journal of controlled release : official journal of the Controlled Release Society* 327, 117-128 (2020).
17. Poulin, P., Burczynski, F.J. & Haddad, S. The Role of Extracellular Binding Proteins in the Cellular Uptake of Drugs: Impact on Quantitative In Vitro-to-In Vivo Extrapolations of Toxicity and Efficacy in Physiologically Based Pharmacokinetic-Pharmacodynamic Research. *Journal of pharmaceutical sciences* 105, 497-508 (2016).
18. Rizk, M.L., Zou, L., Savic, R.M. & Dooley, K.E. Importance of Drug Pharmacokinetics at the Site of Action. *Clinical and translational science* 10, 133-142 (2017).
19. Petiti, J. et al. Bcl-xL represents a therapeutic target in Philadelphia negative myeloproliferative neoplasms. *Journal of cellular and molecular medicine* 24, 10978-10986 (2020).
20. Adams, C.M., Clark-Garvey, S., Porcu, P. & Eischen, C.M. Targeting the Bcl-2 Family in B Cell Lymphoma. *Frontiers in oncology* 8, 636 (2018).
21. Mason, K.D. et al. Programmed anuclear cell death delimits platelet life span. *Cell* 128, 1173-1186 (2007).
22. Schoenwaelder, S.M. et al. Bcl-xL-inhibitory BH3 mimetics can induce a transient thrombocytopenia that undermines the hemostatic function of platelets. *Blood* 118, 1663-1674 (2011).
23. Suvarna, V., Singh, V. & Murahari, M. Current overview on the clinical update of Bcl-2 anti-apoptotic inhibitors for cancer therapy. *European journal of pharmacology* 862, 172655 (2019).
24. Luo, F. et al. Gemcitabine and APG-1252, a novel small molecule inhibitor of BCL-2/BCL-XL, display a synergistic antitumor effect in nasopharyngeal carcinoma through the JAK-2/STAT3/MCL-1 signaling pathway. *Cell death & disease* 12, 772 (2021).
25. Lakhani, N.J. et al. First-in-human study of palcitoclax (APG-1252), a novel dual Bcl-2/Bcl-xL inhibitor, demonstrated advantages in platelet safety while maintaining anticancer effect in U.S. patients with metastatic solid tumors. *Journal of Clinical Oncology* 38, 3509-3509 (2020).
26. Sanders, J.M., Monogue, M.L., Jodlowski, T.Z. & Cutrell, J.B. Pharmacologic Treatments for Coronavirus Disease 2019 (COVID-19): A Review. *JAMA* 323, 1824-1836 (2020).
27. Wang, Y. et al. Remdesivir in adults with severe COVID-19: a randomised, double-blind, placebo-controlled, multicentre trial.
28. Spinner, C.D. et al. Effect of Remdesivir vs Standard Care on Clinical Status at 11 Days in Patients With Moderate COVID-19: A Randomized Clinical Trial.
29. Pan, H. et al. Repurposed Antiviral Drugs for Covid-19 - Interim WHO Solidarity Trial Results.

30. Yan, V.C. & Muller, F.L. Advantages of the Parent Nucleoside GS-441524 over Remdesivir for Covid-19 Treatment.
31. Kokic, G.A.-O. et al. Mechanism of SARS-CoV-2 polymerase stalling by remdesivir.
32. Warren, T.K. et al. Therapeutic efficacy of the small molecule GS-5734 against Ebola virus in rhesus monkeys.
33. Williamson, B.N. et al. Clinical benefit of remdesivir in rhesus macaques infected with SARS-CoV-2.
34. Martinkovich, S., Shah, D., Planey, S.L. & Arnott, J.A. Selective estrogen receptor modulators: tissue specificity and clinical utility. *Clinical interventions in aging* 9, 1437-1452 (2014).
35. Wallace, O.B., Lauwers, K.S., Jones, S.A. & Dodge, J.A. Tetrahydroquinoline-based selective estrogen receptor modulators (SERMs). *Bioorganic & medicinal chemistry letters* 13, 1907-1910 (2003).
36. Renaud, J. et al. Estrogen receptor modulators: identification and structure-activity relationships of potent ERalpha-selective tetrahydroisoquinoline ligands. *Journal of medicinal chemistry* 46, 2945-2957 (2003).
37. Vogel, V.G. et al. Update of the National Surgical Adjuvant Breast and Bowel Project Study of Tamoxifen and Raloxifene (STAR) P-2 Trial: Preventing breast cancer. *Cancer prevention research (Philadelphia, Pa.)* 3, 696-706 (2010).

## **CHAPTER II - Nanomedicine of BCL-2/BCL-X<sub>L</sub> Inhibitors Improve Tissue Targeting, Reduce Platelet Toxicity and Enhance Anticancer Efficacy in Myeloproliferative Neoplasm and Lymphoma**

### **2.1 Abstract**

BCL2 family proteins (BCL-2 and BCL-XL) play important roles in the progression of lymphoma and myeloproliferative neoplasms. However, owing to the critical role of BCL-XL in the survival of platelets, BCL-2/BCL-XL inhibitors are associated with the risk of thrombocytopenia, which limits their clinical potential. APG-1252, as a new generation of BCL-2/BCL-XL inhibitors, is designed to have minimum selectivity to BCL-XL in the circulation system, but its selectivity increases after being metabolized in tissues. Although thrombocytopenia was relieved in clinical trials, APG-1252 still caused a rapid reduction in platelet count at a high dosage (320 mg once per week). Here, we demonstrated that nanomedicine could improve the safety of APG-1252 by preventing its premature metabolism in the blood and inducing fast tissue distribution. In addition, upon changing the formulation to nanomedicine, APG-1252 showed up to 20-fold higher accumulation in target tissues such as the spleen and BM. Confocal images of the spleen showed diffusive distribution of nanomedicine from the marginal zone to the red pulp and mantle cell zone. In mouse models of myeloproliferative neoplasms or mantle cell lymphoma, the nanoformulation of APG-1252 prolonged the survival rate, delayed paralysis occurrence, and reduced tumor infiltration in the spleen and BM compared to the clinical formulation. With the well-established technology (nab®) used in formulation manufacture, nanomedicine of APG-1252 holds promise for use in the future clinical studies.

### **2.2 Introduction**

Myeloproliferative neoplasms (MPNs), as chronic hematological cancers characterized by abnormal growth of blood cells or platelets in bone marrow (BM), are classified into three groups known as polycythemia vera (PV), myelofibrosis (MF) and essential thrombocythemia (ET)<sup>1,2</sup>. JAK2V617 mutation has been considered as one of major drivers in MPNs pathogenesis<sup>3,4</sup>, leading to the approval of JAK2 inhibitors like ruxolitinib as first-line therapy in MF and second-line therapy in PV patients<sup>5</sup>. Besides JAK2 kinases, B-cell lymphoma-2 (BCL2) family proteins have been recently investigated as another potential therapeutic target<sup>6-8</sup>. BCL2 family proteins are normally considered to regulate programmed cell apoptosis through either anti-apoptotic (BCL-2, BCL- XL) or pro-apoptotic (BAX, BAK) members<sup>9</sup>. Recently, the overexpression of BCL2 family proteins especially BCL-XL was found in cells from MPNs patients independent of their JAK2V617F mutation status<sup>6</sup>. Suppression of BCL-2 family proteins by pan-BH3 inhibitor, obatoclax, also showed similar efficacy in reducing the myeloid expansion of MPNs compared to ruxolitinib<sup>7</sup>. Simultaneously targeting JAK2 and BCL-2/BCL-XL was proved to overcome the acquired resistance of MPNs to JAK2 inhibitors, further confirming the therapeutic potential of BCL2 family proteins<sup>10</sup>. Several clinical trials have been undertaken to test the efficacy of single or combinatorial treatments of BCL-2/BCL-XL inhibitors against MPNs<sup>11-13</sup>.

However, BCL- XL pathway is not only important to the tumor cell proliferation in MPNs, but also critical to the survival of platelets in blood<sup>14,15</sup>. Clinical trials with dual BCL-2/BCL-XL inhibitors were usually terminated in early stage because of rapid thrombocytopenia (platelet toxicity) in recruited patients<sup>16-18</sup>. To overcome the dilemma existed for BCL-2/BCL-XL inhibitors between achieving high efficacy and meanwhile maintaining low platelet toxicity, prodrug strategy was utilized and APG-1252 was developed as one of the representatives<sup>19,20</sup>. APG-1252 was designed as a prodrug which showed higher selectivity to BCL-2 and low platelet toxicity after administration. Once APG-1252 was distributed into target tissues it would be metabolized to more active compound, APG-1244, which increased selectivity to BCL- XL and demonstrated higher anti-tumor efficacy<sup>21</sup>. To be noted, prodrug strategy used to reduce BCL- XL selectivity in circulation system needs to be designed finely to prevent pre-mature metabolism of APG-1252 to APG-1244. Recent clinical results demonstrated that APG-1252 did reduce

the thrombocytopenia at some extent but its most common adverse effect was still decreased platelet count (14.3%), and any dosages over 300 mg QD could result in rapid platelet drop<sup>22</sup>.

Nanoparticles as a special formulation is well known to effectively protect the degradation of its encapsulated cargos like mRNA<sup>23, 24</sup>. We hypothesized that by making nano-formulation of APG-1252, the generation of APG-1244 in blood could be minimized together with improved platelet toxicity. In this study, we successfully prepared nanocomplexes of APG-1252 (nano-1252) and confirmed its high physicochemical stability in vitro and in vivo. Short-term platelet toxicity was largely improved for nano-1252 due to its reduced pre-mature metabolism of APG-1252 and fast tissue distribution. Interestingly, nano-1252 showed more accumulation of both APG-1252 and APG-1244 in tissues like spleen and BM. Patients with MPNs are known to develop symptoms like bone/joint pain and splenomegaly due to extramedullary hematopoiesis (EMH)<sup>25, 26</sup>. Higher accumulation of nano-1252 in target tissues like BM and spleen contributed to its better anti-tumor efficacy in MPNs mice model. The effectiveness of nano-1252 was further confirmed in lymphoma model which was also sensitive to BCL-2/BCL-XL inhibitors and progressed with tumor infiltration in bone marrow and spleen. In summary, compared to clinical formulation (clinical-1252), nano-1252 reduced platelet toxicity and meanwhile improved target tissues accumulation, resulting in enhanced anticancer efficacy in MPNs and lymphoma.

### 2.3 Results and Discussion

**Marketable manufacture of nano-1252 with high physicochemical stabilities.** Serum albumin was used to form nanocomplexes with APG-1252 because of its high drug loading efficiency for hydrophobic molecules and mature manufacture pipeline from Abraxane® (nab-paclitaxel)<sup>27, 28</sup>. Similar preparation procedure with nab® technology<sup>29</sup> used in Abraxane® was adopted for the manufacture of nano-1252 (Figure 2.S1a). With the manufacture process going and stronger physical force acting on the system, the formulation became more translucent with its particle size reduced from 10-20 um to 50-100 nm (Figure 2.S1b, Figure 2.1a). The whole manufacture process for nano-1252 was proved to be robust to different homogenizer pressure/cycles and freeze-drying



temperatures (Figure 2.S1c-e). With homogenizer pressure as low as 5000 psi and single process cycle, APG-1252 and albumin could also form nanoparticles with size around 150 nm (Figure 2.S1d). Besides, different primary drying temperature (from -10 °C to 10 °C) during lyophilization would not influence the cake shape of freeze-dried powder and their size distribution (Figure 2.S1e). The resuspension performance of nano-1252 was also better with its resuspended concentration could be as high as 40 mg/ml compared to 10 mg/ml of clinical-1252 (Figure 2.S1f). The composition of nano-1252 was similar with Abraxane®, having more than 80% free or simple albumin complexes in the system while more than 80% APG-1252 was encapsulated into nanoparticles (Figure 2.S1g and h).

The easy and robust manufacture of nano-1252 was possibly attributed to the strong binding affinity between APG-1252 and albumin. Compared to paclitaxel, the molecular interaction between APG-1252 and albumin was much stronger with their docking simulation value as 7.09 vs 13.47 (Figure 2.1b and Figure 2.S2a). Their strong interaction also explained the smaller particle size (about 70 nm vs. 130 nm) and higher formulation stability of nano-1252 than Abraxane®. After dilution with saline from 5-fold (1 mg/ml) to 50000-fold (100 ng/ml), the particle size of nano-1252 was still maintained below 100 nm with PDI around 0.2 (Figure 2.1c). However, Abraxane® will dissociate quickly even with 500-fold dilution (10 ug/ml) and new intensity peak could be observed around 10 nm (Figure 2.S2b). By capturing the movement of particles, nanoparticle tracking analysis (NTA) also showed that only several dim particles remained for Abraxane® after 500-fold dilution (Figure 2.1d, Figure 2.S2c). In contrast, bright particles could be observed for nano-1252 even after 5000-fold dilution. To test the stability of nano-1252 after administration, the formulation was incubated with plasma under 37 °C with volume ratio as 1:5000 (Figure 2.1e). Mode size of formulation detected by NTA was still among 100-150 nm 4 h or 24 h later. The higher particle size than previous DLS result (about 70 nm) could be caused by viscous plasma (abundant of albumin) which decreased the mobility rate of nano-1252 and hence caused larger detected size. Long time incubation did show some influence on the breakup or aggregation of nano-1252 with larger particle concentration and separation of two particle peaks observed at 24 h from Figure 2.1e. To test the storage stability of nano-

1252, freeze-dried powder was stored at different temperature (-20 °C, 4 °C and 25 °C) for up to 13 months. Nano-1252 maintained high formulation stability with size fluctuating within 70-76 nm, and PDI within 0.13-0.16 (Figure 2.1f). Besides there was no apparent degradation of APG-1252 to APG-1244 observed at -20 °C and 4 °C (Figure 2.1g). Only around 3% of APG-1244 was tested in 13th month when stored at 25 °C. If 1% 1244 is taken as the limit, the shelf life of nano-1252 at 4 °C could be about 3 years (34.5 months) according to zero-order metabolism simulation (Figure 2.S2e and f). To be noted, no other metabolites (impurities) were observed for nano-1252 during the storage conditions, while apparent impurities appeared in clinical-1252 when stored at room temperature (Figure 2.S2h).

**Nano-1252 decreased platelet toxicity due to its fast tissue distribution and reduced pre-mature metabolism of APG-1252.** Platelet toxicity under different doses was compared between nano-1252 and clinical-1252. As shown in Figure 2.2a, no apparent decrease of platelet counts (PLT) was observed for both formulations at 10 mg/kg. However, when dosage was increased to 50 mg/kg, clinical-1252 reduced platelet counts significantly at 4 h after administration. Such decrease lasted at least 24 h and returned to normal level after one week. However, only minor influence on platelet counts was observed for nano-1252 around 24 h. The reduced platelet toxicity was further confirmed from microscope images (Figure 2.S3a and b). To be noted, the protection of platelets from nano-1252 also worked when dosage was increased to as high as 100 mg/kg. There were studies showed that young platelets which had larger size were more resistant to BCL-XL inhibitor<sup>14, 30</sup>. Toxicity of clinical-1252 to aged platelets resulted in elevated mean platelet volume (MPV) accordingly. We also analyzed their influence on other blood parameters related to leukocytes and erythrocytes, and found that nano-1252 show no significant difference with clinical-1252 and both formulations kept these parameters within normal range (Figure 2.S4a-c).

Since the metabolite APG-1244 was the major reason to cause platelet toxicity, its concentration in blood and plasma was analyzed and compared between two formulations (Figure 2.2b). Interestingly, 2 to 4-fold lower concentration of APG-1244 was observed in nano-1252 from both blood and plasma samples. The low exposure of APG-1244 in

nano-1252 explained well its better platelet protection activity and could be attributed to at least two factors: 1) fast distribution of nano-formulation and 2) reduced metabolism of APG-1252. As shown in Figure 2.2b, concentration of APG-1252 in nano group also exhibited lower level than clinical-1252, which represented the faster distribution of nano-1252 in vivo. The protection of APG-1252 to APG-1244 was also confirmed in nano-formulation from both in-vitro and in-vivo environments. As shown in Figure 2.2c, solution of two formulations was stored at 4 °C and nano-1252 significantly decreased the metabolism of APG-1252 to APG-1244. Even in blood and plasma samples, the ratio of APG-1244 to APG-1252 in nano-1252 was around half of that in clinical-1252 (Figure 2.2d). Similar phenomenon was observed in other tissues, where nano-1252 generated less percentage of APG-1244 compared to clinical-1252 (Figure 2.2e).

**Nano-1252 improved distribution in target tissues including BM and spleen.** To understand whether change of formulation could have influence on other tissues distribution, concentration-time profile in different tissues was analyzed in detail between nano-1252 and clinical-1252 (Figure 2.S5a-d, Figure 2.3a and b). Nano-1252 showed 2 to 8-fold higher accumulation of APG-1252 in tissues like spleen, bone, fat pad and liver, while in tissues like uterus, skin, intestine, colon, heart and fat, clinical-1252 showed higher exposure of APG-1252 (Figure 2.3a). Due to the decreased metabolism in nano-formulation, most tissues from clinical-1252 administration group showed higher exposure of APG-1244. However, nano-1252 still maintained 2 to 4-fold of APG-1244 in spleen and bone (Figure 2.3a and b). By changing the clinical formulation to nano-formulation, the tissue distribution of compound was significantly altered and demonstrated higher selectivity to spleen and bone (majorly BM). To further confirm this tissue preference caused by nano-formulation, other mice species were also tested. In BALB/c mice, nano-1252 showed 2 to 20-fold higher concentration of both compounds in spleen and BM (Figure 2.3c). Mononuclear phagocyte system (MPS) was normally considered to play an important role in the accumulation of external nanoparticle in tissues like spleen<sup>31</sup>. Here, we depleted the macrophages in BALB/c mice and did find about 80% decrease of both compounds in nano-1252 (Figure 2.3d). However, MPS seemed to also affect the accumulation of clinical-1252 in a similar way and relative

higher concentration of compounds was still observed in nano-1252. In immune deficient mice, nano-1252 and clinical-1252 kept the similar trend as in normal CD-1 or BALB/c mice. Nano-1252 showed higher concentration of compounds while the value in spleen decreased rapidly at 24 h, hinting the potential role of B/T cells in the long-term retention of nano-formulation (Figure 2.3e). Besides spleen and BM, nano-1252 appeared to have more accumulation in lymph nodes in long term (Figure 2.S5a-b, S6). APG-1252 and APG-1244 in nano-1252 showed lower concentration level at 4 h while this trend was reversed at 24 h in mice with or without macrophages depletion (Figure 2.S6a and b).

Fluorescent nano-1252 was prepared to further detect its distribution in subareas of spleen. As shown in Figure 2.3f, nano-1252 was widely dispersed in the marginal zone which stays at the interface between white pulp and red pulp. Due to the biological function of CD169+ macrophages to engulf external particles, high fraction of this type of cells was co-localized with nano-1252 (0.8-0.9). Along with the time, nano-formulation also diffused slowly from marginal zone to red pulp or mantle zone. By calculating the co-localization coefficient of nano-1252 and B-cell, higher value was observed at 24 h compared to 4 h (Figure 2.3g). Distribution of nano-formulation in spleens from mice with macrophages depleted or deficient of lymphocytes was also compared and shown in Figure 2.S7. After depletion of macrophages, lower fluorescence signal was observed in nano-1252 and its distribution was majorly focused on the red pulp area and outer space of white pulp. In NOD SCID mice, diffusive distribution of nano-1252 was more obvious likely attributed to its less organized structure of spleen. Significant lower signal of nano-1252 at 24 h was also observed in the immune deficient mice, which further confirmed the role of immune cells in long-term retention of nanoparticles.

**Established tumor model of MPN and mantle cell lymphoma.** Diseases like leukemia, lymphoma, lung cancer and MPNs could be beneficial from the treatment of BCL-2/BCL-XL inhibitors<sup>32</sup>. Based on the findings that high accumulation of nano-1252 was observed in BM and spleen, MPNs and mantle cell lymphoma were selected for further efficacy test due to their disease progression in these target tissues. We firstly tested the sensitivity of selected cells to APG-1252 and found high cytotoxicity in Mino (mantle

cell lymphoma) and SET-2 cells (essential thrombocythemia) with IC50 around 0.5  $\mu$ M (Figure 2.4a). Nano-1252 showed slight decrease of in-vitro efficacy which was possibly due to its encapsulation of APG-1252 inside particles and hence delay of its cellular uptake. Mino and SET-2 cells were selected to establish the related tumor models by injecting the immune deficient mice intravenously. As shown in Figure 2.4b, at around day 45, enlarged spleen could be observed from both tumor models. Splenomegaly was more obvious in mino cell model with mean spleen weight increased from 0.02 g to 0.1 g (Figure 2.S8a). Bone disease was also established in two models with paralysis appeared in SET-2 model and whiten bone found in mino model (Figure 2.4b). The disease progress in SET-2 model was more aggressive with obvious decrease of weight at around day 40 and death occurred within one to two weeks (Figure 2.S8b and c). Spleens and BM from two established models were further processed through flow cytometry to detect the tumor infiltration. Significant increase of infiltrated tumor cells was found in both models (Figure 2.S8d and e) and representative figures were shown in Figure 2.4c. H&E staining of spleens and BM from tumor models were also compared with control (Figure 2.4d), the structure of spleen and BM exhibited in control mice disappeared in tissues from both disease models. Spleen from mice established with two mino cells was also tested for the distribution of nano-1252. As shown in Figure 2.4e, both tumor cells and nano-1252 spread widely throughout the spleen tissue, and due to this, partial co-localization between formulation and mino cells could be observed with the coefficient around 0.3-0.4.

**Enhanced anti-tumor efficacy of nano-1252.** After confirming the establishment of the tumor models with spleen and BM disease, nano-1252 was tested for its efficacy compared to clinical formulation. As shown in Figure 2.5a-d, clinical-1252 showed no benefits in aggressive SET-2 model with the survival or non-paralysis rate from treatment was not improved. However, better survival was observed in nano-1252 with 3 days elongated in median survival when compared to clinical-1252 or control group (52 day vs 49 day, Figure 2.5b). Similar result was also observed in the improved paralysis occurrence from nano-1252 (Figure 2.5c). Weight change was another parameter to reflect the health status of mice. Nano-1252 delayed the weight decrease effectively when

compared to clinical-1252. In another tumor model established with mino cells, better survival performance was also observed in nano-1252 (Figure 2.5e-g). 3 days or 10 days improved in median survival was also found in nano-1252 when compared to clinical 1252 (72 day vs 69 day) or control group (72 day vs 61.5 day). Weight change showed the similar pattern that control group had the fastest weight loss while nano-1252 behaved the best (Figure 2.5g). In another group of mino model, mice with different treatment groups were sacrificed at Day 49 and tested spleen weight change and tumor infiltration in target tissues (Figure 2.5h). As shown in Figure 2.5i, j and l, both treatment groups decreased infiltration significantly in BM (median value from 49.81% to 18.73% in clinical-1252 and 4.32% in nano-1252) and spleen (median value from 16.65% to 5.92% in clinical-1252 and 1.18% in nano-1252). Due to the large variance existed in treatment groups, the better efficacy in nano-1252 than clinical-1252 could only be concluded from their median value difference. Similar result was found in the spleen weight change (Figure 2.5k and Figure 2.S8f), where nano-1252 showed median weight about 0.05 g compared to 0.076 g in clinical-1252 and 0.21 g in control group.

## 2.4 Conclusion

Albumin-based nano-formulation of APG-1252 was successfully prepared in this study with nab® technology. Nano-1252 showed encouraging results in both decreased thrombocytopenia and enhanced accumulation in target tissues like spleen and BM. Such in-vivo performance of nano-1252 was majorly contributed by its high formulation stability. Because of this, nano-1252 maintained the forms of nanoparticles after administration, functioning to protect its fast metabolism to APG-1244 in blood. In the other side, nano-1252 also had its biodistribution of APG-1252 largely altered. Because of the biological function of MPS in engulfing external particles<sup>33, 34</sup>, large amount of nano-1252 was trapped in spleen and BM, resulting in high accumulation in these tissues and low concentration in circulation system. Low blood exposure of nano-1252, together with its protection of APG-1252 to APG-1244, explained why nano-1252 could decrease the platelet toxicity with maximum tolerated dose (MTD) increased at least 2 folds.

The high accumulation of nano-1252 in tissues like spleen and BM, especially its diffusive distribution in red pulp area and mantle cell zone of spleen, could benefit more

disease like MPNs and mantle cell lymphoma. Due to dysregulated BM microenvironment in MPNs, hematopoietic cells will migrate to organs outside of the BM (like spleen) for the continuous production of blood cells, leading to progressive spleen enlargement<sup>25, 35</sup>. Similar splenomegaly can be also observed in mantle cell lymphoma<sup>36, 37</sup>, but differently the enlarged spleen is caused by tumor infiltration. Therefore, nano-1252 could increase the potential of APG-1252 in treating MPNs and mantle cell lymphoma by increasing accumulation in spleen and BM. In our tumor mice models, nano-1252 prolonged the survival rate, delayed paralysis occurrence and reduced tumor infiltration in spleen and BM when compared to clinical-1252. To be noted, as the first- or second-line treatment of mantle cell lymphoma or MPNs, BTK inhibitor, ibrutinib<sup>38</sup>, or JAK2 inhibitor, ruxolitinib<sup>5</sup>, also showed additive or synergistic cytotoxicity with nano-1252 in SET-2 or Mino cells (Figure 2.S9). Even in the SET-2 cells resistant to ruxolitinib (SET-2/re), nano-1252 was also proved to be effective (Figure 2.S9).

## 2.5 Experimental Section

**Cells and animals.** Mino (CRL-3000), REC-1 (CRL-3004), Z-138 (CRL-3001), HEL 92.1.7 (TIB-180) were purchased from ATCC (American Type Culture Collection USA); SET-2 was from DSMZ (Germany). Rec-1 and HEL 92.1.7 cells were cultured in RPMI 1640 (ATCC) with 10% h.i. FBS; Mino and SET-2 cells were cultured in RPMI 1640 with 20% h.i. FBS; Z-138 cells were cultured in Iscove's Modified Dulbecco's Medium (ATCC) with 10% horse serum. CD-1 ISG, BALB/c, NOD SCID mice were purchased from Charles River and used for platelet toxicity, PK and biodistribution study. NOD.Cg-Prkdcscid IL2rgtm1Wjl/SzJ mice were ordered from the Jackson Laboratory and used for efficacy study. All animal procedures used in this study were approved by the University Committee on Use and Care Animals at the University of Michigan.

**Preparation of nano-1252.** Crude emulsion was prepared by simply mixing organic solution (100 mg/ml APG-1252 in chloroform, 3 ml in total) with 20 ml of 5% HSA solution (Albutein®, Grifols Biologicals Inc. USA). The mixture was dispersed under high shear force with speed set around 8-12K rpm and time around 4-5 mins (t-25 Ultra-

turrax, IKA, USA). Formed milk-like emulsion was further processed to nano-emulsion through high-pressure homogenizer with pressure set around 15K psi, processing cycles about 5 and cooling temperature under 4 °C (Nano DeBEE, BEE international, USA). To remove the organic residue, rotary evaporation of formulation was carried out with vacuum procedurally adjusted and water bath temperature about 20 °C (Vacuum pump v-100, Buchi, Switzerland). The solution was then filtrated through 0.22 µm sterile syringe filter (Fisher Scientific, Ireland) before freeze drying. The lyophilization procedure was set with primary drying step holding at 0°C for 7 h under 150 mTorr and secondary drying step holding at 30 °C for 5 h under 150 mTorr (VirTis advantage pro freeze dryer, SP scientific, USA). 10 ml Serum vials (Thomas Scientific, USA) with freeze dried formulation powder were finally sealed with N<sub>2</sub> and stored at -20°C for future use. Fluorescent formulation (nano-1252/DiD) was prepared by mixing DiD dye (Fisher Scientific, USA) with APG-1252 in organic solution and the following processes remained the same. Mouse albumin (Molecular Innovations, USA) was used to replace HSA when preparing formulations used for animal experiments like PK study and in-vivo anti-tumor efficacy study.

**Characterization of nano-1252.** TEM images of nano-1252 were captured by transmission electron microscope (JEOL JEM-1400 Plus LaB6 TEM, USA). Briefly samples from different preparation steps were evaporated to remove chloroform and centrifugated to reduce amount of free albumin in the system. Precipitates were resuspended with pure water and dipped on carbon support film square grid (400 mesh, 3-4 nm, copper, Electron Microscopy Sciences, USA) to prepare TEM samples. The influence of different processing pressure and cycles in homogenizer on the formulation size distribution was characterized. Briefly, during the preparation process, formulation solution eluted from homogenizer after each cycle (from 1-5 cycles) was collected for image capture and size analysis (Zetasizer, Malvern panalytical, USA). Resuspension ability after freeze drying was also compared between nano-1252 and clinical formulation. Both formulations were resuspended in 24-well plate by PBS, saline or water to achieve the final concentration from 5 mg/ml to 40 mg/ml. Black line marked on the back side was used to observe the transparency of formulations. NativePAGE Bis-



Tris gel (Invitrogen, USA) was used to analyze the native proteins and protein complexes from our nano formulation. Coomassie G-250 binds to proteins and confers a net negative charge without denaturing the proteins. 10 µl samples from pure albumin solution, nano-1252 and abraxane were loaded with the protein concentration fixed as 1 mg/ml through BCA protein assay (Thermo Scientific, USA). The detailed composition of nano-1252 was tested through separating nanoparticles with free albumin or simple protein-compound complexes by centrifugation. Briefly, 200 µl of nano-1252 resuspension (10 mg/ml) was centrifugated for 1.5 h with force set as 20,000 g and temperature under 4 degree. Concentration of albumin and drug in supernatant or pellets resuspension were analyzed through BCA protein assay kit and HPLC.

**Chemical and physical stability of nano-1252.** Sealed vials with powder of nano-1252 and clinical-1252 were stored at -20 °C, 4 °C and 25 °C with light protection. At schedule time points (0 month, 1 month, 3 month, 6 month and 13 month), three vials of nano-1252 and clinical-1252 were collected and resuspended using water to make formulation with concentration around 10 mg/ml. For the analysis of chemical stability, free compound was recovered by adding 20 µl formulation into 180 µl acetonitrile and sonicating the mixture at room temperature for 5 min. Precipitates were removed by centrifugation (10,000 g, 10 min, 4 °C) and supernatant was analyzed by HPLC (Shimadzu, Japan). C18 column (150 mm x 4.6 mm, 3.5 µm, Waters, USA) was used for the analysis with flow speed as 0.8 ml/min, detecting wavelength as 254 nm, solvent phase A as triethylamine phosphate buffer (pH around 3.5) and solvent phase B as acetonitrile. Retention time of APG-1252 and APG-1244 was confirmed by the standard compounds. Peaks areas were analyzed and summed up to calculate the percentages of APG-1252, APG-1244 and other impurities (peak area ratio > 0.1%). For the analysis of physical stability during storage, nano-1252 samples at different time points were diluted and tested the size distribution using DLS method. To simulate the formulation status of nano-1252 after iv administration, resuspended solution was diluted by saline with final concentration ranging from 1 mg/ml to 100 ng/ml, and each dilution was analyzed its size distribution by DLS. Besides, nano-1252 was also incubated with mouse plasma (volume ratio, 1:500) at 37 °C to test the influence of in-vivo environment on the formulation

stability. At scheduled time points (2 h, 4 h and 24 h), samples were collected, and their particles' concentration and mode size were analyzed by Nanosight (NS300, Malvern, UK).

**Platelet toxicity.** Three dosages of nano-1252 and clinical-1252 (10 mg/kg, 50 mg/kg and 100 mg/kg) were administered to CD-1 mice (female, 6-8 weeks, n=10 per group). At each time point (0 h, 4 h, 24 h and 7 day), retro-orbital blood was collected by EDTA rinsed micropipets (Drummond Scientific, USA) and stored in microvette with EDTA preparation (Sarstedt, USA). Platelets' number and volume together with other blood cells were recorded through complete blood count (Heska HT5 Element, USA). Blood samples under 50 mg/kg dosage were prepared as smear slides and the images were captured under microscope.

**PK study of nano-1252 and clinical-1252.** Two formulations were intravenously administered to CD-1 mice (female, 6-8 weeks, n=5 per time point) with dosage as 50 mg/kg (10 mg/ml). At scheduled time point (0.5 h, 2 h, 4 h, 8 h, 24 h and 48 h), mice from each group were anesthetized by isoflurane and retro-orbital blood was collected. Immediate centrifugation of blood was processed to remove cell clumps and prepare plasma. Mice were finally sacrificed and different tissues including skin, fat pad, heart, lung, pancreas, spleen, liver, kidney, stomach, intestine, colon, fat, uterus, muscle, bone and brain were collected for drug concentration analysis. Confirmation of tissue distribution of two formulations was tested in BALB/c mice, BALB/c mice depleted of microphages and NOD SCID mice. All mice were aged among 6-8 weeks and had sex of female. Depletion of microphages in BALB/c mice was processed by injecting 200 µl liposomal clodrosome (Encapsula NanoSciences, USA) intravenously with the concentration as 5 mg/ml 2 days before dosing 1252 formulations. At 4 h or 24 h after formulation injection (50 mg/kg), tissues like pat pad, fat pad without lymph nodes, lymph nodes, spleen, BM and lung was collected. Before LC-MS/MS analyzing, tissue suspensions were prepared by adding 5-fold weight of 20% acetonitrile into tissues and homogenizing the mixture through Precellys Lysing Kit (7700 rpm, 20 s x 4 per cycle, 3 cycles in total, 4 °C). 30 µl tissue suspensions were further diluted into 170 µl acetonitrile

with CE302 as the internal standard. After being shaken under 840 rpm for 10 min, the suspensions were centrifuged and the supernatant was collected for concentration test. LC-MS/MS analysis of APG-1252 and its metabolite APG-1244 were performed using LC 20AD UFLC (Shimadzu, Japan) coupled with an API 5500 (AB Sciex, USA). 50 x 2.1 mm C18 column (3.5  $\mu$ m, Agilent, USA) was used for the separation and the mobile phases were consisted of water (0.1% formic acid, phase A) and acetonitrile (0.1% formic acid, phase B). Multi-stage linear gradient was initiated with 5% phase B for 1 min, increased to 95% phase B in 2 min and maintained for 4 min at a flow rate of 0.4 ml/min.

**Confocal study.** For analysis of formulation distribution in normal mice, BALB/c mice (female, 6-8 weeks) were injected with nano-1252/DiD (about 10  $\mu$ g DiD dye per mouse, n=3). At scheduled time points (4 h and 24 h), mice were sacrificed, and spleens were collected and fixed by immersing into 1% paraformaldehyde PBS solution for 1-2 hours at room temperature. Tissues were then washed with PBS 3 times and embedded into OCT compound and stored at -80 °C. Confocal slides were then prepared by cutting 10-15  $\mu$ m thick sections from embedded tissues with cryostat (). Prepared slides were blocked for 30 min with 1% FBS and 5% rabbit serum before staining. Primary antibodies including Pacific Blue anti-mouse IgD antibody (BioLegend, USA), FITC anti-mouse IgM antibody (BioLegend, USA) and Alexa Fluor 594 anti-mouse CD169 (Siglec-1) antibody (Biolegend) were diluted 100 times with blocking solution and immerse the tissue area on the slides at 4 °C overnight. The staining solution was washed thoroughly to remove unbound primary antibody and slides were finally mounted in DAPI Fluoromount G (SouthernBiotech, USA) for confocal imaging (Nikon A1si confocal, Japan). Confocal analysis was also used to confirm the microphage depletion in the spleen from normal mice. 200  $\mu$ l of Clodrosome solution (5 mg/ml, Encapsula NanoSciences) was intravenously injected into BALB/c mice and 2 days later, spleens were collected and stained with anti-IgD, anti-IgM and anti-CD169 through the similar procedure. For analysis of formulation distribution in mice established with disease model, NOD.Cg-Prkdcscid IL2rgtm1Wjl/SzJ mice were iv injected with 5\*10<sup>6</sup> Mino cells and nano-1252/DiD was administered 40 days later when the enlarged spleen was observed. 4 h after the administration, spleens were collected for the preparation of

frozen slides and stained with Pacific Blue anti-mouse IgD, FITC anti-human CD20 and Alexa Fluor 594 anti-mouse CD169 antibodies according to the previous similar procedure.

**Cytotoxicity.** Breast cell lines (MCF-7, BT474, ZR7530, HCC1954, MDA453, SKBR3, HCC1937, MDA468, MDA231, SUM149 and SUM159), lymphoma cell lines (Mino, Z138 and REC) and MPN (myeloproliferative neoplasm) cell lines (SET-2 and HEL) were tested for the in-vitro efficacy of nano-1252 and clinical-1252. Briefly, 5000-10,000 cells per well were cultured in 96-well plate overnight, and then incubated with series of concentration of compound for 72 h (breast cell lines) or 48 h (lymphoma and MPN cell lines). Cell viability was tested by MTS assay (Cell Proliferation Assay Kit, Promega, USA) according to its protocol.

**Establishment of tumor model.** NOD.Cg-Prkdcscid IL2rgtm1Wjl/SzJ mice were injected with  $5 \times 10^6$  Mino cells or  $5 \times 10^6$  SET-2 cells through tail vein. 45 days after administration, mice were sacrificed and spleens and bones were collected for cytometry and H&E staining analysis. For cytometry purpose, bone marrow (BM) was prepared from bone through centrifugation method. The BM pellets were resuspended with 1640 medium and filtered through 40  $\mu$ m sterile cell strainer (Fisher Scientific, USA) twice. After being washed by 1640, BM was resuspended with staining buffer (ice cold PBS, 10% FBS, 0.1% sodium azide) to the final concentration around  $1 \times 10^7$  cells/ml per tube (100  $\mu$ l in total, BD Falcon tube). Spleen suspension was prepared by grinding the spleen with sterile syringe interior rubber and filtering through 75  $\mu$ m strainer and 40  $\mu$ m strainer. After being washed by 1640, splenocytes were resuspended with staining buffer to the final concentration around  $1 \times 10^7$  cells/ml per tube (100  $\mu$ l in total). 5  $\mu$ l each primary antibody (APC anti-human CD19 and FITC anti-human CD20 for Mino cell staining, APC anti-human CD13 and FITC anti-human CD33 for SET-2 cell staining) was added and incubated for 30 min at 4 °C preventing from light. After immunostaining, primary antibodies were removed by washing the samples three times with staining buffer and resuspended in 500  $\mu$ l staining buffer. 5  $\mu$ l of 7-AAD viability staining solution (BioLegend) was added into each tube before flow testing (CytoFLEX, Beckman

Coulter, USA). For H&E staining analysis, spleens and bones were collected and immersed in fixative (4% paraformaldehyde) immediately for 24 h at 20:1 volume:tissue ratio. After fixation, tissues were embedded in OCT compound and slides with thickness around 10  $\mu$ m were prepared by cryostat (Leica CM1950, German). H&E staining in frozen slides was prepared according to standard protocol and the images were digitalized for further analysis.

**Animal efficacy.** NOD.Cg-Prkdcscid IL2rgtm1Wjl/SzJ mice were iv injected with  $5 \times 10^6$  Mino cells or  $5 \times 10^6$  SET-2 cells to establish tumor models. One week later, 40 mg/kg of nano-1252 or clinical-1252 was iv administered to mice once per week for 4 weeks in total. In survival rate comparison experiment, mice weight (N=10 per group) was monitored till day 49 for SET-2 model and day 65 for Mino model. Survival and paralysis status of experimental mice were recorded every day for both tumor models. To observe the tumor infiltration difference in spleen and BM, Mino tumor models (N=8 per group) were established and treated with clinical-1252 or nano-1252 as previously described. At day 49, mice were sacrificed and both spleens and BM were collected for flow cytometry.

## **2.6 Figures and Tables**

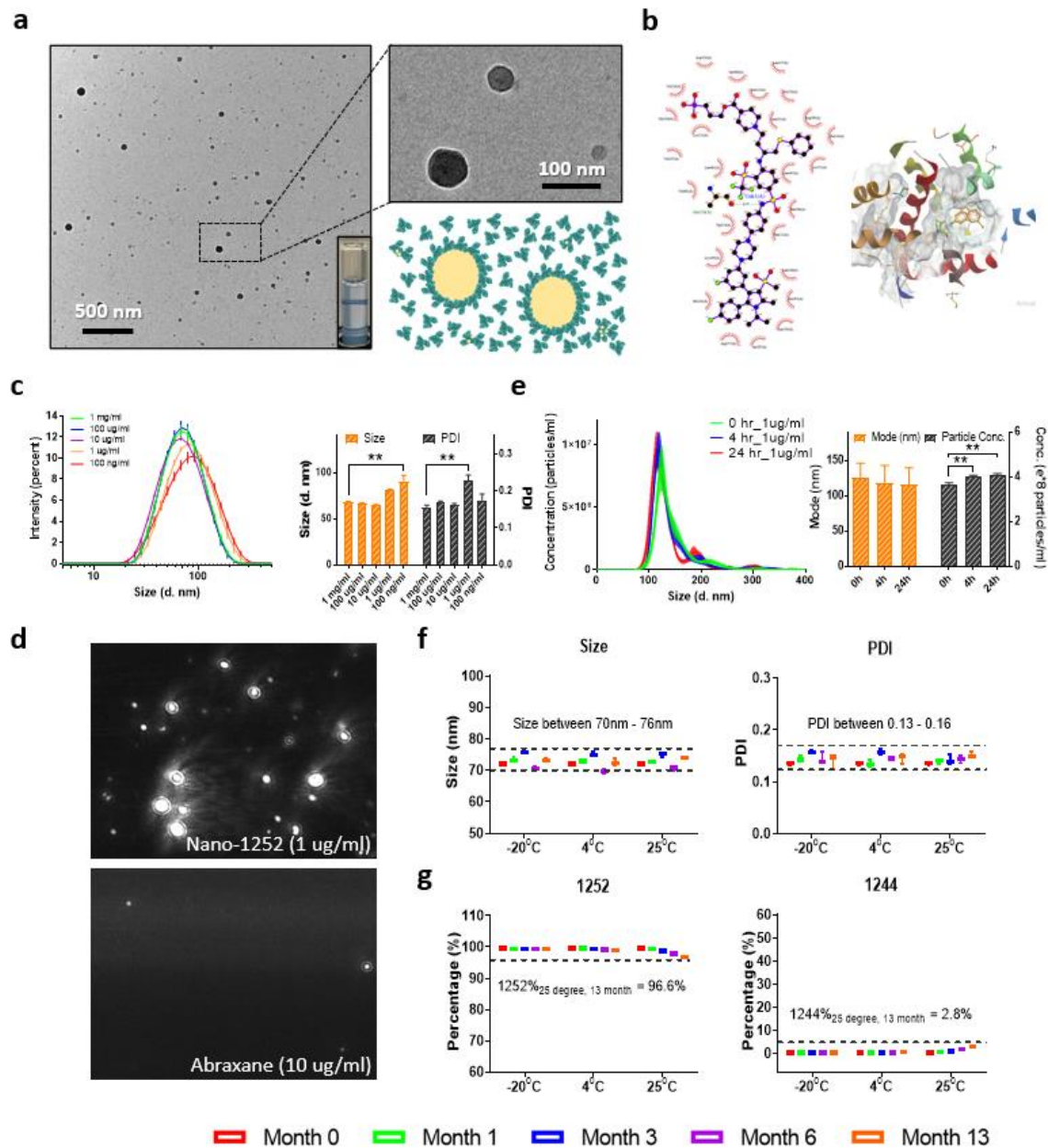


Figure 2.1. High physicochemical stability of nano-1252. a TEM image of nano-1252 and the appearance and schematic representation of the nano-formulation. b Docking simulation between APG-1252 and albumin protein (2BXK). c Dilution stability of nano-1252 by Dynamic Light Scattering (DLS). Nano-1252 was diluted from 5 mg/ml with saline. N=3 for each condition with values represented as mean  $\pm$  SEM (one-way ANOVA test with multiple comparisons against 1 mg/ml. P value is adjusted). d Microscope images of the movement of nano-1252 (1 ug/ml) and Abraxane® (10 ug/ml) by Nanoparticle Tracking Analysis (NTA). Formulations were diluted from 5 mg/ml with saline. e Particle concentration and mode size change for nano-1252 when incubated with plasma at 1 ug/ml for different time points. NTA was used for the analysis. N=5 for each condition with data represented as mean  $\pm$  SEM (one-way ANOVA test with multiple comparisons against 0 h. P value is adjusted). f Size and PDI change during the storage of nano-1252 under different temperature. N=3 for each condition with values represented in boxplot (min to max). Asterisks indicate the following p-value: \* < 0.05, \*\* < 0.01.

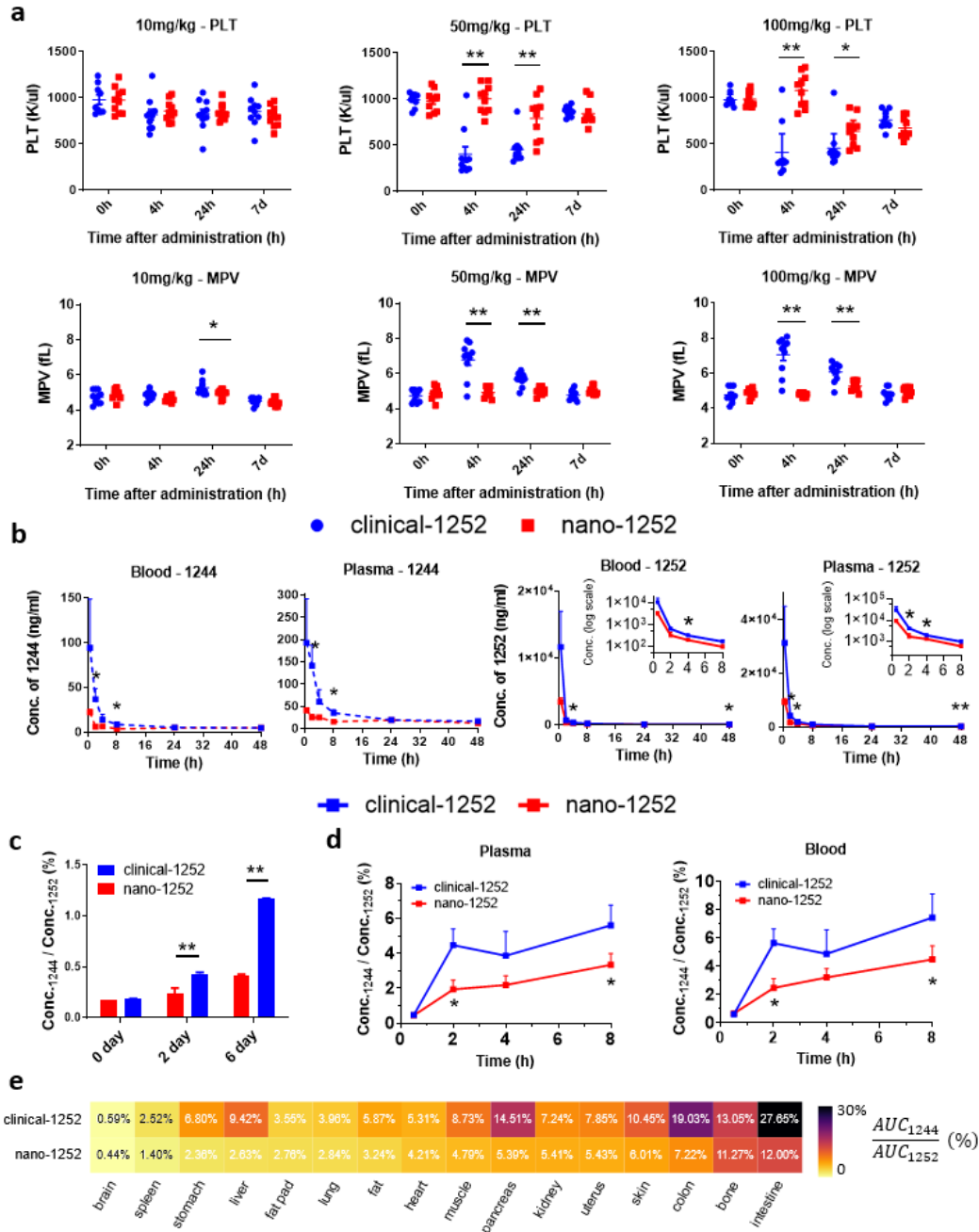


Figure 2.2. Nano-1252 decreased platelet toxicity due to fast distribution of formulation and limited generation of APG-1244 in circulation system. a Platelet count and volume comparison between nano-1252 and clinical-1252 under different dosage administration. N=10 CD-1 mice for each administration group with values represented as mean  $\pm$  SEM (two-tailed t-test). b Concentration-time profile of APG-1244 and APG-1252 in blood and plasma samples from treatment groups. Two formulations were intravenously administered to CD-1 mice (n=5 per time point) with dosage as 50 mg/kg (10 mg/ml). Values are represented as mean  $\pm$  SEM (two-tailed t-test in each time point). Inserted graphs are replotted using the same data but with concentration in log scale. c Percentage of APG-1244 generated during storage of resuspended formulations under 4 °C. N=3 for each condition with values represented as mean  $\pm$  SEM (two-tailed t-test). d Percentage of APG-1244 generated in circulation system after administration of two formulations. Data from b are used for the calculation. Values are represented as mean  $\pm$  SEM (two-tailed t-test in each time point). e AUC percentage of APG-1244 generated in different tissues after administration of nano-1252 and clinical-1252. AUC was calculated using non-compartment model with average concentration data from 0 to 48 h (Supplementary Fig. 5). Asterisks indicate the following p-value: \* < 0.05, \*\* < 0.01.

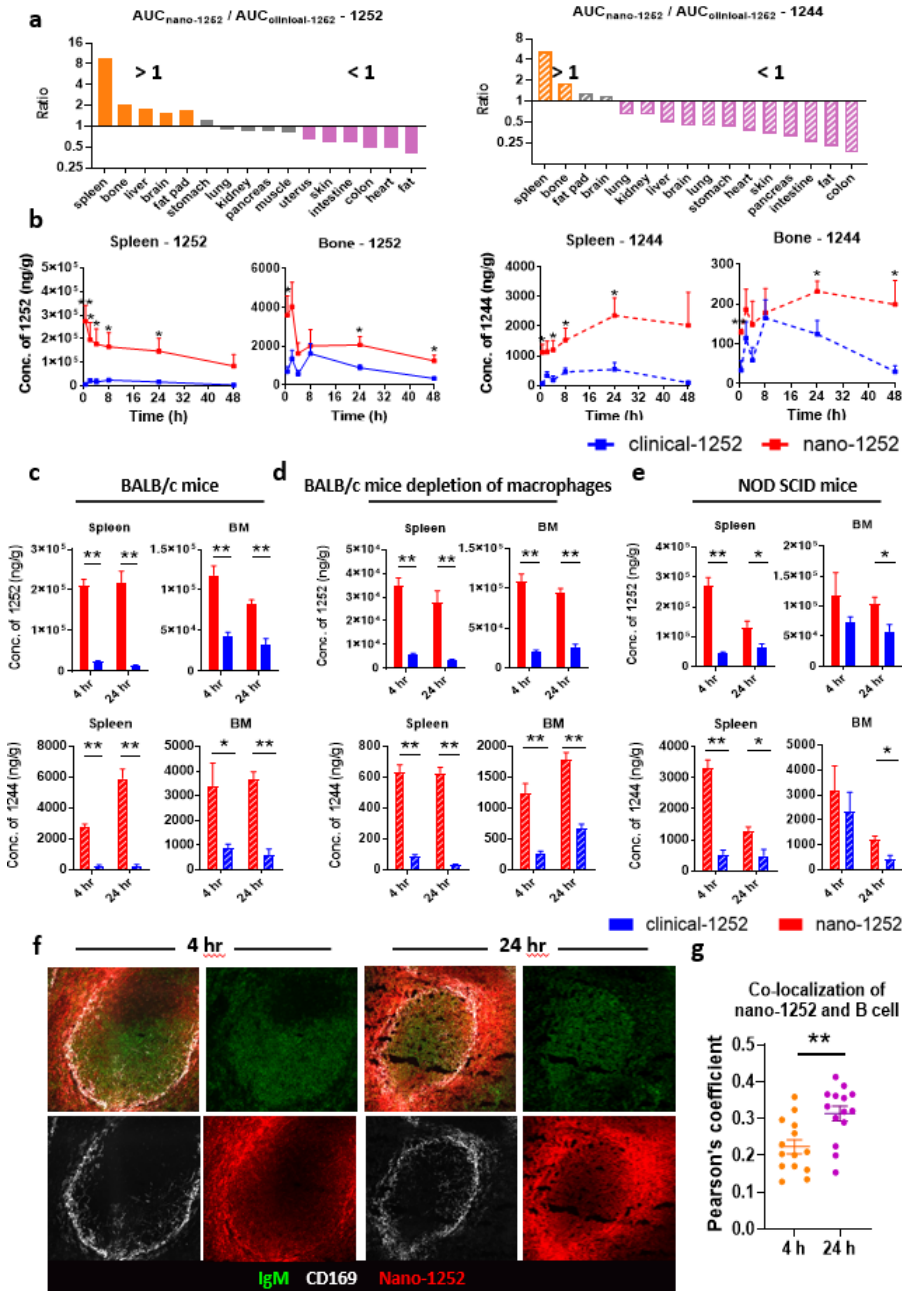


Figure 2.3. Nano-1252 altered biodistribution pattern from clinical-1252 and enhanced spleen and BM selectivity. a AUC ratio of APG-1252 or APG-1244 between nano-1252 and clinical-1252 in different tissues. Average concentration data in each time point was used for the calculation of AUC (non-compartment model). Bars with ratio larger than 1, around 1 or smaller than 1 were colored with orange, gray or magenta. b Concentration-time profile of APG-1252 and APG-1244 in spleen and bone samples from treatment groups. Two formulations were intravenously administered to CD-1 mice ( $n=5$  per time point) with dosage as 50 mg/kg (10 mg/ml). Data are represented as mean  $\pm$  SEM (two-tailed t-test in each time point). c-e Concentration of APG-1252 and APG-1244 in spleen and BM from BALB/c mice (c), BALB/c mice with macrophages depleted (d) and NOD SCID mice (e). Two formulations were intravenously administered ( $n=3$  per time point) with dosage as 50 mg/kg (10 mg/ml). Data are represented as mean  $\pm$  SEM (two-tailed t-test in each time point). f Confocal images of spleen tissue from BALB/c mice after administration of fluorescent nano-1252. Selected area from whole tissue slides (Supplementary Fig. 7) was presented. g Co-localization analysis of nano-1252 and B cell in spleens at different time points. Different area from the whole tissue slides (Supplementary Fig. 7) was selected for Pearson's coefficient analysis using ImageJ software. Data are represented as mean  $\pm$  SEM (two-tailed t-test). Asterisks indicate the following p-value: \*  $< 0.05$ , \*\*  $< 0.01$ .



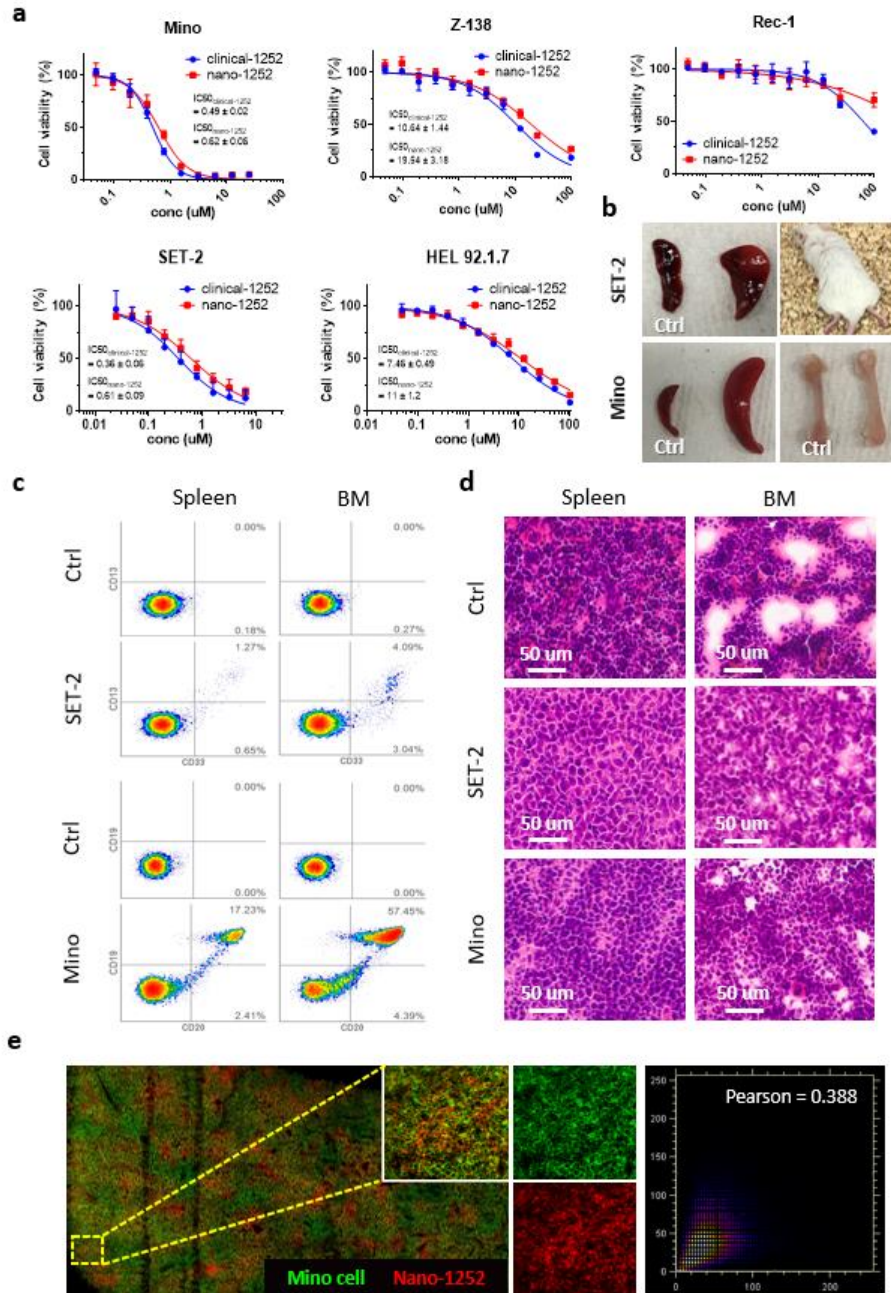


Figure 2.4. Establishment of tumor model with disease progression occurred in spleen and BM. a Cytotoxicity of nano-1252 and clinical-1252 in lymphoma cells (Mino, Z-138 and Rec-1) and MPNs cells (SET-2 and HEL 92.1.7). Raw data are represented as mean  $\pm$  SEM (N=6) and IC50 are represented as mean  $\pm$  95% CI. IC50 was calculated using dose-response nonlinear fit with variable Hill Slope. b Photo images of enlarged spleen, paralyzed mice and white bone from disease mice model. NOD.Cg-Prkdcscid IL2rgtm1Wjl/SzJ mice were injected with  $5 \times 10^6$  Mino cells or  $5 \times 10^6$  SET-2 cells, and photos were captured at day 45 after inoculation. c Flow cytometry of tumor infiltration in spleen and BM from disease mice model (established as before). Representative figures were selected with quantification of tumor infiltration percentage shown in Supplementary Fig. 8d. Double positive cells (anti-human CD13+/anti-human CD33+, anti-human CD19+/anti-human CD20+) were labeled as tumor cells. d H&E staining of spleen and BM from blank and disease mice model (established as before). e Confocal image of distribution of fluorescent nano-1252 in spleen from Mino tumor mice. Tumor cells were labeled as green (FITC anti-human CD20) and formulation was labeled as red (DiD dye). Co-localization coefficient was analyzed between tumor cells and nano-1252.

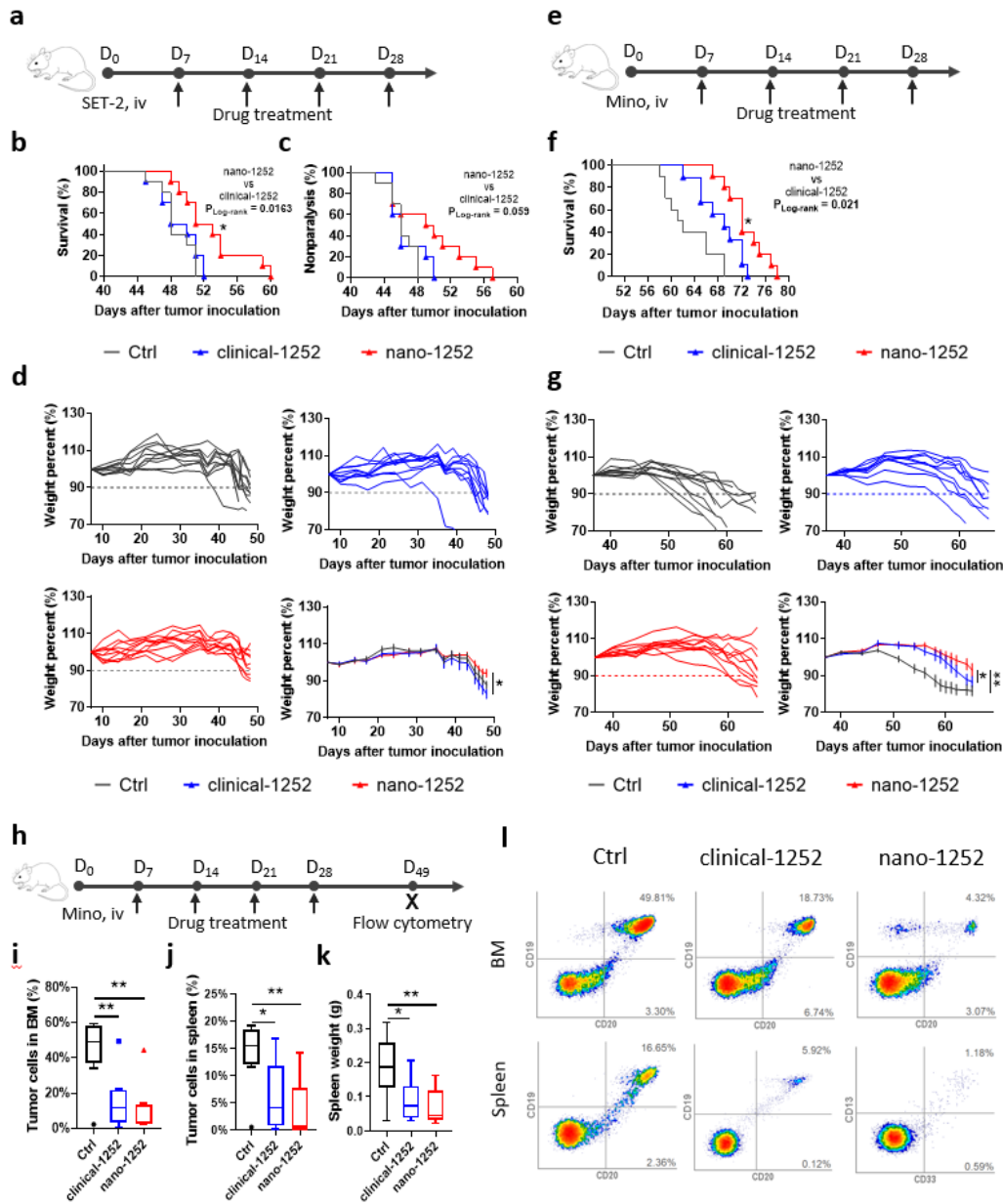


Figure 2.5. Enhanced anti-tumor efficacy of nano-1252 in MPNs and mantle cell lymphoma mice model. **a** Time schedule of tumor inoculation and drug treatment in SET-2 mice model. **b** Survival rate comparison among control, clinical-1252 and nano-1252 groups (N=10 mice per group). Log-rank test was used to analyze the P value between nano-1252 and clinical-1252 survival curves. **c** Non-paralysis rate comparison among control, clinical-1252 and nano-1252 groups (N=10 mice per group). Log-rank test was used to analyze the P value between nano-1252 and clinical-1252 non-paralysis curves. **d** Weight change comparison among control, clinical-1252 and nano-1252 groups. Data in summarized graph were presented as mean  $\pm$  SEM (N=10, ANOVA test with multiple comparisons and adjusted P value). **e** Time schedule of tumor inoculation and drug treatment in Mino mice model. **f** Survival rate comparison among control, clinical-1252 and nano-1252 groups (N=10 mice per group). Log-rank test was used to analyze the P value between nano-1252 and clinical-1252 survival curves. **g** Weight change comparison among control, clinical-1252 and nano-1252 groups. Data in summarized graph were presented as mean  $\pm$  SEM (N=10, ANOVA test with multiple comparisons and adjusted P value). **h** Time schedule of tumor inoculation, drug treatment and flow cytometry in Mino mice model. **i-k** Comparison of tumor infiltration in BM (**i**), spleen (**j**) and spleen weight (**k**) in control, clinical-1252 and nano-1252 groups. Box-and-whisker plots were used to present the data (N=8 per group, ANOVA test with multiple comparisons and adjusted P value). **l** Representative flow cytometry results (median value) from experiment **h** were presented. Asterisks indicate the following p-value: \* < 0.05, \*\* < 0.01.

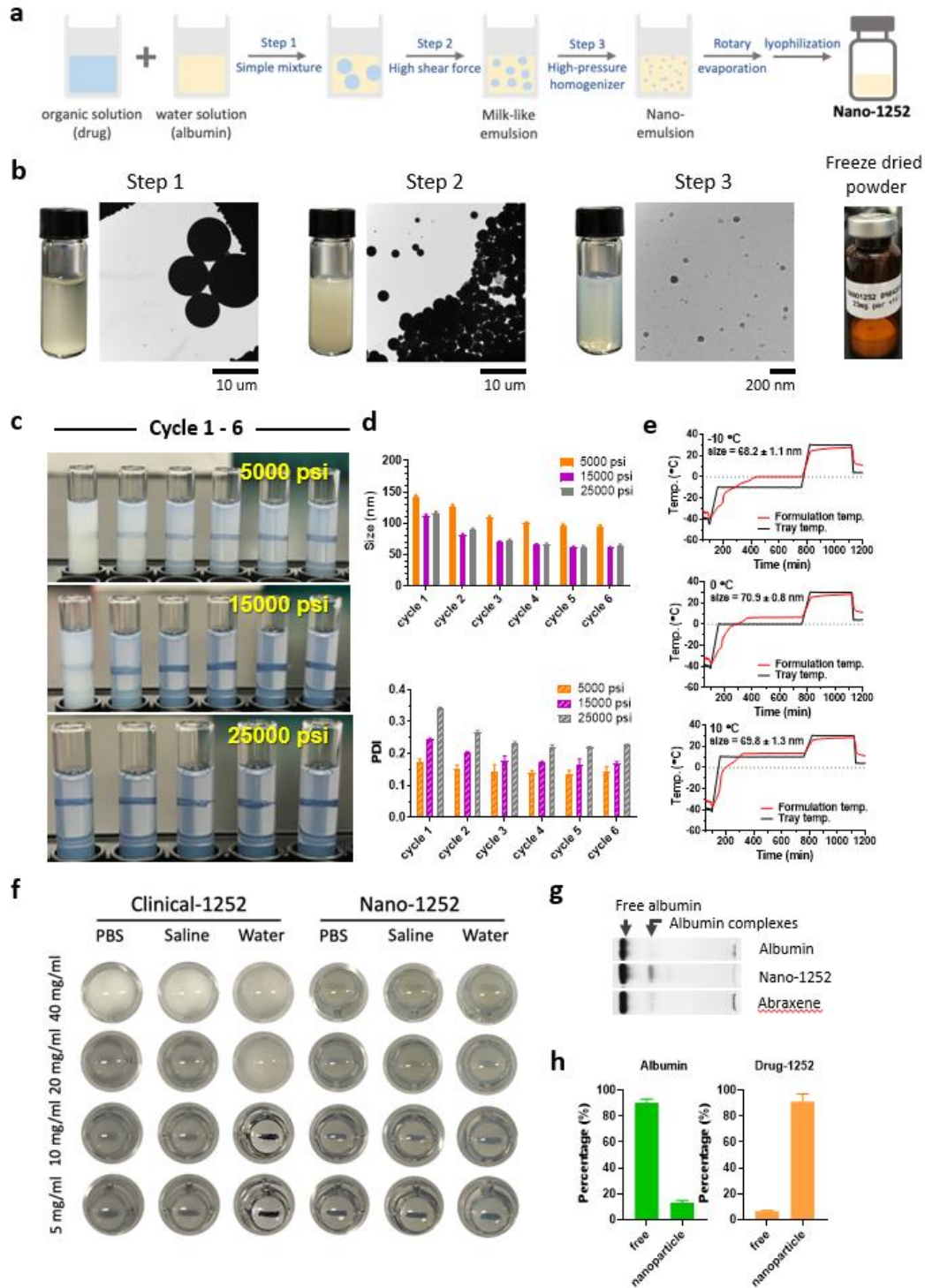


Figure 2.S1. Preparation and characterization of nano-1252. a Preparation process of nano-1252. b TEM images and appearance of nano-formulations prepared at different steps from a. c-d Appearance (c) and size distribution (d) of nano-1252 during different processing cycles and pressure in high-pressure homogenizer step. Data were represented as mean  $\pm$  SEM (N=3). e Temperature change of formulation environment during freeze drying process when primary drying temperature set as  $-10^{\circ}\text{C}$ ,  $0^{\circ}\text{C}$  or  $10^{\circ}\text{C}$ . f Appearance of clinical-1252 and nano-1252 after resuspension with PBS, saline or water. g Native gel analysis of free albumin, nano-1252 and abraxane. h Composition of albumin and APG-1252 in free/simple albumin complexes or nanoparticles.

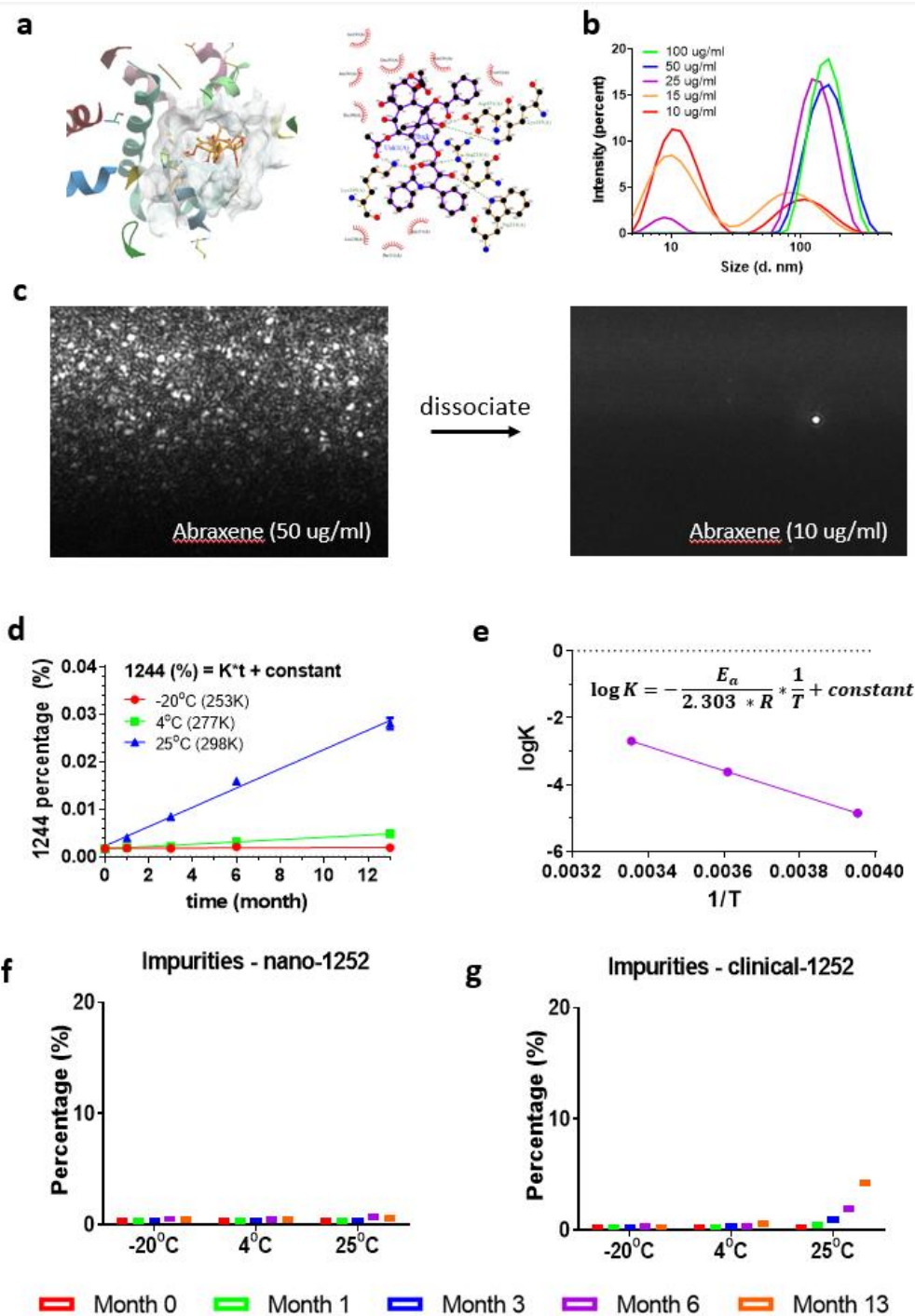


Figure 2.S2. Low physical stability of abraxane and chemical stability of clinical-1252. a Docking simulation between paclitaxel and albumin protein (2BXX). b Stability of abraxane after being diluted from 5 mg/ml to 10 ug/ml with saline. DLS was used to test the size distribution. c Microscope images of the movement of abraxane with concentration from 50 ug/ml to 10 ug/ml by Nanoparticle Tracking Analysis (NTA). Formulations were diluted from 5 mg/ml with saline. d APG-1244 percentage change for nano-1252 during storage period under -20°C, 4°C or 25°C (N=3). Zero order generation of APG-1244 was hypothesized to calculate the rate constant K. e Relationship between logK and 1/T for APG-1244 generation matches Arrhenius equation. f-g Generation of impurities during storage was compared between nano-1252 and clinical-1252 (N=3).

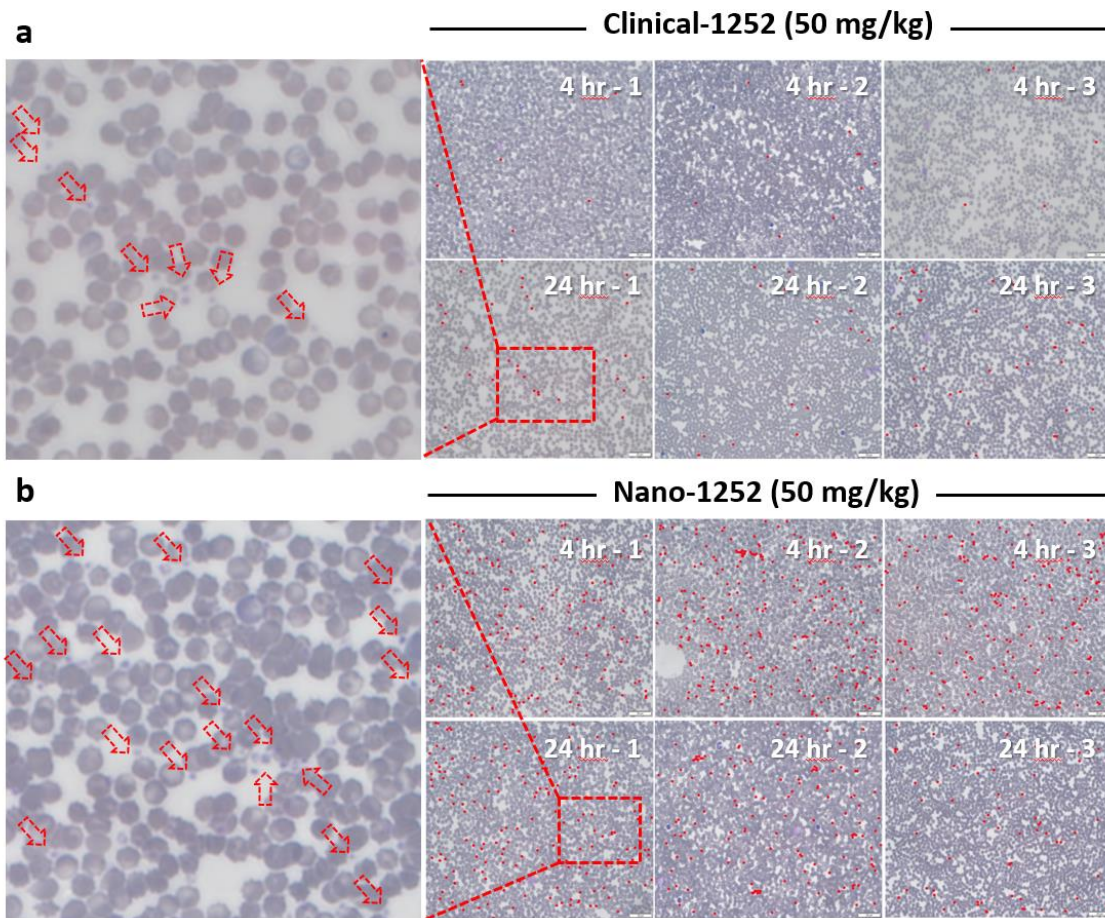


Figure 2.S3. Microscope images of blood cells and platelets for clinical-1252 (a) and nano-1252 (b) at 4 hr or 24 hr.

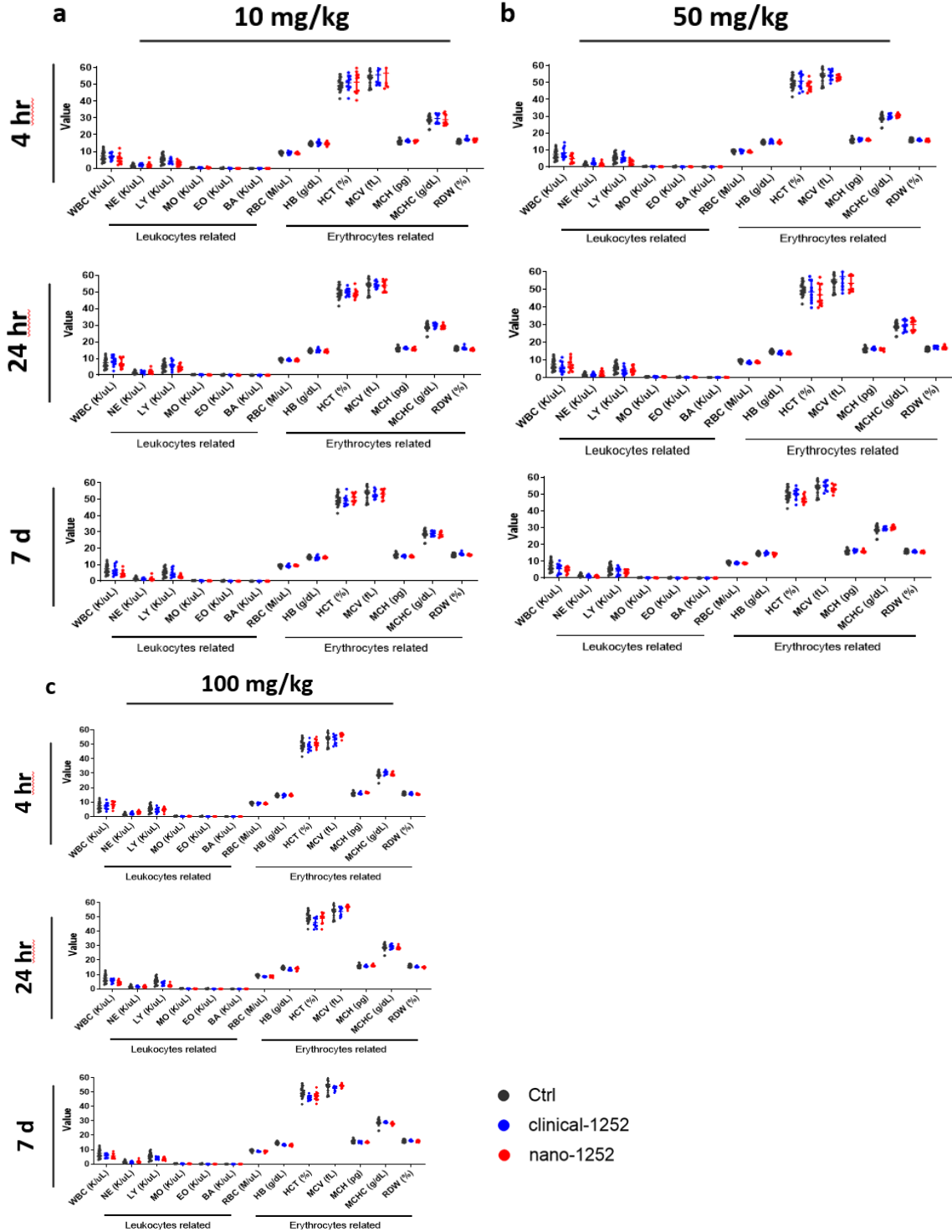


Figure 2.S4. Complete blood count (CBC) analysis of clinical-1252 and nano-1252. CD-1 mice were iv injected with different formulations at dosage of 10 mg/kg (a), 50 mg/kg (b) or 100 mg/kg (c). Blood from administered mice were collected at pre-determined schedule (4 hr, 24 hr and 7d) and analyzed the composition change related to leukocytes or erythrocytes. Data were represented as mean  $\pm$  SEM (N=10 for treatment groups). Blood from blank mice were also collected as the control group (N=20) for different conditions.

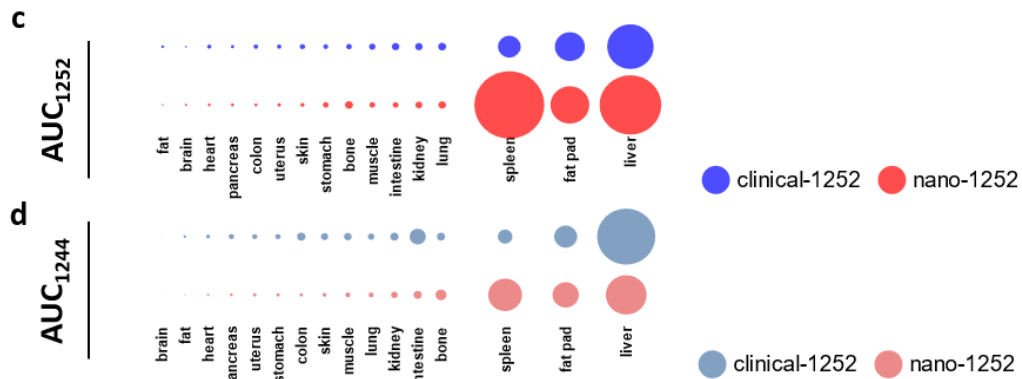
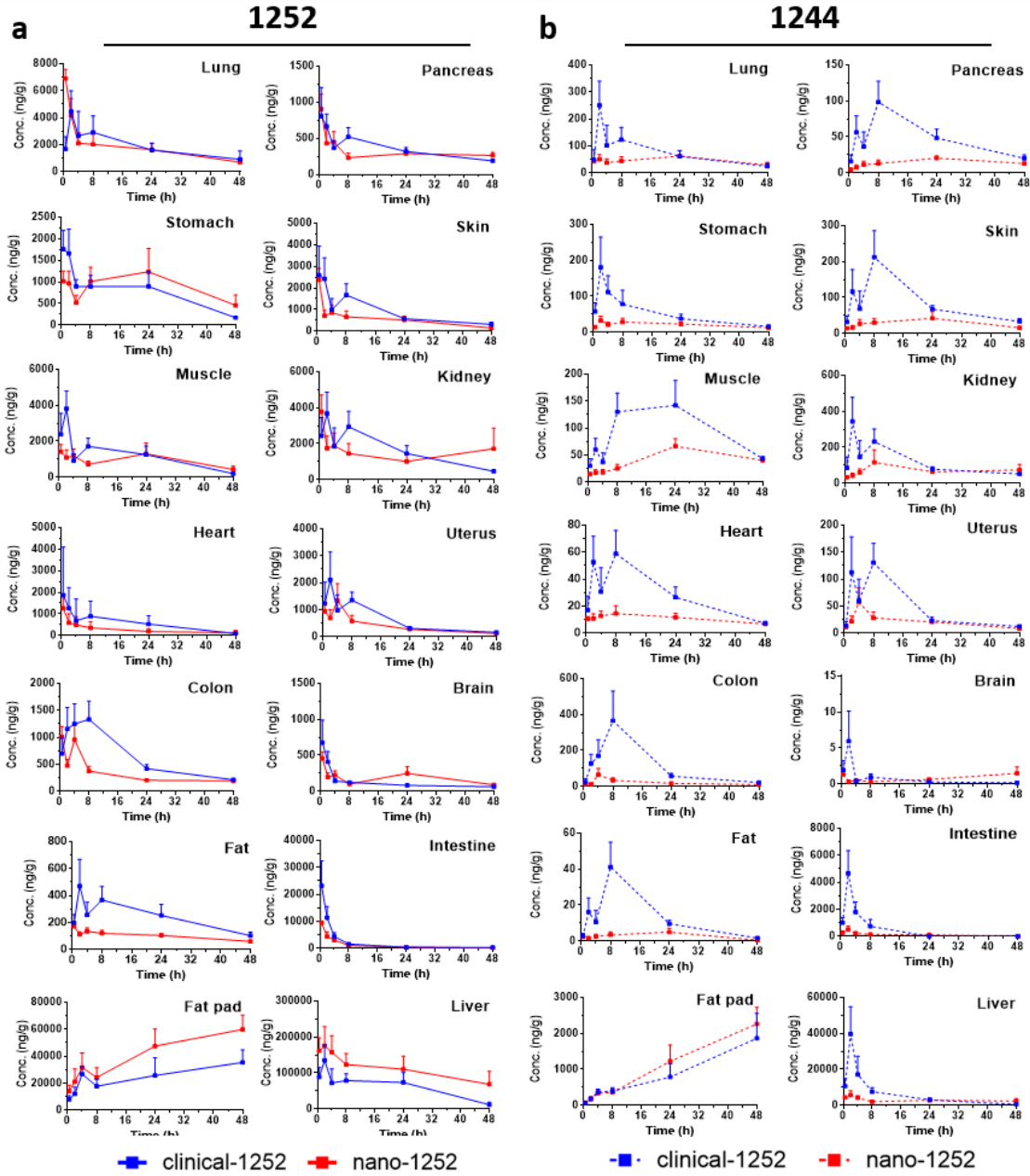


Figure 2.S5. Tissue distribution of clinical-1252 and nano-1252. a-b Concentration-time profile of APG-1252 (a) and APG-1244 (b) from both formulations in tissues like lung, pancreas, stomach, skin, muscle, kidney, heart, uterus, colon, brain, fat, intestine, fat pad and liver. c-d AUC comparison of APG-1252 (c) and APG-1244 (d) from both formulations in tissues like a and b. Size of circles represented the value of calculated AUC through non-compartment model.

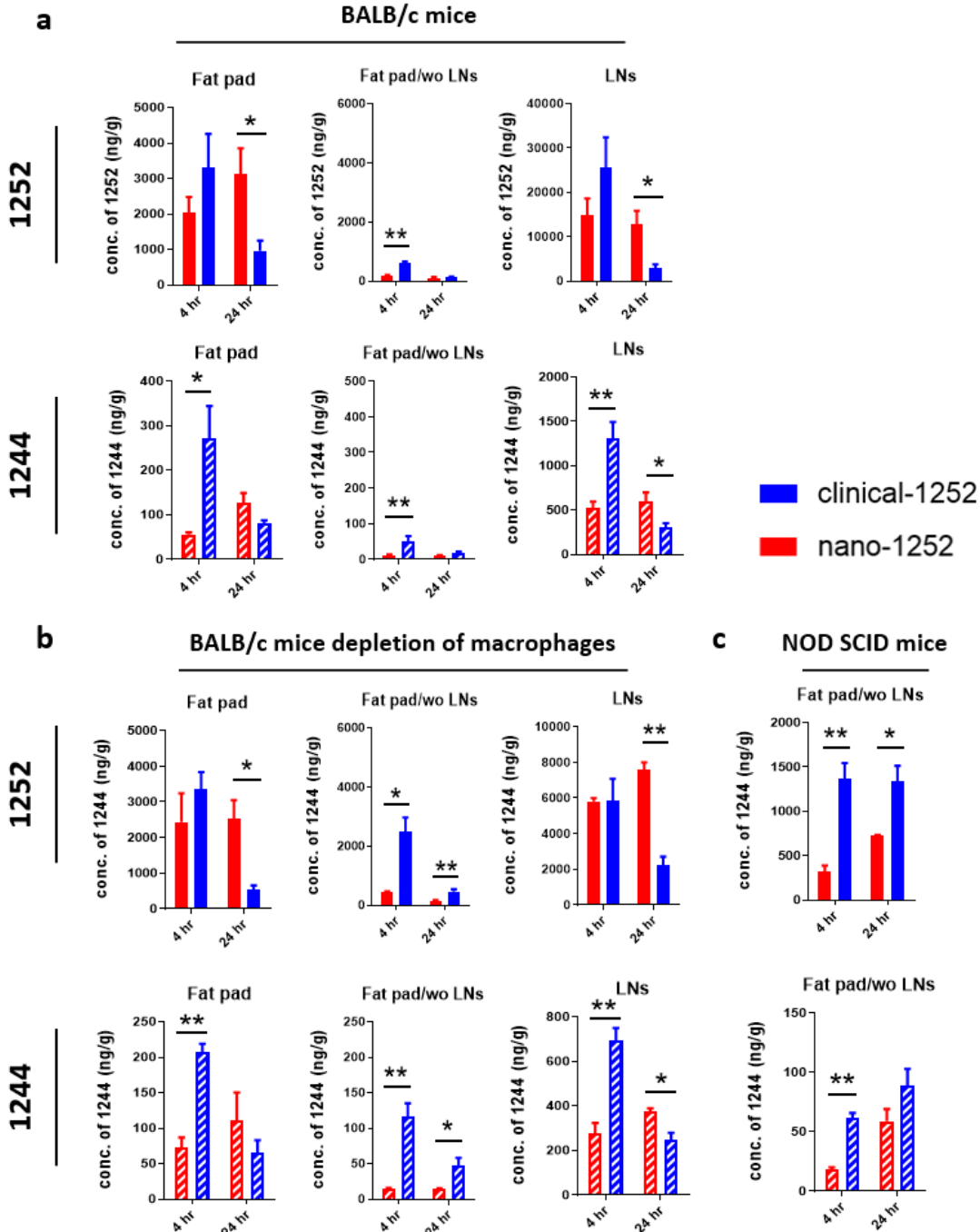
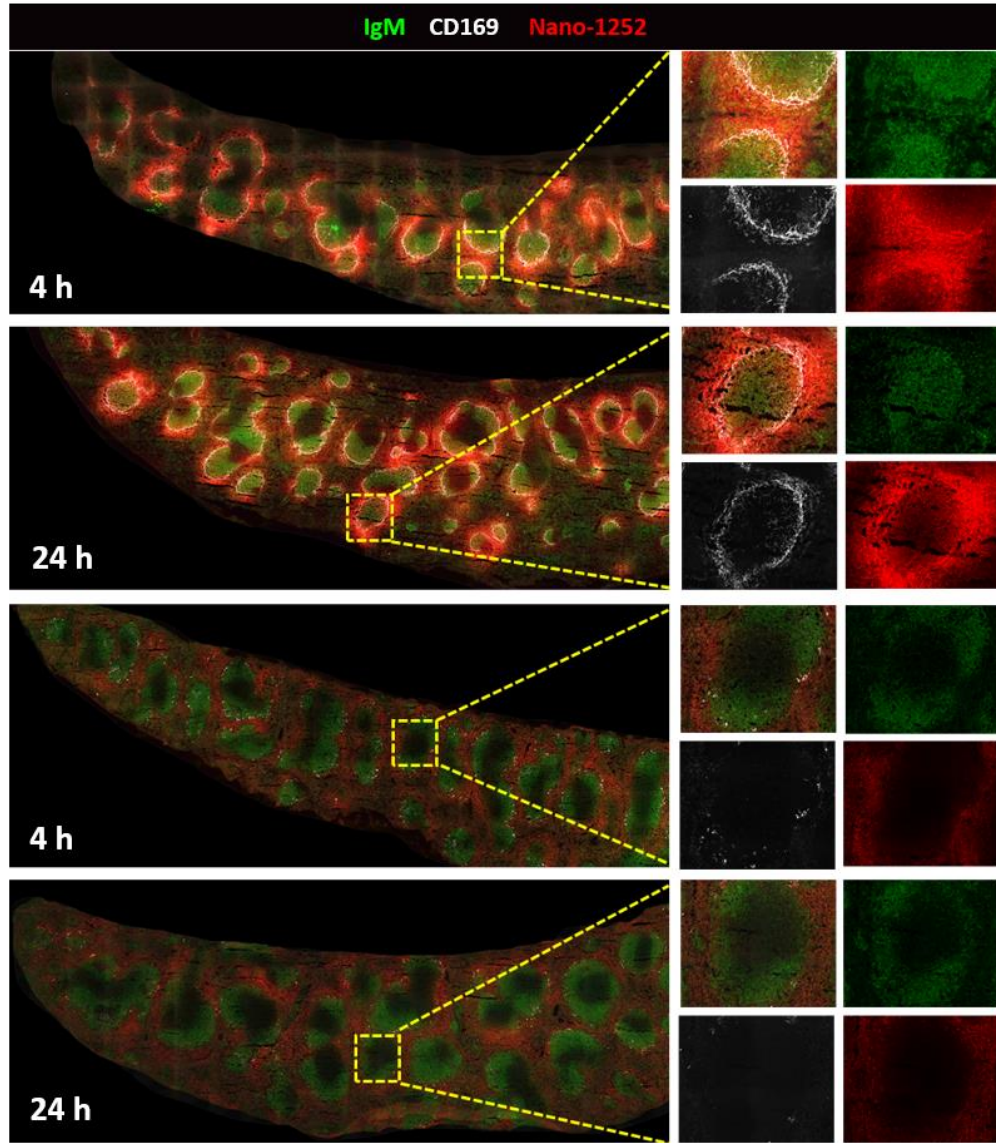


Figure 2.S6. Tissue distribution of clinical-1252 and nano-1252 in fat pad, fat pad without lymph nodes (fat pad/wo LNs) and lymph nodes (LNs). BALB/c mice (a), BALB/c mice depleted with macrophages (b) and NOD SCID (c) mice were iv injected with both formulations at dosage of 50 mg/kg. At scheduled time point (4 hr and 24 hr), selected tissues were collected for analysis of APG-1252 and APG-1244. Data were represented as mean  $\pm$  SEM (N=3-4 for treatment groups). Asterisks indicate the following p-value: \* < 0.05, \*\* < 0.01.



BALB/c mice

BALB/c mice depletion of macrophages



NOD SCID mice

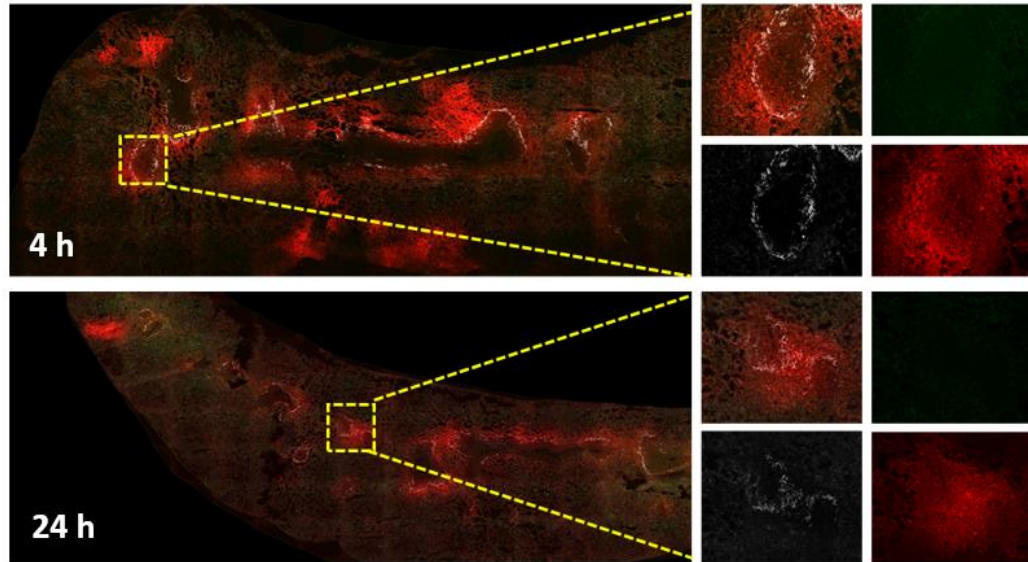


Figure 2.S7. Confocal images of the fluorescent nano-1252 distribution in spleens from BALB/c mice, BALB/c mice depleted with macrophages and NOD SCID mice. Whole spleen sections were stained for images presentation.

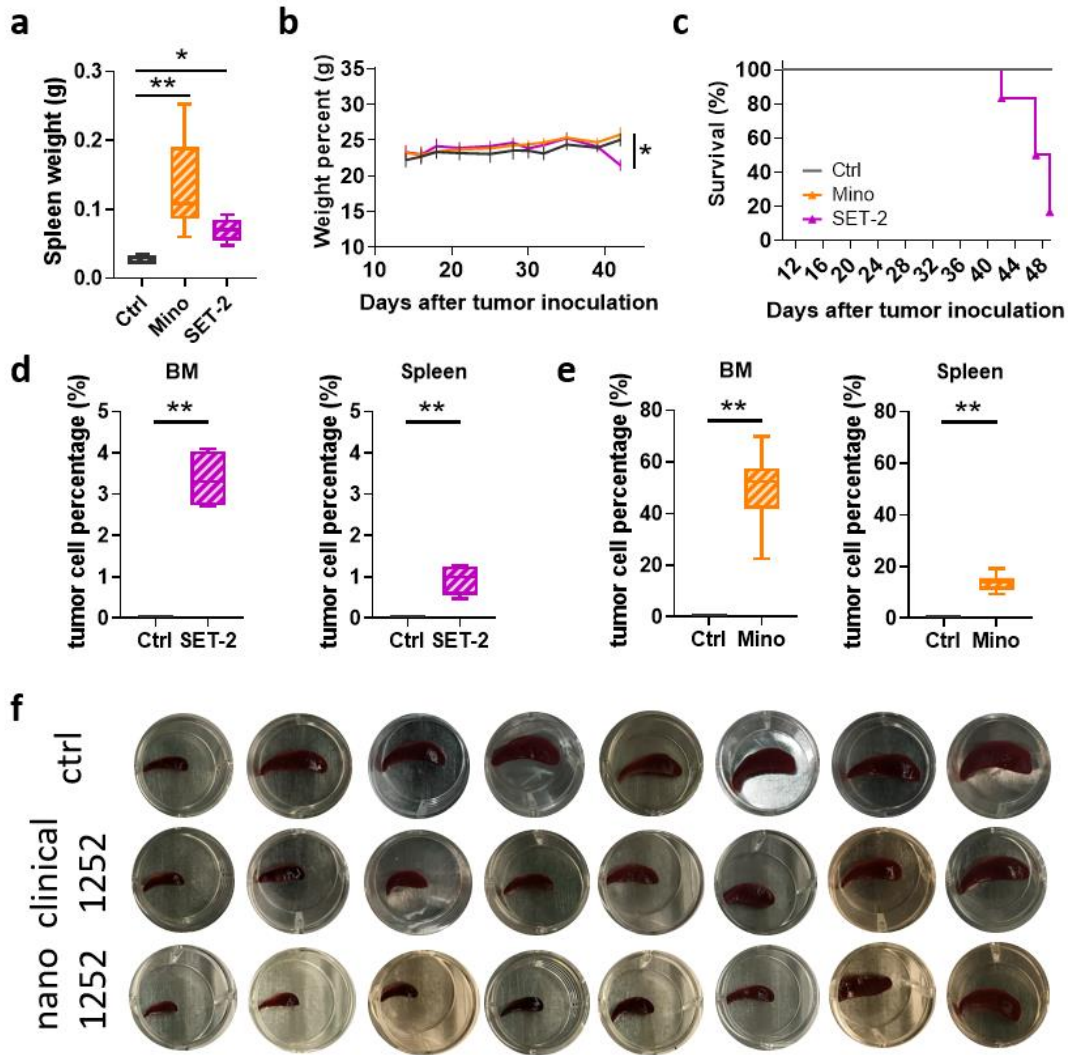


Figure 2.S8. Establishment of tumor model with disease progression in spleen and BM. a Spleen weight change among control, Mino and SET-2 model groups. NOD.Cg-Prkdcscid IL2rgtm1Wjl/SzJ mice were iv injected with  $5 \times 10^6$  Mino cells or  $5 \times 10^6$  SET-2 cells. At day 45, spleens from different groups were collected for weight comparison. Data were represented as mean  $\pm$  SEM (N=4-8 for each group, ANOVA test with multiple comparisons against ctrl group and adjusted P value). b Weight change comparison among control, Mino and SET-2 model groups. Data were represented as mean  $\pm$  SEM (N=4-8 for each group, ANOVA test with multiple comparisons against ctrl group and adjusted P value) Data were represented as mean  $\pm$  SEM (N=4-8 for each group, t test with between ctrl group and SET-2 group). c Survival rate comparison among ctrl, Mino and SET-2 groups. d Percentage of tumor cell infiltration in BM and spleen from SET-2 tumor mice model (N=4-8, two-tailed t test). e Percentage of tumor cell infiltration in BM and spleen from Mino tumor mice model (N=4-8, two-tailed t test). f Appearance of spleens from Mino tumor model after treatment of blank, clinical-1252 and nano-1252. NOD.Cg-Prkdcscid IL2rgtm1Wjl/SzJ mice were iv injected with  $5 \times 10^6$  Mino cells at day 0 and then treated with clinical-1252 or nano-1252 (40 mg/kg) once per week for 4 consecutive weeks. At day 49, mice were sacrificed and their spleens were collected for comparison. Asterisks indicate the following p-value: \* < 0.05, \*\* < 0.01.

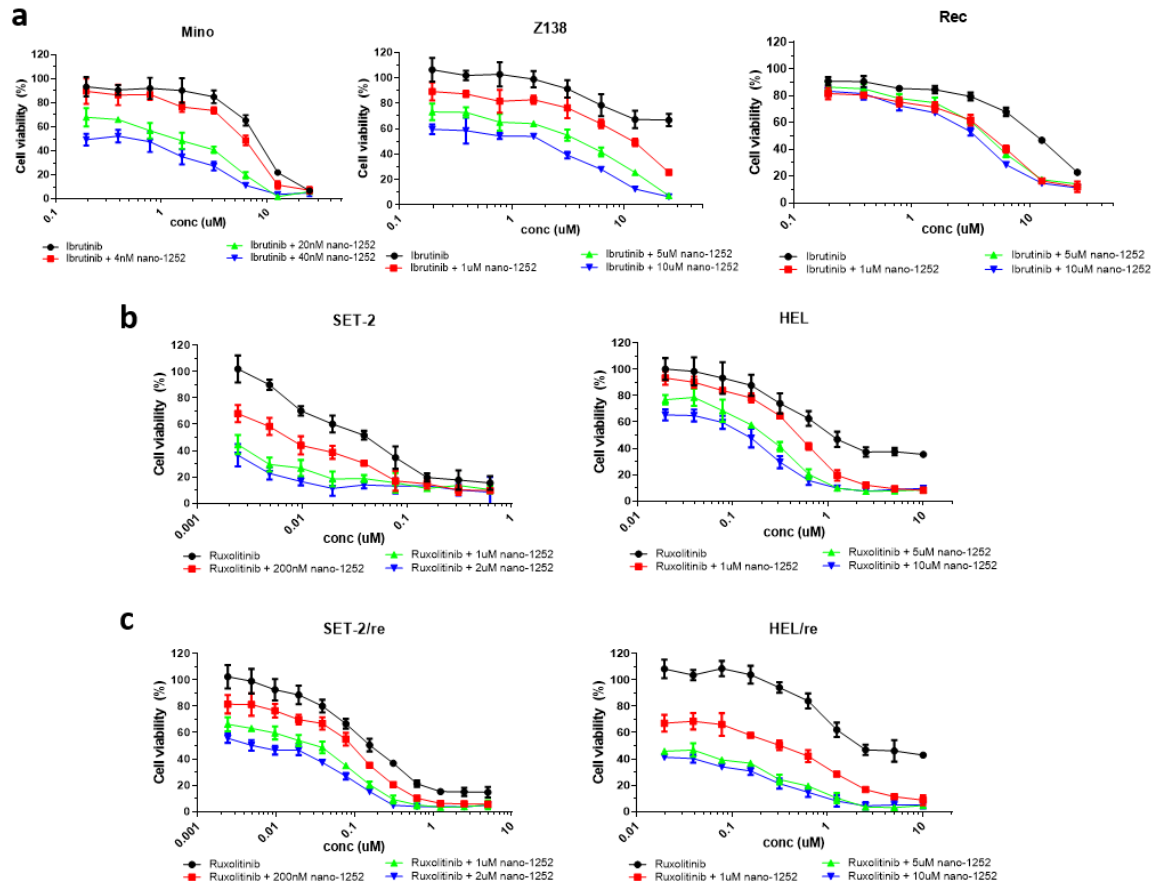


Figure 2.S9. Cytotoxicity of nano-1252 combined with other drugs against lymphoma or MPNs cell lines. a Inhibition of nano-1252 combined with BTK inhibitor, ibrutinib, in lymphoma cells lines including Mino, Z138 and Rec. Data were represented as mean  $\pm$  SEM (N=6). b-c Inhibition of nano-1252 combined with JAK2 inhibitor, ruxolitinib, in original (b) or drug-induced resistant (c) MPNs cell lines (SET-2 and HEL 92.1.7, SET-2/re and HEL 92.1.7/re). Data were represented as mean  $\pm$  SEM (N=6).

## 2.7 Bibliography

1. Muller, P.Y. & Milton, M.N. The Determination and Interpretation of the Therapeutic Index in Drug Development. *Nature reviews. Drug discovery* 11, 751-761 (2012).
2. Mead, A.J. & Mullally, A. Myeloproliferative neoplasm stem cells. *Blood* 129, 1607-1616 (2017).
3. Mullally, A. et al. Physiological Jak2V617F expression causes a lethal myeloproliferative neoplasm with differential effects on hematopoietic stem and progenitor cells. *Cancer Cell* 17, 584-596 (2010).
4. Tefferi, A. & Pardanani, A. Myeloproliferative Neoplasms: A Contemporary Review. *JAMA oncology* 1, 97-105 (2015).
5. Plosker, G.L. Ruxolitinib: a review of its use in patients with myelofibrosis. *Drugs* 75, 297-308 (2015).
6. Petiti, J. et al. Bcl-xL represents a therapeutic target in Philadelphia negative myeloproliferative neoplasms. *Journal of cellular and molecular medicine* 24, 10978-10986 (2020).
7. Takei, H. et al. Suppression of multiple anti-apoptotic BCL2 family proteins recapitulates the effects of JAK2 inhibitors in JAK2V617F driven myeloproliferative neoplasms. *Cancer science* (2021).
8. Schieber, M., Crispino, J.D. & Stein, B. Myelofibrosis in 2019: moving beyond JAK2 inhibition. *Blood Cancer Journal* 9, 74 (2019).
9. Youle, R.J. & Strasser, A. The BCL-2 protein family: opposing activities that mediate cell death. *Nature reviews. Molecular cell biology* 9, 47-59 (2008).
10. Waibel, M. et al. Combined targeting of JAK2 and Bcl-2/Bcl-xL to cure mutant JAK2-driven malignancies and overcome acquired resistance to JAK2 inhibitors. *Cell Rep* 5, 1047-1059 (2013).
11. Harrison, C.N. et al. Results from a Phase 2 Study of Navitoclax in Combination with Ruxolitinib in Patients with Primary or Secondary Myelofibrosis. *Blood* 134, 671-671 (2019).
12. Pemmaraju, N. et al. Trial in Progress: Phase Ib/II Study of Bcl-2/Bcl-XI Inhibitor Pelcitoclax (APG-1252) in Patients with Myelofibrosis (MF) That Progressed after Initial Therapy. *Blood* 136, 15-16 (2020).
13. Potluri, J., Harb, J., Masud, A.A. & Hutti, J.E. A Phase 3, Double-Blind, Placebo-Controlled, Randomized Study Evaluating Navitoclax in Combination with Ruxolitinib in Patients with Myelofibrosis (TRANSFORM-1). *Blood* 136, 4 (2020).
14. Mason, K.D. et al. Programmed anuclear cell death delimits platelet life span. *Cell* 128, 1173-1186 (2007).
15. Schoenwaelder, S.M. et al. Bcl-xL-inhibitory BH3 mimetics can induce a transient thrombocytopenia that undermines the hemostatic function of platelets. *Blood* 118, 1663-1674 (2011).
16. Delbridge, A.R.D., Grabow, S., Strasser, A. & Vaux, D.L. Thirty years of BCL-2: translating cell death discoveries into novel cancer therapies. *Nature Reviews Cancer* 16, 99-109 (2016).

17. Roberts, A.W. et al. Substantial Susceptibility of Chronic Lymphocytic Leukemia to BCL2 Inhibition: Results of a Phase I Study of Navitoclax in Patients With Relapsed or Refractory Disease. *JOURNAL OF CLINICAL ONCOLOGY* 30, 488-496 (2012).
18. Wilson, W.H. et al. Navitoclax, a targeted high-affinity inhibitor of BCL-2, in lymphoid malignancies: a phase 1 dose-escalation study of safety, pharmacokinetics, pharmacodynamics, and antitumour activity. *LANCET ONCOLOGY* 11, 1149-1159 (2010).
19. Suvarna, V., Singh, V. & Murahari, M. Current overview on the clinical update of Bcl-2 anti-apoptotic inhibitors for cancer therapy. *European journal of pharmacology* 862, 172655 (2019).
20. Luo, F. et al. Gemcitabine and APG-1252, a novel small molecule inhibitor of BCL-2/BCL-XL, display a synergistic antitumor effect in nasopharyngeal carcinoma through the JAK-2/STAT3/MCL-1 signaling pathway. *Cell death & disease* 12, 772 (2021).
21. Wang, H. et al. 544 Preclinical studies of a dual Bcl-2/Bcl-xL inhibitor APG-1252 with strong anti-tumor efficacy and significantly reduced platelet toxicity. 50, 176-177 (2014).
22. Lakhani, N.J. et al. First-in-human study of palcitoclax (APG-1252), a novel dual Bcl-2/Bcl-xL inhibitor, demonstrated advantages in platelet safety while maintaining anticancer effect in U.S. patients with metastatic solid tumors. *Journal of Clinical Oncology* 38, 3509-3509 (2020).
23. Chaudhary, N., Weissman, D. & Whitehead, K.A. mRNA vaccines for infectious diseases: principles, delivery and clinical translation. *Nat Rev Drug Discov* 20, 817-838 (2021).
24. Hou, X., Zaks, T., Langer, R. & Dong, Y. Lipid nanoparticles for mRNA delivery. *Nature reviews. Materials*, 1-17 (2021).
25. Song, M.K., Park, B.B. & Uhm, J.E. Understanding Splenomegaly in Myelofibrosis: Association with Molecular Pathogenesis. *INTERNATIONAL JOURNAL OF MOLECULAR SCIENCES* 19 (2018).
26. Tefferi, A. Primary myelofibrosis: 2017 update on diagnosis, risk-stratification, and management. *AMERICAN JOURNAL OF HEMATOLOGY* 91, 1262-1271 (2016).
27. Yardley, D.A. nab-Paclitaxel mechanisms of action and delivery. *Journal of controlled release : official journal of the Controlled Release Society* 170, 365-372 (2013).
28. Wolfram, J. & Ferrari, M. Clinical cancer nanomedicine. *Nano Today* 25, 85-98 (2019).
29. Kratz, F. Albumin as a drug carrier: design of prodrugs, drug conjugates and nanoparticles. *Journal of controlled release : official journal of the Controlled Release Society* 132, 171-183 (2008).
30. Korniluk, A., Koper-Lenkiewicz, O.M., Kamińska, J., Kemon, H. & Dymicka-Piekarska, V. Mean Platelet Volume (MPV): New Perspectives for an Old Marker in the Course and Prognosis of Inflammatory Conditions. *Mediators of inflammation* 2019, 9213074 (2019).

31. Blanco, E., Shen, H. & Ferrari, M. Principles of nanoparticle design for overcoming biological barriers to drug delivery. *Nature biotechnology* 33, 941-951 (2015).
32. Kale, J., Osterlund, E.J. & Andrews, D.W. BCL-2 family proteins: changing partners in the dance towards death. *CELL DEATH AND DIFFERENTIATION* 25, 65-80 (2018).
33. Gustafson, H.H., Holt-Casper, D., Grainger, D.W. & Ghandehari, H. Nanoparticle uptake: The phagocyte problem. *NANO TODAY* 10, 487-510 (2015).
34. Hu, G.R. et al. Nanoparticles Targeting Macrophages as Potential Clinical Therapeutic Agents Against Cancer and Inflammation. *FRONTIERS IN IMMUNOLOGY* 10 (2019).
35. McKenzie, C.V., Colonne, C.K., Yeo, J.H. & Fraser, S.T. Splenomegaly: Pathophysiological bases and therapeutic options. *INTERNATIONAL JOURNAL OF BIOCHEMISTRY & CELL BIOLOGY* 94, 40-43 (2018).
36. Ye, H.G. et al. Smoldering mantle cell lymphoma. *JOURNAL OF EXPERIMENTAL & CLINICAL CANCER RESEARCH* 36 (2017).
37. Angelopoulou, M.K. et al. The splenic form of mantle cell lymphoma. *EUROPEAN JOURNAL OF HAEMATOLOGY* 68, 12-21 (2002).
38. Tam, C.S. et al. Ibrutinib plus Venetoclax for the Treatment of Mantle-Cell Lymphoma. *NEW ENGLAND JOURNAL OF MEDICINE* 378, 1211-1223 (2018).

## CHAPTER III – Drug Optimization of Anti-SARS-Cov-2 Candidate to Improve Lung Targeting and Enhance Efficacy in Treatment of COVID-19

### Authors:

*Hongxiang Hu<sup>1,#</sup>, Mohamed Dit Mady Traore<sup>1,#</sup>, Ruiting Li<sup>1</sup>, Hebao Yuan<sup>1</sup>, Miao He<sup>1</sup>, Bo Wen<sup>1</sup>, Wei Gao<sup>1</sup>, Colleen B Jonsson<sup>2</sup>, Elizabeth A Fitzpatrick<sup>2</sup>, Duxin Sun<sup>1,\*</sup>*

### 3.1 Abstract

COVID-19 patients with severe symptoms still lack antiviral treatment options. Although remdesivir is the only FDA approved drug in treating severe disease of COVID-19, its efficacy is limited by premature hydrolysis to NUC, low accumulation in the disease targeted tissue (lung) and low antiviral potency. In this study, we synthesized new series prodrugs of remdesivir by modifying prodrug moiety using ProTide strategy. The lead compound MMT5-14, in comparison with remdesivir, increased prodrug concentration by 300-fold and 200-fold in the plasma and lung of hamsters by reducing premature hydrolysis to nucleoside (NUC), enhanced accumulation of active metabolite triphosphate nucleosides (NTP) in the lung by 5-fold in hamster. MMT5-14 increased intracellular uptake and activation in lung epithelial cells by 25-fold compared to remdesivir. Further, MMT5-14 showed 4-7-fold higher antiviral activity than remdesivir in SARS-CoV-2 and different variants. MMT5-14 is a potential antiviral drug to treat severe disease in hospitalized COVID-19 patients.

### 3.2 Introduction

---

1 Department of Pharmaceutical Sciences, College of Pharmacy, University of Michigan, 1600 Huron Parkway, North Campus Research Complex, Building 520, Ann Arbor, MI 48109, USA

2 Regional Biocontainment laboratory, University of Tennessee Health Science Center, Memphis, TN 38163

# These authors contributed equally to the work.

\* To whom correspondence should be addressed: duxins@umich.edu



Global pandemic coronavirus disease 2019 (Covid-19), caused by severe acute respiratory syndrome coronavirus 2 (SARS-Cov-2), has infected more than 250 million people and caused 5 million deaths worldwide by December 2021 according to Coronavirus Resource Center in Johns Hopkins University. Despite the recent successful development of antiviral drugs for in treating mild and moderate COVID-19<sup>1,2</sup>, COVID-19 patients with severe disease still lack antiviral effective treatment options. Remdesivir (VEKLURY®), approved by FDA in October 2020, was the only anti-viral drug in COVID-19 patients with severe disease<sup>3,4</sup>. The approval of remdesivir was based on the clinical study ACTT-1 (NCT 04280705), in which subjects with moderate or severe disease showed shorter recovery time (median 10 days vs 15 days in the placebo group, 95% CI of recovery rate ratio is 1.12-1.49), higher odd ratios of improvement at Day 15 (95% CI of odds ratio in the 8-point ordinal scale is 1.25-1.91) and lower mortality at Day 29 (11% vs 15% in the placebo group)<sup>5</sup>. The combination of remdesivir with other clinical interventions, such as immune modulators (e.g. baricitinib or tocilizumab), supplemental oxygen, or SARS-Cov-2-targeting monoclonal antibodies (e.g. Casirivimab, Imdevimab or Sotrovimab), has improved the clinical outcome of COVID-19 patients by reducing fatality rate<sup>6,7</sup>. However, several other clinical trials using remdesivir against SARS-Cov-2, like WHO Solidarity trial<sup>8</sup>, GS-US-540-5773 (NCT04292899)<sup>9</sup>, GS-US-540-5774 (NCT04292730)<sup>10</sup> failed to show any statistical difference between remdesivir treatment group and control group when considering odd ratios of improvement in clinical status (NCT04292730, 10-day administration)<sup>10</sup> or mortality rate (Solidarity trial, 95% CI is 0.81-1.11)<sup>8</sup>.

Remdesivir was designed as a prodrug of nucleoside monophosphate (NMP) using ProTide strategy, which generates active metabolite nucleoside triphosphate (NTP) to inhibit its target RNA-dependent RNA polymerase (RdRp)<sup>11,12</sup>. The prodrug remdesivir is to enhance cell permeability of NMP and overcome the rate limiting step of phosphorylation of nucleoside (NUC) inside cells. The activation of prodrug remdesivir needs a delicate balance between outside and inside cells. Ideally, the intact prodrug remdesivir enters the cells and then is cleaved by intracellular carboxyesterase 1 (CES 1) and phosphoramidases (HINT1-3) to generate NMP that subsequently transform to NTP for its antiviral activity.

Three shortcomings of remdesivir may have contributed to its limited clinical efficacy: (1) premature hydrolysis of remdesivir to nucleoside metabolite (NUC, GS-441524) in plasma may limit its antiviral activity since NUC is 20-fold less potent than remdesivir<sup>13</sup>. Due to the abundance of esterases and phosphatases in the plasma, NUC is the predominant metabolite (100-fold higher than remdesivir) in the plasma after injection of remdesivir<sup>12, 14</sup>. (2) low exposure and selectivity of remdesivir and its active metabolite NTP in the SARS-Cov-2 targeted tissues (such as Lung) may limit its clinical efficacy. The remdesivir was undetectable in the lung while low concentration of NTP was detected in the lung after IV injection<sup>15</sup>. (3) remdesivir still has relative low potency (IC<sub>50</sub>) against SARS-COV-2<sup>16, 17</sup>. Although Remdesivir showed IC<sub>50</sub> against SARS-COV-2 in Calu-3 cells at nM range, its IC<sub>50</sub> in other cells is in the uM range<sup>18</sup>.

In this study, we aim to modify ProTide design by changing the prodrug moiety to synthesize new remdesivir derivatives with better stability, higher lung accumulation, and better antiviral activities. We utilized the following strategy to optimize these compounds: 1) since the first step activation of remdesivir is the hydrolysis of L-alaniate ester and phenolate moiety to generate alanine metabolite (ALA), modifications on these two positions with bulky moieties will likely improve its stability<sup>11, 19</sup>; 2) Long lipid chain modification in molecular structure may improve drug exposure/selectivity in the lung<sup>20</sup>; and 3) Linoleic acid (LA) moiety has been shown to inhibit spike protein and angiotension-converting enzyme 2 (ACE 2) receptor that may further improve anti-SARS-Cov-2 activity<sup>21</sup>. It is known that premature activation of remdesivir to NUC reduces its antiviral activity<sup>13</sup>. However, it is unknown if more stable compounds using ProTide prodrug design of remdesivir may slow down its activation and also reduce its activity. To our surprise, the final optimized compound MMT5-14, which is 3 to 8-fold higher more stable than remdesivir in the plasma and liver microsome, not only achieved more than 10 to 500-fold higher drug concentration and 4 to 5-fold higher active metabolite (NTP) in the target tissues (e.g. Lung) than remdesivir, but also demonstrated 3 to 5-fold higher antiviral activity than remdesivir against SARS-CoV-2 variants. MMT5-14 may have potential to treat COVID-19 with severe disease.

### **3.3 Result and Discussion**

**Modification of prodrug moiety of ProTide remdesivir to generate new analogs.** Five remdesivir derivatives were synthesized following the synthetic route as described in Figure 3.1A. First, esterification of N-Boc-L-alanine with appropriate alcohols (1-dodecanol; benzyl alcohol; cis,cis-9,12-octadecadien-1-ol) provided compounds 1a-c which were subsequently taken into 4 M HCl for Boc deprotection to give intermediates 2 as a salt. Condensation of intermediates 2 with either Phenyl or naphthyl dichlorophosphate, followed by 4-nitrophenol afforded intermediates 3 as ~ 1:1 diastereoisomeric mixture at the phosphorus. Acetonide protection of the 2,3'-hydroxyl moieties of GS-441524 with 2,2-dimethoxypropane in the presence of H<sub>2</sub>SO<sub>4</sub> afforded the intermediate 4. Coupling of intermediate 4 with intermediates 3 in the presence of magnesium chloride and Hünig's base efficiently afforded the intermediates 5 as ~ 1:1 diastereoisomeric mixture. The last step consisted of the acetonide group deprotection of intermediates 5 and provided the final compounds as ~ 1:1 diastereoisomeric mixture in good yields (Figure 3.1B).

**The in vitro plasma and microsomal stability and in vivo stability of new analogs in comparison with remdesivir.** To select more stable analogs in plasma and liver microsome, we tested the five newly synthesized analogs for their stability in plasma and liver microsomes in three different species: human, hamster and mouse. As shown in Figure 3.1C and table 3.1, in comparison with MMT5-70, MMT5-14 with linoleyl alcohol chain improved the plasma stability in human and hamster by 3 to 4-fold, while MMT5-70 with C12 alky chain failed to do so. In comparison of MMT5-15, MMT5-98 and MMT5-1, both MMT5-15 and MMT5-98 improved stability by 3 to 4-fold in human and hamster plasma, while MMT5-1 failed to do so. All compounds degraded rapidly in mouse plasma due to the abundant esterases in mice. This difference in stability was even more significant in liver microsomes. MMT5-14 and MMT5-15 showed the higher stability than remdesivir in all three species microsomes (t<sub>1/2</sub> was 8-20 min in human, 16-60 min in hamster, and 10-13 min in mouse). MMT4-70 and MMT4-98 also degraded slower than remdesivir even though the stability difference was less significant. MMT5-1 showed no difference with remdesivir in microsomal stability.

To further test the stability of these compounds in vivo, all five compounds and remdesivir were dosed in hamster (10 mg/kg) to measure the plasma concentration. As shown in figure 3.1D, MMT5-14 and MMT5-15 achieved the highest concentration in plasma followed by the 12-carbon-chain modified analogs, MMT4-70 and MMT4-98. Remdesivir was metabolized rapidly with 10 to 100-fold less concentration when compared to MMT5-14 or MMT5-15.

**MMT5-14 and MMT5-15 achieved higher drug concentration and active metabolite, NTP in blood and lung.** ProTide type of prodrugs need not only to achieve high drug concentration, but also to generate high concentration of active metabolite (NTP) in the targeted tissues (e.g. Lung) after these prodrugs were dosed in vivo. To select the best lead compound to achieve these goals, we also measured the intact prodrug, alanine metabolite (ALA), released nucleoside (NUC), and active metabolite triphosphate of nucleoside (NTP) after in vivo IV dosing (10 mg/kg) (Figure 3.2A). As shown in Figure 3.2B, three compounds, MMT5-14, MMT5-15, and MMT5-98 showed 8 to 10-fold higher intact prodrug concentration than remdesivir in the lung at 4 hrs post IV dosing. In addition, these three compounds also generated 2 to 4.5-fold higher NTP in the lung than remdesivir. MMT5-14 showed highest level of NTP in the lung in comparison with other compounds, and thus was selected for further studies. (Figure 3.2B).

We generated two different formulations (cyclodextrin formulation and albumin nanoparticle) of MMT5-14 in comparison with clinical formulation of remdesivir in a detailed PK study. As shown in Figure 3.2C, both formulations of MMT5-14 increased plasma concentration of MMT5-14 (more than 300-fold) and decreased the NUC formation by two-fold in the plasma. Since NTP is only formed inside the cells, no NTP was observed in plasma. Interestingly, MMT5-14 increased intact prodrug concentration, ALA, NUC in the blood (2-10 fold) and lung (4-200 fold). These data suggest more MMT5-14 is accumulated than remdesivir into these tissues. More importantly, MMT5-14 generated 4.5-fold higher active metabolite NTP in the lung, 2-fold higher NTP in the blood compared to remdesivir.

**MMT5-14 not only increased tissue exposure but also increased the tissue selectivity of both prodrug and active metabolite NTP in the lung, spleen and blood.** The drug's activity is usually correlated with drug exposures in the disease targeted tissues. To compare the drug exposure in various tissues of MMT5-14 and remdesivir, we calculated and compared the AUC of prodrug, ALA, NUC, and NTP in all tissues (Figure 3.S1-S2). Their exposure (AUC) ratios between MMT5-14 and remdesivir group were shown in Figure 3.3A. The exposure (AUC) ratios of MMT5-14 (both albumin and cyclodextrin formulations) vs. remdesivir were in the range from 8-800 in various tissues, which suggest MMT5-14 was able to increase tissue exposure in most of the tissues. In comparison, the AUC ratio of metabolite ALA from MMT5-14 vs. remdesivir were also higher (1-8) in most tissues.

However, exposure (AUC) ratios of NUC and NTP from MMT5-14 vs. remdesivir were very different. Higher exposure ratios of NUC from MMT5-14 vs. remdesivir were only observed in the lung, spleen and lymph nodes (Figure 3.3A). More importantly, the higher exposure ratios of active metabolite NTP from MMT5-14 vs. remdesivir were only seen in the lung, spleen, blood (2-4.5 fold), which may provide advantage for its activity in these organs.

Further, the balance of drug's efficacy/toxicity is often related to the drug tissue selectivity as calculated by the equation

$$tissue\ selectivity_{i,compound} = \frac{AUC_{i,compound}}{\sum_{all} AUC_{all,compound}}$$

Where AUC<sub>i</sub> represents the AUC of the compound in one specific tissue and  $\sum AUC_{all}$  represents the sum of AUC of the compound in all tissues. Since the whole metabolism pathway (from prodrug to NTP) could influence the actual distribution of MMT5-14 or remdesivir, we added AUC of all compounds together to calculate the tissue selectivity (Figure 3.3B-C). Surprisingly, MMT5-14 showed 5 to 10-fold higher tissue selectivity in lung compared to remdesivir. Increased tissue selectivity could also be observed in the spleen (2-fold), lymph node (1-2 fold).

It is worth noting although both MMT5-14 and remdesivir had large percentage of accumulation in kidney and liver (around 80% in total) while MMT5-14 increased prodrug exposure in these two organs in comparison with remdesivir. However, it is

possible that remdesivir's toxicity is related to high level of NUC and NTP in the kidney and liver (Figure 3.S2). Interestingly, MMT5-14 did not increase either NTP or NUC in comparison with remdesivir (Figure 3.3A). Therefore, the preferred tissue exposure and selectivity of MMT5-14 and NTP may provide advantage to balance efficacy and toxicity in the future clinical patients. We also dosed MMT5-14 (two formulations, 15 mg/kg) by intravenous administration for continuous 9 days. No obvious toxicity was observed in the hamsters (Figure 3.S3).

**MMT5-14 increased epithelial cells uptake.** The cell uptake and intra-cellular activation of MMT5-14 and remdesivir were also performed in lung epithelial cell line Calu-3 in vitro (Figure 3.4A). As expected, much higher (100-fold) intracellular concentration of MMT5-14 was observed than remdesivir. However, the intra-cellular concentrations of ALA and NUC from MMT5-14 2 to 4-fold lower than that from remdesivir. In contrast, the intracellular level of NTP from MMT5-14 was 1 to 2-fold higher than that from remdesivir. The total intracellular concentrations of the MMT5-14 and its metabolites was 16-fold higher than that of remdesivir.

**MMT5-14 demonstrated superior in-vitro antiviral activity.** The antiviral activities of both MMT5-14 and remdesivir were evaluated against four variants of SARS-Cov-2 in Vero-E6 cells (Figure 3.4B). The MMT5-14 showed 7-fold higher anti-viral activity (7-fold lower IC<sub>50</sub>) compared to remdesivir against SARS-Cov-2 as measured by the protection of Vero-E6 cell survival after infection of the virus. MMT5-14 is also active against other variants, which showed 4 to 7-fold higher activity than remdesivir. Both MMT5-14 and remdesivir alone showed very little toxicity in Vero-E6 cells at concentration up to 10uM.

The virus titer reduction by MMT5-14 vs. remdesivir was further evaluated as shown in Figure 3.4C. Series of dilutions of culture medium with virus, remdesivir + virus, or MMT5-14 + virus were incubated with Vero-E6 cells. The virus infected cells with low cell viability in the presence/absence of drug treatment were labeled as positive. The quantification of the titer reduction was also calculated by log(TCID<sub>50</sub>/ml) through Reed-Muench method<sup>22</sup>:

$$\log_{10} TCID50/ml = \log_{10}(Endpoint\ Dilution) + \Delta logs * \log_{10}(dilution\ factor)$$

$$\Delta logs = \frac{\log_{10}(Infection\ ratio\ at\ Endpoint\ Dilution) - 50\%}{\log_{10}(Infection\ ratio\ at\ Endpoint\ Dilution) - \log_{10}(Infection\ ratio\ after\ Endpoint\ Dilution)}$$

the Endpoint Dilution represent the dilution times with infection ratio above 50%.

MMT5-14 showed 4-fold higher virus titer reduction than remdesivir as measured by the significant decrease of Log10 (TCID50).

### 3.4 Conclusion

Despite the recent successful development of antiviral therapy for mild and moderate COVID-19 patients, COVID-19 patients with severe disease still lack effective anti-viral treatment. Although remdesivir is the only FDA approved drug in treating severe disease of COVID-19, its efficacy is limited by premature hydrolysis to NUC, low accumulation in the disease targeted tissues (e.g. lung) and low antiviral potency. In this study, we synthesized new series prodrugs of remdesivir by modifying prodrug moiety of ProTide strategy. The lead compound MMT5-14, in comparison with remdesivir, increased prodrug concentration by 300-fold and 200-fold in the plasma and lung by reducing premature hydrolysis to NUC in hamsters, enhanced accumulation of active metabolite NTP in the lung by 5-fold in hamster. MMT5-14 increased intracellular uptake and activation in lung epithelial cells by 200-fold compared to remdesivir. Further, MMT5-14 showed 4-7-fold antiviral activity than remdesivir in SARS-CoV-2 and different variants. MMT5-14 is a potential antiviral drug to treat severe disease in hospitalized COVID-19 patients.

### 3.5 Experimental Section

**Chemistry.** All commercially available products and solvents were purchased from Sigma-Aldrich, AK Scientific, DC Chemicals and Fisher scientific. Solvents were used as received or dried over molecular sieves (4 Å). All water or air-sensitive reactions were performed under an argon atmosphere with dry solvents and anhydrous conditions. All reactions were monitored by thin-layer chromatography (TLC) performed on aluminum-backed silica plates (0.2 mm, 60 F254). Purification by flash chromatography was

performed on Merck silica gel 60 (230– 400 mesh). Yields refer to chromatographically and spectroscopically ( $^1\text{H}$  and  $^{31}\text{P}$  NMR) homogeneous materials, unless otherwise stated.

NMR spectra were recorded on a Bruker instrument (500 or 300 MHz) and calibrated using a solvent peak as an internal reference. Spectra were processed using MestReNova software. Chemical shifts  $\delta$  are given in ppm and coupling constants ( $J$ ) in Hz. Peak multiplicities are described as follows: s, singlet, t, triplet, and m, multiplet. High-resolution mass spectra were obtained on an AB Sciex X500R QTOF spectrometer. The purity of all compounds subjected to biological tests was determined by analytical HPLC and was found to be  $\geq 95\%$ . The synthesis and characterization of compound **4**<sup>23</sup> and **1b**<sup>24</sup> have been previously described.

General method 1: The alcohol was dissolved in  $\text{CH}_2\text{Cl}_2$  and cooled to  $0^\circ\text{C}$ . A catalytic amount of DMAP (10%) was added and the reaction mixture was stirred for 20 minutes at  $0^\circ\text{C}$ . N-Boc-L-alanine (1eq) and EDC·HCl (1 eq) were added to the reaction mixture at  $0^\circ\text{C}$ . The mixture was stirred for 1 h, warmed up to room temperature, stirred overnight and monitored by TLC. Upon completion, the mixture was diluted with  $\text{CH}_2\text{Cl}_2$ , washed with aqueous  $\text{NaHCO}_3$  followed by brine and dried over  $\text{Na}_2\text{SO}_4$ . The solvent was concentrated under vacuum and the residue was purified by silica gel column chromatography to provide compound **1**. Dodecyl (tert-butoxycarbonyl)-L-alaninate (**1a**). Compound **1a** (1.48 g, yield 86%) was obtained following general method 1.  $^1\text{H}$  NMR (500 MHz, methanol- $d_4$ )  $\delta$  4.04 – 3.92 (m, 3H), 1.58 – 1.46 (m, 2H), 1.34 (s, 9H), 1.31 – 1.18 (m, 21H), 0.80 (t,  $J = 6.9$  Hz, 3H). HRMS (ESI)  $m/z$ : 380.2726 [ $\text{M} + \text{Na}^+$ ]. (9Z,12Z)-octadeca-9,12-dien-1-yl (tert-butoxycarbonyl)-L-alaninate (**1c**). Compound **1c** (5.12 g, yield 95%) was obtained following general method 1.  $^1\text{H}$  NMR (300 MHz, DMSO)  $\delta$  5.32 (q,  $J = 5.9$  Hz, 4H), 4.17 – 3.81 (m, 4H), 2.73 (t,  $J = 5.9$  Hz, 2H), 2.14 – 1.89 (m, 4H), 1.64 – 1.13 (m, 30H), 0.96 – 0.72 (m, 3H). HRMS (ESI)  $m/z$ : 460.3356 [ $\text{M} + \text{Na}^+$ ].

General method 2: Compound **1** was added in one portion to a solution of HCl/dioxane (4ml, 4M) cooled to  $0^\circ\text{C}$  under argon. The ice-bath was removed and the mixture was kept stirred at room temperature for 4h. Upon completion, the reaction mixture was condensed by rotary evaporation under high vacuum. The residue was then



taken into dry Et<sub>2</sub>O and collected by filtration to give the deprotected alanine ester as a hydrochloride salt. The alanine ester hydrochloride (1.1 eq) and the aryloxy dichlorophosphate (1 eq) were dissolved in anhydrous CH<sub>2</sub>Cl<sub>2</sub> and cooled to -78 °C under argon. Et<sub>3</sub>N (5 eq) was added dropwise and the reaction was allowed to slowly warm to room temperature and stirred for 2h. The mixture was then cooled to 0°C and 4-nitrophenol (1 eq) was added followed by the slow addition of Et<sub>3</sub>N (1.1 eq). The resulting mixture was allowed to slowly warm to room temperature and stirred for 3h. Upon completion, the solvent was evaporated under reduced pressure and the resulting residue was dissolved in anhydrous Et<sub>2</sub>O and filtered. The solvent was concentrated under vacuum and the residue was purified by silica gel column chromatography to provide compound **3** as a diastereoisomeric mixture. Dodecyl ((4-nitrophenoxy)(phenoxy)phosphoryl)-L-alaninate (**3a1**). Compound **3a1** (995.4 mg, yield 60%) was obtained as an ~1:1 diastereomeric mixture following general method 2. <sup>1</sup>H NMR (500 MHz, methanol-*d*<sub>4</sub>) δ 8.18 (dd, *J* = 9.1, 1.8 Hz, 2H), 7.40 – 7.31 (m, 2H), 7.31 – 7.25 (m 2H), 7.22 – 7.09 (m, 3H), 4.06 – 3.85 (m, 3H), 1.54 – 1.35 (m, 2H), 1.32 – 1.08 (m, 21H), 0.79 (t, *J* = 6.9 Hz, 3H). <sup>31</sup>P NMR (202 MHz, methanol-*d*<sub>4</sub>) δ -1.52, -1.80. HRMS (ESI) *m/z*: 535.2487 [M + H<sup>+</sup>]. Dodecyl ((naphthalen-1-yloxy)(4-nitrophenoxy)phosphoryl)-L-alaninate (**3a2**). Compound **3a2** (554 mg, yield 56%) was obtained as an ~1:1 diastereomeric mixture following general method 2. <sup>1</sup>H NMR (500 MHz, methanol-*d*<sub>4</sub>) δ 8.19 – 8.12 (m, 2H), 8.06 – 7.96 (m, 1H), 7.82 – 7.76 (m, 1H), 7.63 (dd, *J* = 8.4, 2.9 Hz, 1H), 7.48 – 7.31 (m, 6H), 4.08 – 3.96 (m, 1H), 3.96 – 3.83 (m, 2H), 1.47 – 1.30 (m, 2H), 1.28 – 0.96 (m, 22H), 0.79 (td, *J* = 7.1, 1.5 Hz, 3H). <sup>31</sup>P NMR (202 MHz, methanol-*d*<sub>4</sub>) δ -1.40, -1.43. HRMS (ESI) *m/z*: 585.2642 [M + H<sup>+</sup>]. Benzyl ((naphthalen-1-yloxy)(4-nitrophenoxy)phosphoryl)-L-alaninate (**3b**). Compound **3b** (438 mg, yield 34%) was obtained as an ~1:1 diastereomeric mixture following general method 2. <sup>1</sup>H NMR (500 MHz, methanol-*d*<sub>4</sub>) δ 8.07 (dq, *J* = 8.9, 3.4 Hz, 2H), 8.02 – 7.95 (m, 1H), 7.84 – 7.72 (m, 1H), 7.62 (d, *J* = 8.2 Hz, 1H), 7.45 – 7.35 (m, 3H), 7.35 – 7.22 (m, 3H), 7.21 – 7.11 (m, 5H), 5.03 – 4.86 (m, 2H), 4.16 – 4.00 (m, 1H), 1.23 (dt, *J* = 7.2, 1.4 Hz, 3H). <sup>31</sup>P NMR (202 MHz, methanol-*d*<sub>4</sub>) δ -1.33, -1.50. HRMS (ESI) *m/z*: 507.1236 [M + H<sup>+</sup>]. (9*Z*,12*Z*)-octadeca-9,12-dien-1-yl ((4-nitrophenoxy)(phenoxy)phosphoryl)-L-alaninate (**3c1**). Compound **3c1** (916 mg, yield

61%) was obtained as an ~1:1 diastereomeric mixture following general method 2. <sup>1</sup>H NMR (500 MHz, methanol-*d*<sub>4</sub>) δ 8.17 – 8.11 (m, 2H), 7.39 – 7.30 (m, 2H), 7.30 – 7.22 (m, 2H), 7.20 – 7.06 (m, 3H), 5.28 – 5.15 (m, 4H), 4.71 (s, 1H), 4.00 – 3.89 (m, 3H), 2.65 (t, *J* = 6.2 Hz, 2H), 1.97 – 1.86 (m, 4H), 1.49 – 1.39 (m, 2H), 1.29 – 1.08 (m, 19H), 0.77 (t, *J* = 6.9 Hz, 3H). <sup>31</sup>P NMR (202 MHz, methanol-*d*<sub>4</sub>) δ -1.62, -1.87. HRMS (ESI) *m/z*: 615.3113 [M + H<sup>+</sup>]. (9*Z*,12*Z*)-octadeca-9,12-dien-1-yl ((naphthalen-1-yloxy)(4-nitrophenoxy)phosphoryl)-L-alaninate (**3c2**). Compound **3c2** (673 mg, yield 42%) was obtained as an ~1:1 diastereomeric mixture following general method 2. <sup>1</sup>H NMR (500 MHz, methanol-*d*<sub>4</sub>) δ 8.12 (d, *J* = 9.2 Hz, 2H), 8.05 – 7.96 (m, 1H), 7.80 – 7.71 (m, 1H), 7.64 – 7.56 (m, 1H), 7.49 – 7.27 (m, 6H), 5.28 – 5.14 (m, 4H), 4.10 – 3.96 (m, 1H), 3.94 – 3.81 (m, 2H), 2.64 (t, *J* = 6.3 Hz, 2H), 1.96 – 1.86 (m, 4H), 1.45 – 1.30 (m, 2H), 1.28 – 0.98 (m, 19H), 0.77 (t, *J* = 6.9 Hz, 3H). <sup>31</sup>P NMR (202 MHz, methanol-*d*<sub>4</sub>) δ -1.44, -1.49. HRMS (ESI) *m/z*: 665.3284 [M + H<sup>+</sup>].

General method 3: To a solution of compound **3** (1.2 eq) in CH<sub>3</sub>CN, was added compound **4** (1 eq), and MgCl<sub>2</sub> (1 eq) at room temperature. The solution was heated to 50 °C for 15 min, and DIPEA (2.5 eq) was added. After 1 hour, the reaction mixture was allowed to cool to room temperature, and then diluted with EtOAc. The organic layer was washed with 5% aqueous citric acid, saturated aqueous NH<sub>4</sub>Cl, 5% aqueous K<sub>2</sub>CO<sub>3</sub>, and brine. The organic layer was dried over anhydrous Na<sub>2</sub>SO<sub>4</sub> and reduced to dryness to give compound **5**, which was purified by column chromatography on silica gel. Dodecyl (((((3*aR*,4*R*,6*R*,6*aR*)-6-(4-aminopyrrolo[2,1-*f*][1,2,4]triazin-7-yl)-6-cyano-2,2-dimethyltetrahydrofuro[3,4-*d*][1,3]dioxol-4-yl)methoxy)(phenoxy)phosphoryl)-L-alaninate (**5a1**). Compound **5a1** (748.6 mg, yield 74%) was obtained as an ~1:1 diastereomeric mixture following general method 3. <sup>1</sup>H NMR (500 MHz, methanol-*d*<sub>4</sub>) δ 7.76 (s, 1H), 7.20 – 7.12 (m, 2H), 7.07 – 7.01 (m, 2H), 6.97 (dt, *J* = 8.5, 1.3 Hz, 1H), 6.86 – 6.72 (m, 2H), 5.24 (d, *J* = 6.7 Hz, 1H), 4.90 – 4.81 (m, 1H), 4.54 – 4.43 (m, 1H), 4.27 – 4.12 (m, 2H), 4.00 – 3.85 (m, 2H), 3.77 – 3.64 (m, 1H), 1.60 (d, *J* = 3.9 Hz, 3H), 1.52 – 1.41 (m, 2H), 1.29 (d, *J* = 13.1 Hz, 3H), 1.17 (m, 23H), 0.79 (t, *J* = 6.9 Hz, 3H). <sup>31</sup>P NMR (202 MHz, methanol-*d*<sub>4</sub>) δ 3.51, 3.20. HRMS (ESI) *m/z*: 727.3462 [M + H<sup>+</sup>]. Dodecyl (((((3*aR*,4*R*,6*R*,6*aR*)-6-(4-aminopyrrolo[2,1-*f*][1,2,4]triazin-7-yl)-6-cyano-2,2-dimethyltetrahydrofuro[3,4-*d*][1,3]dioxol-4-yl)methoxy)(naphthalen-1-

xyloxy)phosphoryl)-L-alaninate (**5a2**). Compound **5a2** (347 mg, yield 70%) was obtained as an ~1:1 diastereomeric mixture following general method 3. <sup>1</sup>H NMR (500 MHz, methanol-*d*<sub>4</sub>) δ 8.03 – 7.85 (m, 1H), 7.79 – 7.68 (m, 2H), 7.54 (dd, *J* = 32.4, 8.2 Hz, 1H), 7.41 – 7.13 (m, 4H), 6.81 – 6.67 (m, 2H), 4.92 (d, *J* = 6.6 Hz, 1H), 4.80 (dd, *J* = 6.6, 3.3 Hz, 1H), 4.47 (dt, *J* = 5.7, 3.9 Hz, 1H), 4.30 – 4.13 (m, 2H), 4.00 – 3.75 (m, 3H), 1.57 (d, *J* = 12.3 Hz, 3H), 1.50 – 1.35 (m, 2H), 1.27 – 0.99 (m, 26H), 0.78 (t, *J* = 7.1 Hz, 3H). <sup>31</sup>P NMR (202 MHz, methanol-*d*<sub>4</sub>) δ 3.87, 3.64. HRMS (ESI) *m/z*: 777.3634 [M + H<sup>+</sup>]. Benzyl (((3*aR*,4*R*,6*R*,6*aR*)-6-(4-aminopyrrolo[2,1-*f*][1,2,4]triazin-7-yl)-6-cyano-2,2-dimethyltetrahydrofuro[3,4-*d*][1,3]dioxol-4-yl)methoxy)(naphthalen-1-xyloxy)phosphoryl)-L-alaninate (**5b**). Compound **5b** (260 mg, yield 67%) was obtained as an ~1:1 diastereomeric mixture following general method 3. <sup>1</sup>H NMR (500 MHz, methanol-*d*<sub>4</sub>) δ 8.10 – 7.90 (m, 1H), 7.90 – 7.73 (m, 2H), 7.71 – 7.54 (m, 1H), 7.50 – 7.31 (m, 3H), 7.31 – 7.20 (m, 6H), 6.91 – 6.72 (m, 2H), 5.13 – 4.97 (m, 3H), 4.88 – 4.85 (m, 1H), 4.54 – 4.48 (m, 1H), 4.35 – 4.19 (m, 2H), 4.04 – 3.94 (m, 1H), 1.66 (d, *J* = 11.5 Hz, 3H), 1.34 – 1.20 (m, 6H); <sup>31</sup>P NMR (202 MHz, methanol-*d*<sub>4</sub>) δ 3.91, 3.53. HRMS (ESI) *m/z*: 699.2217 [M + H<sup>+</sup>]. (9*Z*,12*Z*)-octadeca-9,12-dien-1-yl (((3*aR*,4*R*,6*R*,6*aR*)-6-(4-aminopyrrolo[2,1-*f*][1,2,4]triazin-7-yl)-6-cyano-2,2-dimethyltetrahydrofuro[3,4-*d*][1,3]dioxol-4-yl)methoxy)(phenoxy)phosphoryl)-L-alaninate (**5c1**). Compound **5c1** (404 mg, yield 52%) was obtained as an ~1:1 diastereomeric mixture following general method 3. <sup>1</sup>H NMR (500 MHz, methanol-*d*<sub>4</sub>) δ 7.76 (s, 1H), 7.25 – 7.10 (m, 2H), 7.07 – 7.01 (m, 2H), 6.97 (dq, *J* = 7.7, 1.2 Hz, 1H), 6.84 – 6.72 (m, 2H), 5.31 – 5.14 (m, 4H), 4.92 – 4.81 (m, 1H), 4.56 – 4.38 (m, 1H), 4.28 – 4.10 (m, 3H), 4.03 – 3.82 (m, 2H), 3.79 – 3.61 (m, 1H), 2.67 (t, *J* = 6.5 Hz, 1H), 2.01 – 1.86 (m, 3H), 1.60 (d, *J* = 3.9 Hz, 4H), 1.43 – 1.37 (m, 3H), 1.35 – 1.09 (m, 26H), 0.80 (t, *J* = 6.9 Hz, 3H). <sup>31</sup>P NMR (202 MHz, methanol-*d*<sub>4</sub>) δ 3.51, 3.20. HRMS (ESI) *m/z*: 807.4087 [M + H<sup>+</sup>]. (9*Z*,12*Z*)-octadeca-9,12-dien-1-yl (((3*aR*,4*R*,6*R*,6*aR*)-6-(4-aminopyrrolo[2,1-*f*][1,2,4]triazin-7-yl)-6-cyano-2,2-dimethyltetrahydrofuro[3,4-*d*][1,3]dioxol-4-yl)methoxy)(naphthalen-1-xyloxy)phosphoryl)-L-alaninate (**5c2**). Compound **5c2** (436 mg, yield 68%) was obtained as an ~1:1 diastereomeric mixture following general method 3. <sup>1</sup>H NMR (500 MHz, methanol-*d*<sub>4</sub>) δ 8.03 – 7.84 (m, 1H), 7.77 – 7.69 (m, 2H), 7.60 – 7.48 (m, 1H), 7.42 – 7.21 (m, 3H), 7.17 (t, *J* = 7.9 Hz, 1H), 6.82 – 6.67 (m, 2H), 5.32 – 5.13 (m, 4H), 4.93 (d, *J* =

6.6 Hz, 1H), 4.84 – 4.77 (m, 1H), 4.47 (qd,  $J = 4.1, 1.7$  Hz, 1H), 4.31 – 4.11 (m, 2H), 4.01 – 3.78 (m, 3H), 2.73 – 2.58 (m, 2H), 2.00 – 1.83 (m, 4H), 1.57 (d,  $J = 11.9$  Hz, 3H), 1.48 – 1.34 (m, 2H), 1.32 – 1.00 (m, 23H), 0.78 (t,  $J = 7.0$  Hz, 3H).  $^{31}\text{P}$  NMR (202 MHz, methanol- $d_4$ )  $\delta$  3.85, 3.63. HRMS (ESI)  $m/z$ : 857.4227 [ $\text{M} + \text{H}^+$ ].

General method 4: To a stirred solution of intermediate **5** (1 eq) in THF was added 37% aqueous HCl slowly at 0 °C. The reaction mixture was allowed to warm to room temperature. After 6 h, the reaction mixture was diluted with water and adjusted to pH=8 by the addition of saturated aqueous  $\text{NaHCO}_3$ . The resulting mixture was extracted with EtOAc, and the organic layer was then washed with brine, dried over anhydrous  $\text{Na}_2\text{SO}_4$ , and concentrated under reduced pressure. The crude product obtained after evaporation was purified by column chromatography on silica gel to give the remdesivir analog. Dodecyl (((((2R,3S,4R,5R)-5-(4-aminopyrrolo[2,1-f][1,2,4]triazin-7-yl)-5-cyano-3,4-dihydroxytetrahydrofuran-2-yl)methoxy)(phenoxy)phosphoryl)-L-alaninate (**MMT4-70**). Compound **MMT4-70** (337.3 mg, yield 60%) was obtained as a diastereomeric mixture (45%, 55%) following general method 4.  $^1\text{H}$  NMR (500 MHz, methanol- $d_4$ )  $\delta$  7.85 (d,  $J = 7.5$  Hz, 1H), 7.29 (dt,  $J = 9.2, 7.2$  Hz, 2H), 7.22 – 7.07 (m, 3H), 6.97 – 6.73 (m, 2H), 4.79 (d,  $J = 5.4$  Hz, 1H), 4.45 – 4.33 (m, 2H), 4.33 – 4.24 (m, 1H), 4.18 (dt,  $J = 17.3, 5.5$  Hz, 1H), 4.10 – 3.96 (m, 3H), 1.64 – 1.48 (m, 2H), 1.26 (tdd,  $J = 13.7, 5.7, 2.2$  Hz, 25H), 0.89 (t,  $J = 6.8$  Hz, 3H);  $^{31}\text{P}$  NMR (202 MHz, methanol- $d_4$ )  $\delta$  3.53 (s), 3.49 (s); HRMS (ESI)  $m/z$ : 687.3160 [ $\text{M} + \text{H}^+$ ]. Dodecyl (((((2R,3S,4R,5R)-5-(4-aminopyrrolo[2,1-f][1,2,4]triazin-7-yl)-5-cyano-3,4-dihydroxytetrahydrofuran-2-yl)methoxy)(naphthalen-1-yloxy)phosphoryl)-L-alaninate (**MMT4-98**). Compound **MMT4-98** (75 mg, yield 26%) was obtained as a diastereomeric mixture (47%, 53%) following general method 4.  $^1\text{H}$  NMR (500 MHz, methanol- $d_4$ )  $\delta$  8.16 – 8.02 (m, 1H), 7.87 – 7.79 (m, 2H), 7.66 (t,  $J = 8.0$  Hz, 1H), 7.53 – 7.40 (m, 3H), 7.34 (dt,  $J = 9.5, 7.9$  Hz, 1H), 6.88 – 6.76 (m, 2H), 4.69 (t,  $J = 5.6$  Hz, 1H), 4.46 (dddd,  $J = 11.4, 8.9, 6.0, 2.8$  Hz, 1H), 4.41 – 4.30 (m, 2H), 4.19 (t,  $J = 5.5$  Hz, 1H), 4.04 – 3.90 (m, 3H), 1.58 – 1.43 (m, 2H), 1.37 – 1.09 (m, 25H), 0.89 (t,  $J = 6.8$ , 3H);  $^{31}\text{P}$  NMR (202 MHz, methanol- $d_4$ )  $\delta$  3.92 (s), 3.87 (s); HRMS (ESI)  $m/z$ : 737.3362 [ $\text{M} + \text{H}^+$ ]. Benzyl (((((2R,3S,4R,5R)-5-(4-aminopyrrolo[2,1-f][1,2,4]triazin-7-yl)-5-cyano-3,4-dihydroxytetrahydrofuran-2-yl)methoxy)(naphthalen-1-yloxy)phosphoryl)-L-alaninate (**MMT5-1**). Compound

**MMT5-1** (62.6 mg, yield 30%) was obtained as a diastereomeric mixture (42%, 58%) following general method 4.  $^1\text{H}$  NMR (500 MHz, methanol- $d_4$ )  $\delta$  8.12 – 8.01 (m, 1H), 7.88 – 7.78 (m, 2H), 7.65 (dd,  $J = 10.7, 8.2$  Hz, 1H), 7.52 – 7.36 (m, 3H), 7.35 – 7.20 (m, 6H), 6.91 – 6.71 (m, 2H), 5.09 – 4.95 (m, 2H), 4.67 (dd,  $J = 9.2, 5.5$  Hz, 1H), 4.47 – 4.25 (m, 3H), 4.20 – 4.13 (m, 1H), 4.02 – 3.89 (m, 1H), 1.31 – 1.24 (m, 3H);  $^{31}\text{P}$  NMR (202 MHz, methanol- $d_4$ )  $\delta$  3.95 (s), 3.82 (s); HRMS (ESI)  $m/z$ : 659.1912 [ $\text{M} + \text{H}^+$ ]. (9Z,12Z)-octadeca-9,12-dien-1-yl (((((2R,3S,4R,5R)-5-(4-aminopyrrolo[2,1-f][1,2,4]triazin-7-yl)-5-cyano-3,4-dihydroxytetrahydrofuran-2-yl)methoxy)(phenoxy)phosphoryl)-L-alaninate (**MMT5-14**). Compound **MMT5-14** (169.6 mg, yield 51%) was obtained as a diastereomeric mixture (48%, 52%) following general method 4.  $^1\text{H}$  NMR (500 MHz, methanol- $d_4$ )  $\delta$  7.85 (s, 1H), 7.29 (dt,  $J = 9.1, 7.4$  Hz, 2H), 7.21 – 7.10 (m, 3H), 6.93 – 6.85 (m, 2H), 5.43 – 5.23 (m, 4H), 4.79 (d,  $J = 5.4$  Hz, 1H), 4.47 – 4.33 (m, 2H), 4.33 – 4.23 (m, 1H), 4.19 (dt,  $J = 17.5, 5.5$  Hz, 1H), 4.10 – 3.94 (m, 2H), 3.92 – 3.76 (m, 1H), 2.76 (t,  $J = 6.3$  Hz, 2H), 2.11 – 1.98 (m, 4H), 1.60 – 1.52 (m, 2H), 1.41 – 1.19 (m, 23H), 0.89 (t,  $J = 6.8$  Hz, 3H);  $^{31}\text{P}$  NMR (202 MHz, methanol- $d_4$ )  $\delta$  3.52 (s), 3.50 (s); HRMS (ESI)  $m/z$ : 767.3773 [ $\text{M} + \text{H}^+$ ]. (9Z,12Z)-octadeca-9,12-dien-1-yl (((((2R,3S,4R,5R)-5-(4-aminopyrrolo[2,1-f][1,2,4]triazin-7-yl)-5-cyano-3,4-dihydroxytetrahydrofuran-2-yl)methoxy)(naphthalen-1-yloxy)phosphoryl)-L-alaninate (**MMT5-15**). Compound **MMT5-15** (171.9 mg, yield 60%) was obtained as a diastereomeric mixture (50%, 50%) following general method 4.  $^1\text{H}$  NMR (500 MHz, methanol- $d_4$ )  $\delta$  8.09 (ddd,  $J = 24.8, 7.6, 2.2$  Hz, 1H), 7.88 – 7.78 (m, 2H), 7.66 (t,  $J = 7.9$  Hz, 1H), 7.52 – 7.46 (m, 2H), 7.46 – 7.40 (m, 1H), 7.38 – 7.28 (m, 1H), 6.87 – 6.77 (m, 2H), 5.43 – 5.18 (m, 4H), 4.69 (t,  $J = 5.5$  Hz, 1H), 4.49 – 4.41 (m, 1H), 4.42 – 4.37 (m, 1H), 4.34 (td,  $J = 10.6, 10.0, 4.4$  Hz, 1H), 4.19 (t,  $J = 5.5$  Hz, 1H), 4.03 – 3.91 (m, 3H), 2.75 (t,  $J = 6.3$  Hz, 2H), 2.09 – 1.91 (m, 4H), 1.55 – 1.42 (m, 2H), 1.39 – 1.07 (m, 23H), 0.89 (t,  $J = 6.8$  Hz, 3H);  $^{31}\text{P}$  NMR (202 MHz, methanol- $d_4$ )  $\delta$  3.93 (s), 3.87(s); HRMS (ESI)  $m/z$ : 817.3939 [ $\text{M} + \text{H}^+$ ].

**Cells.** Calu-3 (HTB-55), HUVEC (Human Primary Umbilical Vein Endothelial Cells, PCS-100-010), and Vero E6 cells were purchased from American Type Culture Collection. Calu-3 cells were cultured in ATCC-formulated Eagle's Minimum Essential Medium (EMEM) supplemented with 10% fetal bovine serum. HUVEC cells were

cultured in Vascular Cell Basal Medium supplemented with Endothelial Cell Growth Kit-BBE (ATCC PCS-100-040, including Bovine Brain Extract (BBE), rh EGF, L-glutamine, Heparin sulfate, Hydrocortisone hemisuccinate, Fetal Bovine Serum and Ascorbic acid). Vero E6 cells were cultured in EMEM supplemented with 5% FBS.

**Virus:** SARS-CoV-2 UTHSC passage 2, (SARS-Related Coronavirus 2 Isolate USA-WA1/2020)

**Animal.** Catheterized LVG Golden Syrian Hamster (female, 70-80 g, Jugular vein catheters) are purchased from Charles river and used for PK study. All animal procedures used in this study were approved by the University Committee on Use and Care Animals at the University of Michigan.

**PK study.** Catheterized female hamsters were used for PK study. 10mg/Kg remdesivir (15% cyclodextrin, pH 3-3.5) and MMT5-14 (cyclodextrin or albumin formulation) was injected intravenously with the concentration set as 2mg/ml. At scheduled timepoint (0.5h, 1h, 4h, 7h and 24h), 2 hamsters from each group were sacrificed and tissues including blood, blood vessel, bone marrow, brain, colon, fat, fatpad, heart, intestine, kidney, liver, lung, lymph node, mouth membrane, muscle, nose, pancreas, plasma, skin, spleen, stomach, trachea and uterus were collected and stored at -80 °C refrigerator. Before analyzing, samples were mixed with 5 fold of 70% methanol solution (internal standard included) and homogenized within Precellys Lysing Kit (7700 rpm, 20s \* 4 per cycle , 3 cycles in total, 4°C). Supernatant was then collected through centrifugation for further concentration test. Remdesivir, MMT5-14, ALA, and NUC were analyzed on an X500R QTOF System (AB Sciex, USA). Chromatographic separation was obtained on a 50 × 2.1 mm Agilent 3.5 µm C18 column using constant flow rate of 0.6 mL/min. The gradient mobile phase consisted of 0.1% formic acid in water (mobile phase A) and 0.1% formic acid acetonitrile (mobile phase B), running from 5% B to 95% B within 3 min and then maintaining 95% B for 1 min. The eluent was introduced into quadrupole time-of-flight mass spectrometry by electrospray ionization (ESI) operated in positive modes. For NTP analysis, supernatant solution was further concentrated to 20 fold through freeze

drying and its LC-MS/MS was performed by ion-pairing chromatography using LC 20AD UFLC (Shimadzu, Japan) couple with an API 5500 (AB Sciex, USA). The separation was achieved on a 50 × 2.1 mm Agilent 3.5 μm C18 column. The mobile phase consisted of 3 mM ammonium formate with 10 mM dimethylhexylamine in water (mobile phase A), and 0.1% formic Acid in ACN (mobile phase B). A multi-stage linear gradient initiated with 2% B for 1 min, increased to 95% B in 2 min and maintained with 95% B for 1 min at a flow rate of 0.4 mL/min. Detection was performed on negative ion mode and multiple reaction monitoring modes. All the analytes were quantified using 10-point standard curves ranging from 5 to 5000 ng/mL.

**Cell uptake.** 1-5 × 10<sup>5</sup> of Calu-3 and HUVEC cells were cultured per well in 12-well plate for 12 h before incubating with drugs. 10 μM of remdesivir or MMT5-14 were then added into each well and incubated at 37 °C for 2, 6 and 12 hours (n = 3). At each scheduled time point, medium was collected together with detached cells in Trypsin-EDTA solution (200 ul per well). Centrifugation (600 g, 5 min, 4 °C) was used to remove the medium and the cell pellets were then washed with 1 ml ice-cold PBS for three times. 200 ul of ice-cold 70% methanol was added last and stored at -20 °C overnight to extract drug molecules. After centrifugation at 15, 000 g for 15 mins, the supernatants were collected for LC-MS test.

**In vitro antiviral test against SARS CoV-2.** High throughput screening (HTS) was used to provide the percent protection of cytopathic effect of SARS CoV-2. Briefly, Vero E6 cells were plated into 384-well plate with seeding density as 5000-6000 per well. The next day, different concentration of compounds were added and the highest DMSO was kept below 0.5%. The cells were transported to the BSL3 and half of them were infected with SARS-CoV-2 virus with multiplicity of infection (MOI) as 0.1. After 2 days incubation at 37 °C, 5% CO<sub>2</sub>, 25 ul of Promega CellTiter-Glo® (Promega, Madison, WI) was added to each well and the luminescence was then measured using a PerkinElmer Envision™ plate reader (PerkinElmer, Wellesley, MA). Cells only were treated as the positive control and virus-infected cells as negative control. Titer reduction assay was used to show the different capacity of remdesivir and MMT5-14 in the reduction of the

virus titer. Briefly, Vero E6 cells were grown in 12-well plates overnight and then infected one hour with virus at a MOI of 0.1 diluted in EMEM. Cells were then washed twice with PBS and incubated with media containing 5  $\mu$ M of remdesivir or MMT5-14. After two days, supernatant was collected and the number of infectious virus particles in it was quantified by Median Tissue Culture Infectious Dose (TCID<sub>50</sub>) assay. Vero E6 cells were used in this assay and incubated with serial dilution of the infectious supernatant (n=4) and the cytopathic effect was monitored by Promega CellTiter-Glo kit.

### **3.6 Figures and Tables**



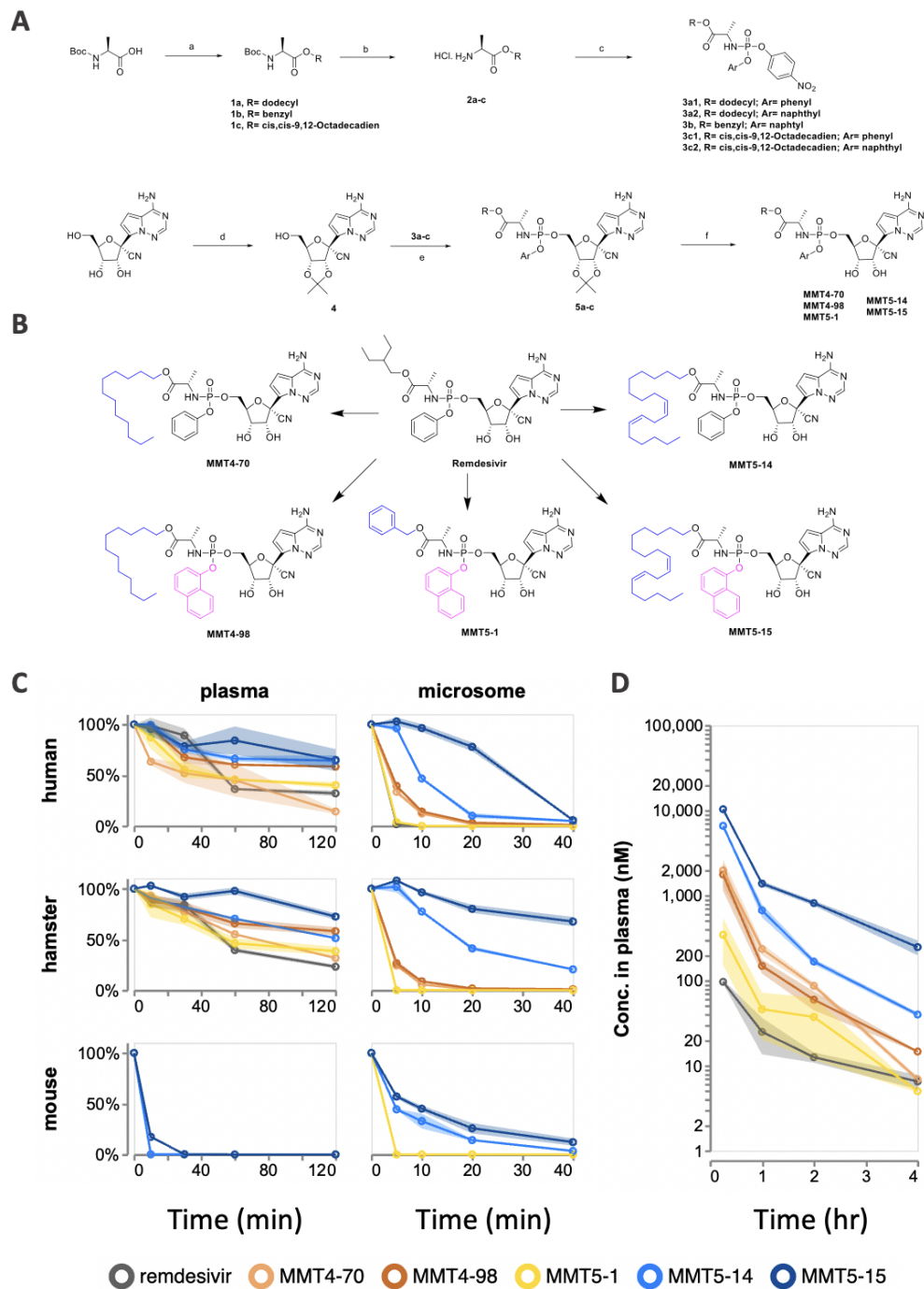


Figure 3.1. Synthesis of remdesivir analogs and their improved in-vitro and in-vivo stability. (A) Modification of prodrug moiety of remdesivir using ProTide strategy. Reaction conditions: (a) appropriate alcohol, EDC.HCl, DMAP, CH<sub>2</sub>Cl<sub>2</sub>, rt, overnight, and 95%; (b) 4 M HCl in dioxane, rt, 4h; (c) OP(OAr)Cl<sub>2</sub>, ET<sub>3</sub>N, CH<sub>2</sub>Cl<sub>2</sub>, -78°C, 2h, then 4-nitrophenol, ET<sub>3</sub>N, 0°C, 2h, and 60%; (d) 2,2-dimethoxypropane, H<sub>2</sub>SO<sub>4</sub>, acetone, rt, 1.5h, and 96%; (e) MgCl<sub>2</sub>, DIPEA, MeCN, 2h, 50°C, and 74%; (f) 37% HCl, THF, rt, 5h, and 60%. (B) Structure of five new analogs in comparison with remdesivir. (C) In-vitro plasma and microsome stability for remdesivir and its analogs in human, hamster and mouse species. Data are represented as mean ± SD (shaded area). (D) In-vivo plasma concentration-time profile in hamster of five new analogs in comparison with remdesivir (10 mg/kg, iv).

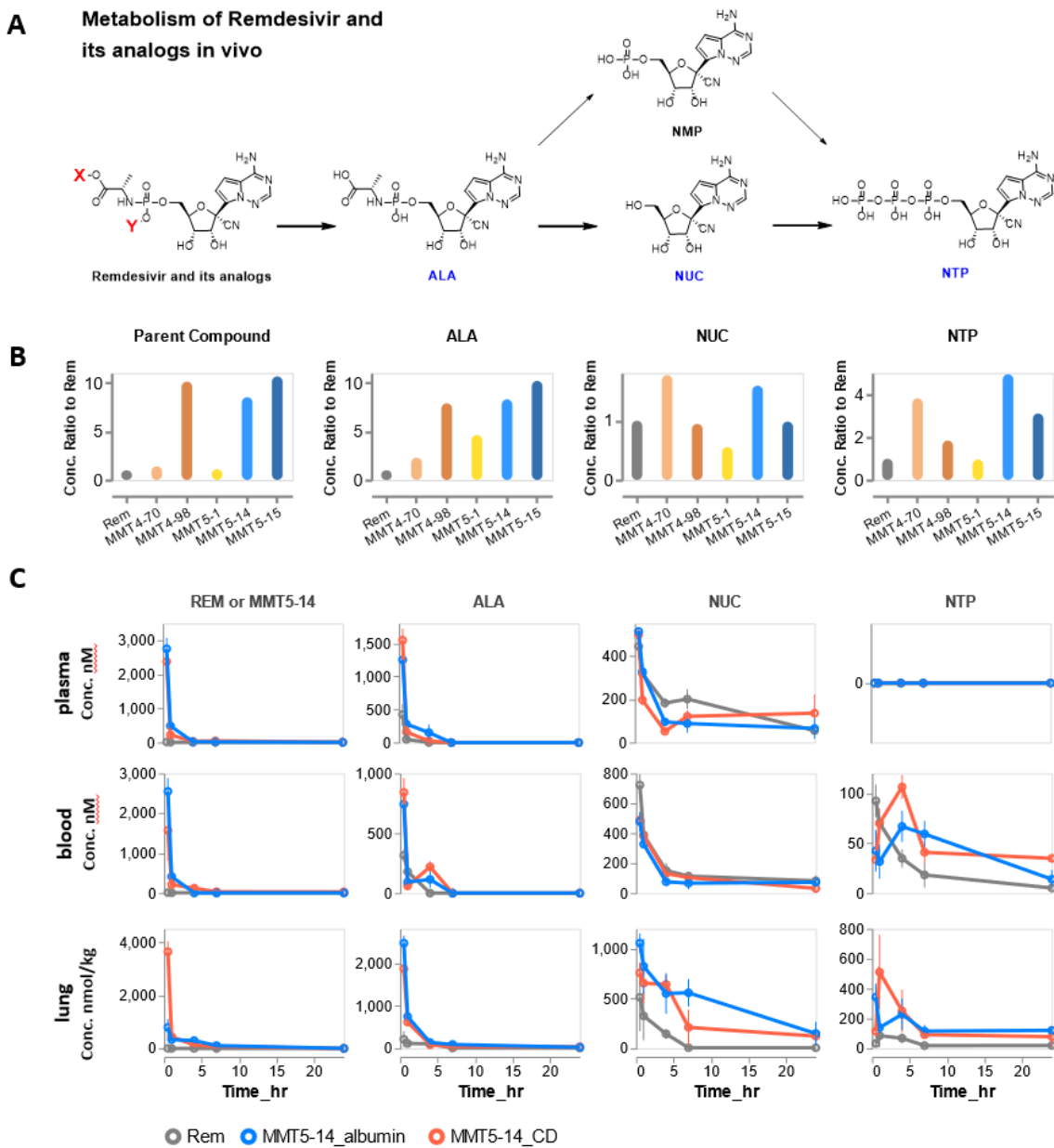


Figure 3.2. MMT5-14 and MMT5-15 achieved higher drug concentration and active metabolite, NTP in blood and lung. (A) Activation of prodrug remdesivir and formation of its active metabolite NTP in vivo. (B) Ratio of compound concentration in lung between new analogs and remdesivir (10 mg/kg, iv, 4 h). (C) Concentration-time profile of MMT5-14 (two formulations) and its metabolites in plasma, blood and lung in comparison with remdesivir after 10 mg/kg IV dose in hamsters.

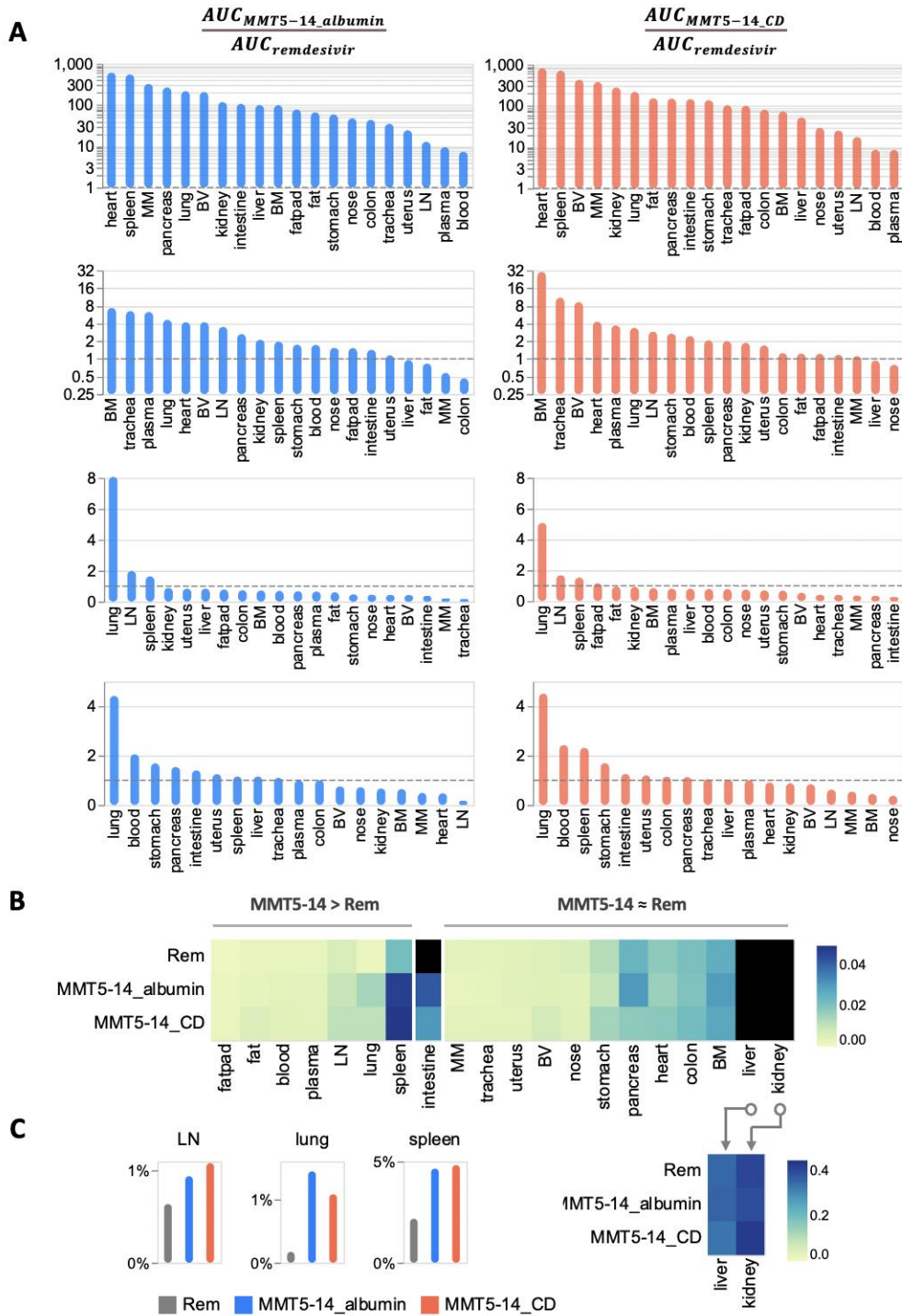


Figure 3.3. MMT5-14 not only increased tissue exposure but also increased the tissue selectivity of both prodrug and active metabolite NTP in the lung, spleen and blood. (A) Drug exposure (AUC) ratios of prodrug, ALA, NUC, and NTP between MMT5-14 vs. remdesivir after IV dose (10 mg/kg, iv, in hamsters). (B) Comparison of tissues selectivity in all tissues between MMT5-14 and remdesivir. (C) MMT5-14 increased tissue selectivity in in the lung, spleen and lymph nodes .

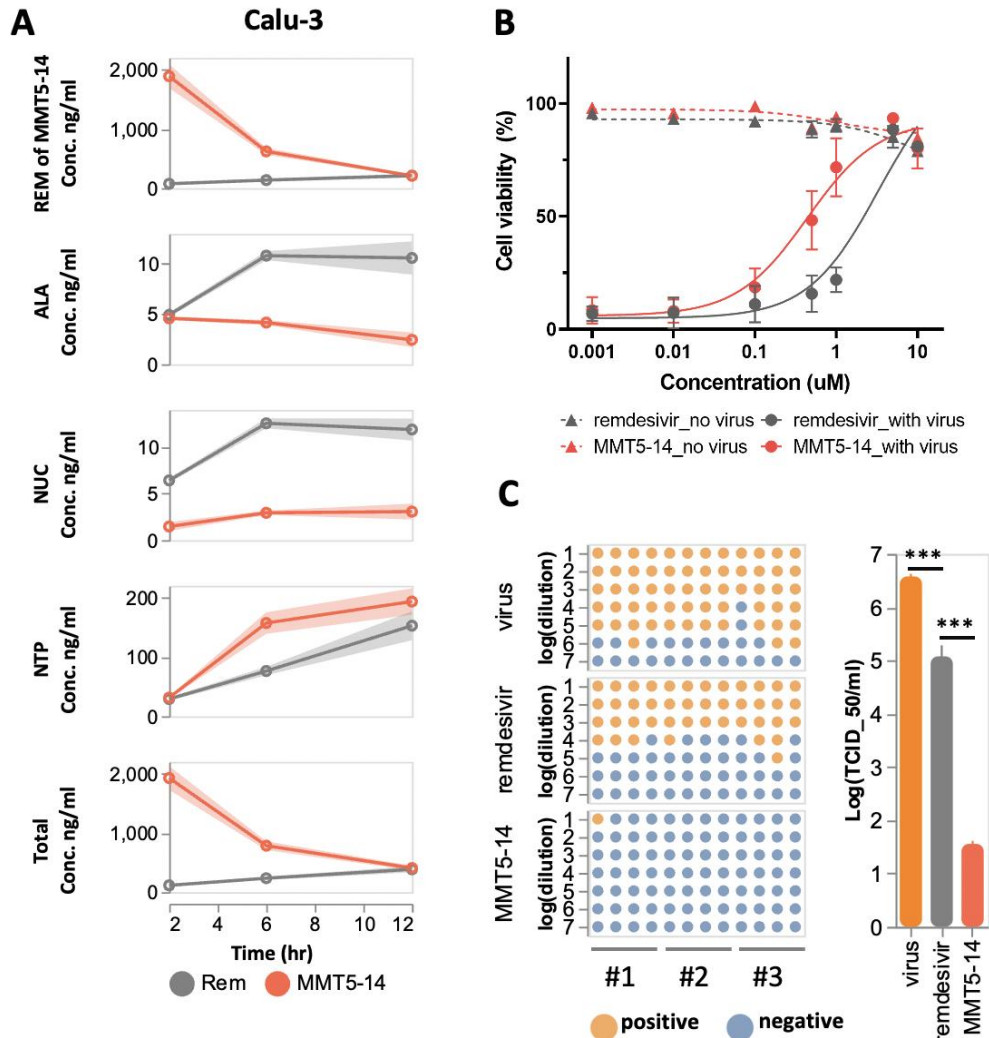
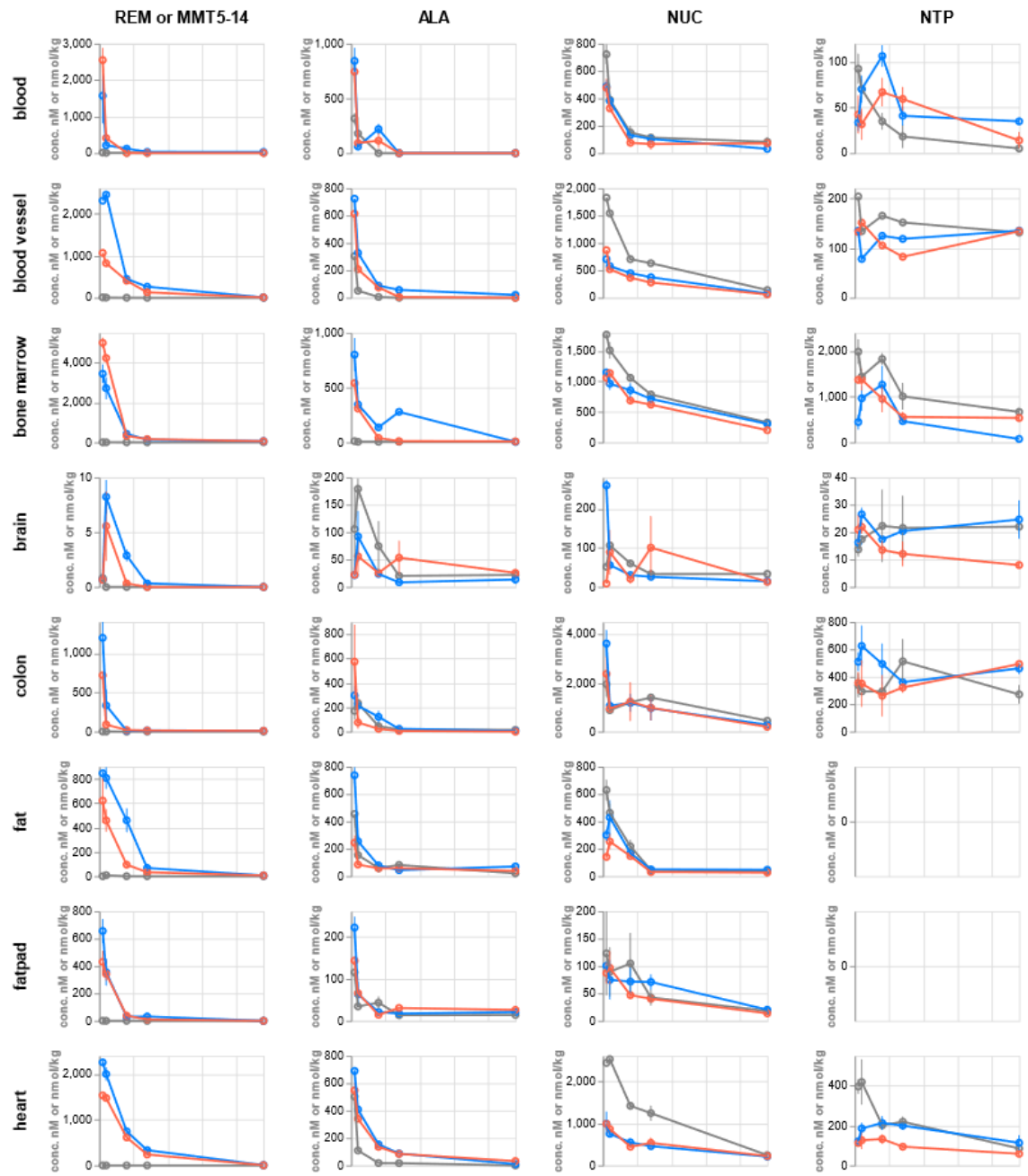
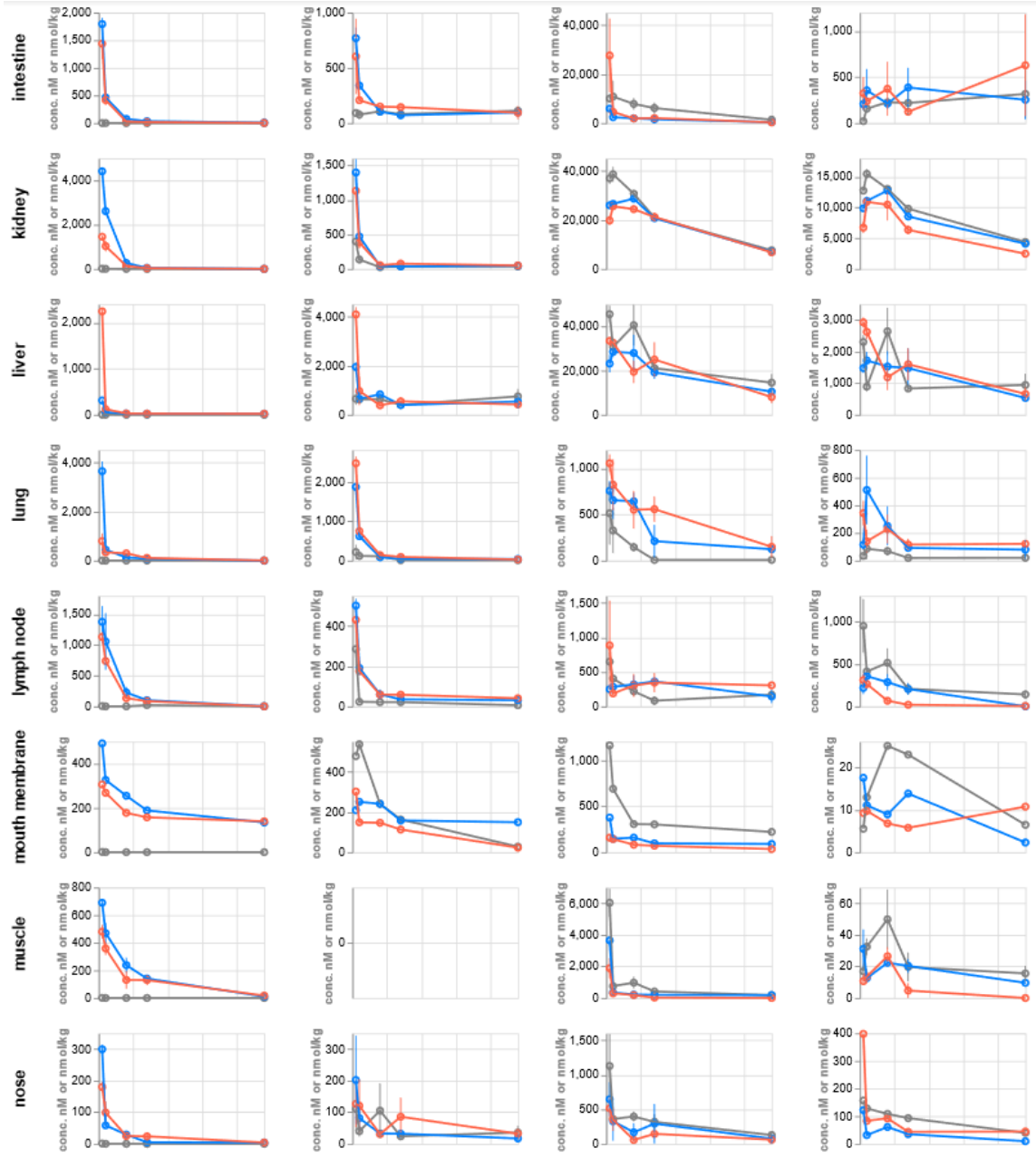


Figure 3.4. MMT5-14 increased epithelial cells uptake and in-vitro antiviral activity. (A) Intracellular uptake and activation of MMT5-14 and remdesivir or (10 uM) in Calu-3. Data are represented by mean  $\pm$  SD (shaded area). (B) Cell viability protection by MMT5-14 and remdesivir from SARS-Cov-2 virus infection. (c) Calculated EC50 of MMT5-14 and remdesivir against SARS-Cov-2 virus and four variants (C) Virus titer reduction assay by MMT5-14 and remdesivir or. Data are represented by mean  $\pm$  SD\*\*\* $p < 0.001$ , by 2-tailed, unpaired t-test.





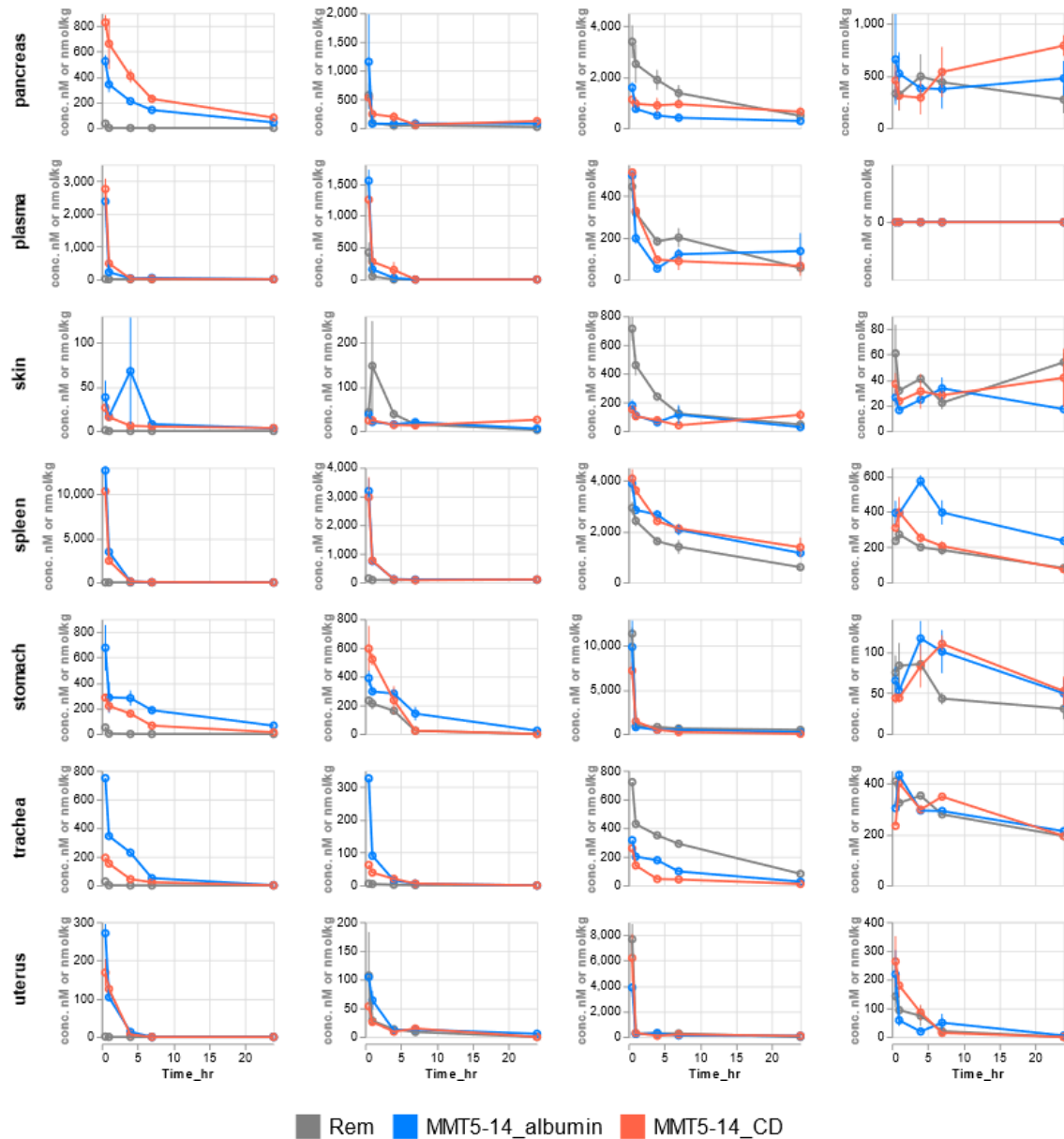


Figure 3.S1. Concentration-time profile in collected tissues from hamsters (n=2) after administration of remdesivir, MMT5-14\_albumin or MMR5-14\_CD. Data are represented as mean (min, max)

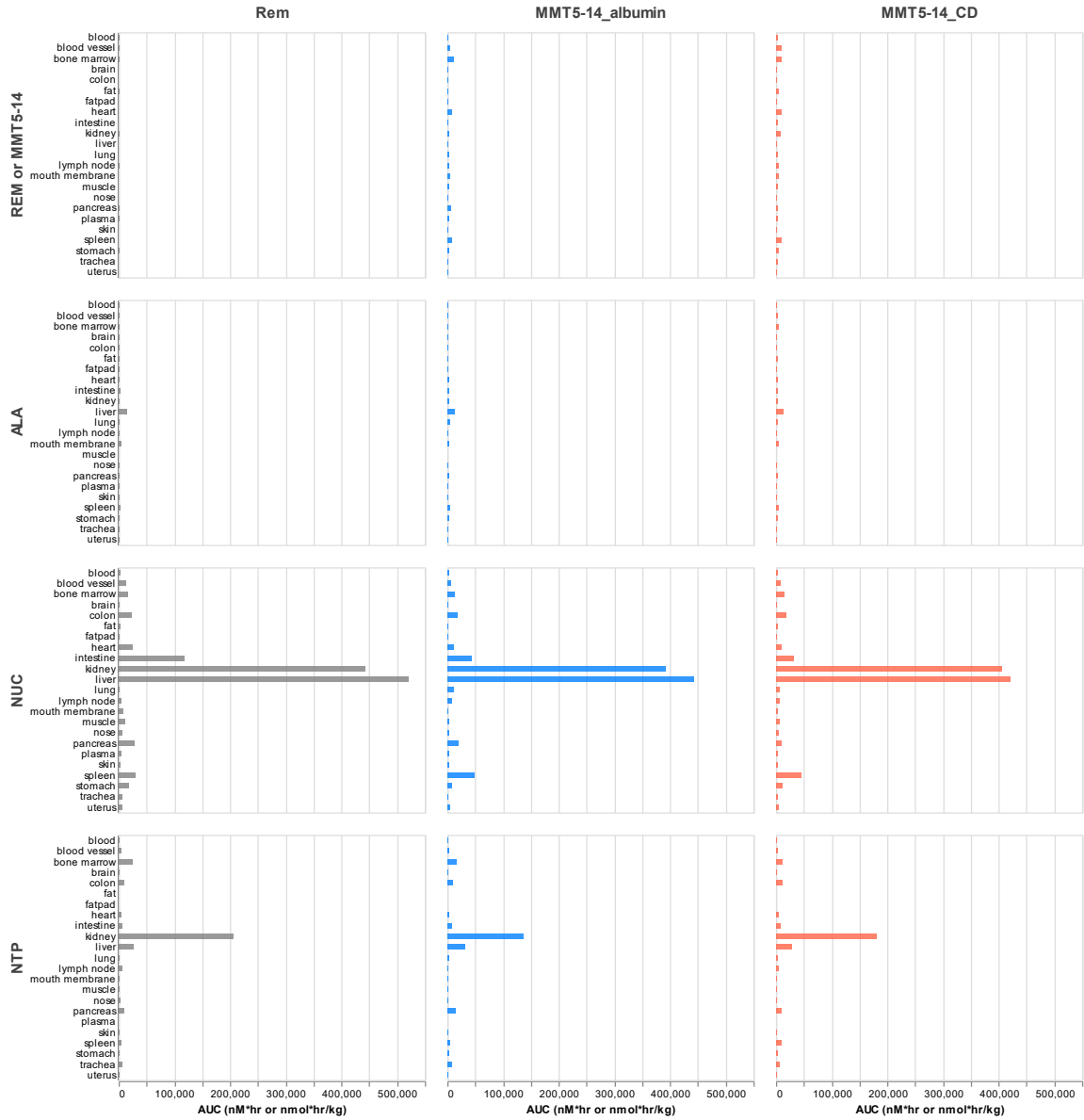


Figure 3.S2. Average AUC of collected tissues from hamsters after administration of remdesivir, MMT5-14\_albumin or MMT5-14\_CD (10 mg/kg).



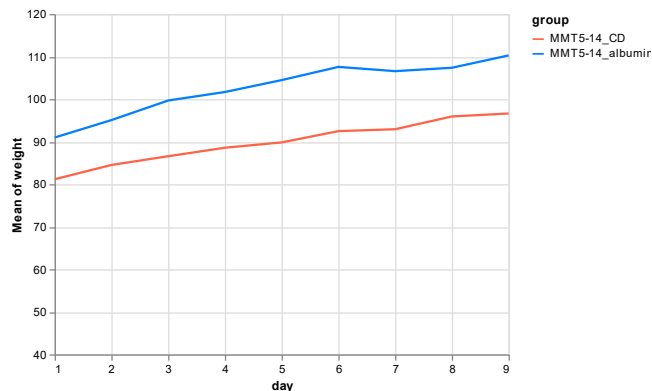


Figure 3.S3. Mean of weight change of hamsters after administration of MMT5-14\_albumin or MMT5-14\_CD (10 mg/kg, QD for 9 days in total)

	<b>t<sub>1/2</sub> (min), mean ± se</b>					
	human		hamster		mouse	
	plasma	microsome	plasma	microsome	plasma	microsome
<b>remdesivir</b>	40.7 ± 1.11	0.86 ± 0.04	54.5 ± 3.39	0.48 ± 0.01	N.D.	N.D.
<b>MMT5-1</b>	52.4 ± 3.83	1.05 ± 0.03	55.8 ± 4.36	0.46 ± 0.01	N.D.	N.D.
<b>MMT4-70</b>	47.1 ± 5.29	4.29 ± 0.11	71.2 ± 2.09	2.72 ± 0.3	N.D.	N.D.
<b>MMT4-98</b>	153.7 ± 2.40	6.11 ± 0.15	158 ± 11.9	3.49 ± 0.09	N.D.	N.D.
<b>MMT5-14</b>	191.9 ± 39.9	8.33 ± 0.61	128 ± 2.16	16.2 ± 0.44	1.03 ± 0.02	8.65 ± 0.35
<b>MMT5-15</b>	285.9 ± 137	19.7 ± 0.44	271 ± 37.8	61.82 ± 8.1	3.44 ± 0.06	13.6 ± 1.63

Table 3.1. In-vitro stability half-life time of new analogs in comparison with remdesivir. Data are represented as mean ± SE, n=3. N.D. none detected due to zero concentration of compounds due to rapid degradation.

Cell	Analytes	AUC <sub>2-12hr</sub> (ng*hr/ml)	
		MMT5-14	Rem
Calu-3	REM or MMT5-14	7515.87302	1378.98942
	ALA	37.7868254	99.9037037
	NUC	27.7067725	114.132804
	NTP	1429.87654	828.592593
	total	9011.24316	2421.61852
HUVEC	REM or MMT5-14	36527.6433	2673.53667
	ALA	130	47.2033333
	NUC	93.71	124.43
	NTP	3959.55667	3291.41667
	total	40710.91	6136.58667

Table 3.S1. Average AUC of cellular uptake in Calu-3 and HUVEC cells after incubation with remdesivir or MMT5-14 (10 uM) during 2-12 hr.

### 3.7 Bibliography

1. Jayk Bernal, A.; Gomes da Silva, M. M.; Musungaie, D. B.; Kovalchuk, E.; Gonzalez, A.; Delos Reyes, V.; Martin-Quiros, A.; Caraco, Y.; Williams-Diaz, A.; Brown, M. L.; et al. Molnupiravir for Oral Treatment of Covid-19 in Nonhospitalized Patients. *N Engl J Med* 2021.
2. Mahase, E. Covid-19: Pfizer's paxlovid is 89% effective in patients at risk of serious illness, company reports. *BMJ* 2021, 375, n2713.
3. Sanders, J. M.; Monogue, M. L.; Jodlowski, T. Z.; Cutrell, J. B. Pharmacologic Treatments for Coronavirus Disease 2019 (COVID-19) A Review. *JAMA-J AM MED ASSOC* 2020, 323, 1824-1836.
4. Eastman, R. T.; Roth, J. S.; Brimacombe, K. R.; Simeonov, A.; Shen, M.; Patnaik, S.; Hall, M. D. Remdesivir: A Review of Its Discovery and Development Leading to Emergency Use Authorization for Treatment of COVID-19. *ACS Cent Sci* 2020, 6, 672-683.
5. Beigel, J. H.; Tomashek, K. M.; Dodd, L. E.; Mehta, A. K.; Zingman, B. S.; Kalil, A. C.; Hohmann, E.; Chu, H. Y.; Luetkemeyer, A.; Kline, S.; et al. Remdesivir for the Treatment of Covid-19 - Final Report. *N Engl J Med* 2020, 383, 1813-1826.
6. Wiersinga, W. J.; Rhodes, A.; Cheng, A. C.; Peacock, S. J.; Prescott, H. C. Pathophysiology, Transmission, Diagnosis, and Treatment of Coronavirus Disease 2019 (COVID-19) A Review. *JAMA-J AM MED ASSOC* 2020, 324, 782-793.
7. Pascarella, G.; Strumia, A.; Piliengo, C.; Bruno, F.; Del Buono, R.; Costa, F.; Scarlata, S.; Agro, F. E. COVID-19 diagnosis and management: a comprehensive review. *J. Intern. Med.* 2020, 288, 192-206.
8. Consortium, W. H. O. S. T. Repurposed Antiviral Drugs for Covid-19-Interim WHO Solidarity Trial Results. *N Engl J Med* 2021, 384, 497-511.
9. Goldman, J. D.; Lye, D. C. B.; Hui, D. S.; Marks, K. M.; Bruno, R.; Montejano, R.; Spinner, C. D.; Galli, M.; Ahn, M. Y.; Nahass, R. G.; et al. Remdesivir for 5 or 10 Days in Patients with Severe Covid-19. *N Engl J Med* 2020, 383, 1827-1837.
10. Spinner, C. D.; Gottlieb, R. L.; Criner, G. J.; Lopez, J. R. A.; Cattelan, A. M.; Viladomiu, A. S.; Ogbuagu, O.; Malhotra, P.; Mullane, K. M.; Castagna, A.; et al. Effect of Remdesivir vs Standard Care on Clinical Status at 11 Days in Patients With Moderate COVID-19 A Randomized Clinical Trial. *JAMA-J AM MED ASSOC* 2020, 324, 1048-1057.
11. Kokic, G.; Hillen, H. S.; Tegunov, D.; Dienemann, C.; Seitz, F.; Schmitzova, J.; Farnung, L.; Siewert, A.; Hobartner, C.; Cramer, P. Mechanism of SARS-CoV-2 polymerase stalling by remdesivir. *Nat. Commun.* 2021, 12.
12. Warren, T. K.; Jordan, R.; Lo, M. K.; Ray, A. S.; Mackman, R. L.; Soloveva, V.; Siegel, D.; Perron, M.; Bannister, R.; Hui, H. C.; et al. Therapeutic efficacy of the small molecule GS-5734 against Ebola virus in rhesus monkeys. *NATURE* 2016, 531, 381-+.
13. Amirian, E. S.; Levy, J. K. Current knowledge about the antivirals remdesivir (GS-5734) and GS-441524 as therapeutic options for coronaviruses. *One Health* 2020, 9, 100128.
14. Williamson, B. N.; Feldmann, F.; Schwarz, B.; Meade-White, K.; Porter, D. P.; Schulz, J.; van Doremalen, N.; Leighton, I.; Yinda, C. K.; Perez-Perez, L.; et al.

- Clinical benefit of remdesivir in rhesus macaques infected with SARS-CoV-2. *NATURE* 2020, 585, 273-+.
15. Sun, D. X. Remdesivir for Treatment of COVID-19: Combination of Pulmonary and IV Administration May Offer Additional Benefit. *AAPS J.* 2020, 22.
  16. Yan, V. C.; Muller, F. L. Why Remdesivir Failed: Preclinical Assumptions Overestimate the Clinical Efficacy of Remdesivir for COVID-19 and Ebola. *Antimicrob. Agents Chemother.* 2021, 65.
  17. Malin, J. J.; Suarez, I.; Priesner, V.; Fatkenheuer, G.; Rybniker, J. Remdesivir against COVID-19 and Other Viral Diseases. *Clin. Microbiol. Rev.* 2021, 34.
  18. Li, Y.; Cao, L.; Li, G.; Cong, F.; Li, Y.; Sun, J.; Luo, Y.; Chen, G.; Li, G.; Wang, P.; et al. Remdesivir Metabolite GS-441524 Effectively Inhibits SARS-CoV-2 Infection in Mouse Models. *J Med Chem* 2021.
  19. Zhang, L. L.; Zhou, R. H. Structural Basis of the Potential Binding Mechanism of Remdesivir to SARS-CoV-2 RNA-Dependent RNA Polymerase. *J. Phys. Chem. B* 2020, 124, 6955-6962.
  20. Harrell, A. W.; Sychterz, C.; Ho, M. Y.; Weber, A.; Valko, K.; Negash, K. Interrogating the relationship between rat in vivo tissue distribution and drug property data for > 200 structurally unrelated molecules. *Pharmacol. res. perspect.* 2015, 3.
  21. Toelzer, C.; Gupta, K.; Yadav, S. K. N.; Borucu, U.; Davidson, A. D.; Williamson, M. K.; Shoemark, D. K.; Garzoni, F.; Staufer, O.; Milligan, R.; et al. Free fatty acid binding pocket in the locked structure of SARS-CoV-2 spike protein. *SCIENCE* 2020, 370, 725-+.
  22. Ramakrishnan, M. A. Determination of 50% endpoint titer using a simple formula. *World J Virol* 2016, 5, 85-86.
  23. Siegel, D.; Hui, H. C.; Doerffler, E.; Clarke, M. O.; Chun, K.; Zhang, L.; Neville, S.; Carra, E.; Lew, W.; Ross, B.; et al. Discovery and Synthesis of a Phosphoramidate Prodrug of a Pyrrolo(2,1-f)[triazin-4-amino] Adenine C-Nucleoside (GS-5734) for the Treatment of Ebola and Emerging Viruses. *J Med Chem* 2017, 60, 1648-1661.
  24. Slusarczyk, M.; Lopez, M. H.; Balzarini, J.; Mason, M.; Jiang, W. G.; Blagden, S.; Thompson, E.; Ghazaly, E.; McGuigan, C. Application of ProTide Technology to Gemcitabine: A Successful Approach to Overcome the Key Cancer Resistance Mechanisms Leads to a New Agent (NUC-1031) in Clinical Development. *J Med Chem* 2014, 57, 1531-1542.

## **CHAPTER IV - Structure-Tissue Exposure/Selectivity Relationship (STR) May Correlate with Dose-Dependent Clinical Efficacy/Safety**

### **Authors:**

*Wei Gao<sup>2,#,\*</sup>, Hongxiang Hu<sup>1,#</sup>, Lipeng Dai<sup>1,#</sup>, Miao He<sup>1</sup>, Hebao Yuan<sup>1</sup>, Huixia Zhang<sup>1</sup>, Jinhui Liao<sup>1</sup>, Bo Wen<sup>1</sup>, Yan Li<sup>2</sup>, Maria Palmisano<sup>2</sup>, Mohamed Dit Mady Traore<sup>1</sup>, Simon Zhou<sup>2</sup>, Duxin Sun<sup>1,\*</sup>*

### **4.1 Abstract**

The success rate of drug development remains at 10% despite significant effort to optimize drug with high specificity/potency and better drug-like properties based on plasma pharmacokinetics. However, drug exposure in the plasma as a surrogate of exposure in disease relevant tissues may mislead drug candidate selection and result in high clinical failure. In this study, we investigated the structure-tissue exposure/selectivity relationship (STR) to correlate with observed clinical efficacy/toxicity of a series of clinical approved or tested drugs with similar structures, same molecular target, but different clinical indications. The results showed that drug exposure in plasma was not correlated with drug exposure in the target tissues (tumor, fatpad and bone) that was associated with clinical efficacy/safety. Slight structure modification altered drug exposure/selectivity in tissues despite similar drug exposure in the plasma. STR may correlate with clinical efficacy/safety which impacts success rate of drug development.

### **4.2 Introduction**

---

1 Department of Pharmaceutical Sciences, College of Pharmacy, University of Michigan, 1600 Huron Parkway, North Campus Research Complex, Building 520, Ann Arbor, MI 48109, USA

2 Translational Development and Clinical Pharmacology, Bristol Myers Squibb, 86 Morris Avenue, Summit, NJ 07920, USA

# These authors contributed equally to the work.

\* To whom correspondence should be addressed: duxins@umich.edu; weiga@umich.edu

In the past few decades, despite of significant effort to optimize the drug discovery and development process, the success rate from clinical phase I trial to launch was less than 10%<sup>1,2</sup>. The analysis of the clinical trial data from 2010-2017 found four possible reasons for clinical failure, which included insufficient efficacy (~40-50%), unmanageable toxicity (~30%), poor drug-like properties (10-15%), and lack of commercial needs and poor strategic realignment (10-15%)<sup>1,3</sup>. In each aspect, tremendous effort has been spent improving the outcome, including high throughput screening, target validation, pharmacogenomics biomarker discovery, preclinical efficacy and toxicity prediction, optimal pharmacokinetics, and biomarker-guided selection of patients in clinical studies. However, the overall success rate of drug development remained around 10% in the past several decades. One would wonder if there have been any other aspects overlooked in lead compound selection to advance to clinical trials, which could be important to improve the success potential in balancing clinical efficacy and toxicity.

In the lead compound selection process during drug development, two important aspects of drug candidates are rigorously optimized: (1) to achieve high specificity and potency to inhibit the intended molecular target, as measured by low  $K_i$  or  $IC_{50}$  at pM or nM, where the structure-activity-relationship (SAR) has been well studied to select lead compound for clinical studies<sup>4,5</sup>; (2) to have better drug-like properties as measured by pharmacokinetics and biopharmaceutics, where pharmacokinetic and biopharmaceutic parameters with certain cut off values are usually used as acceptable compound selection criteria, such as solubility, permeability, in vitro ADME, bioavailability  $F$ , absorption rate  $K_a$ , AUC exposure,  $C_{max}$ ,  $T_{1/2}$ , clearance  $CL$  and volume distribution  $V$ <sup>6-8</sup>. Drug candidates with high exposure in the plasma and better plasma PK parameters are often selected to advance to clinical studies, while drug candidates with low exposure in the plasma are often eliminated without further development<sup>6,9</sup>.

However, drug exposure in the plasma as a surrogate of therapeutic exposure in target tissue may mislead the selection of drug candidate to clinical trials<sup>10</sup>. The philosophy of using systemic exposure to predict the pharmacologic effects is based on the well accepted “free drug hypothesis” assuming that the free drug concentration in tissue is equal to that in plasma for permeable compounds at pharmacokinetic steady state<sup>11,12</sup>. However, the hypothesis may only be applied for a few small-molecule drugs,

since many factors can cause an asymmetric free drug distribution between plasma and tissue<sup>12-18</sup>. Hence, systemic exposure as a driver of pharmacologic effects may provide limited value in drug screening and optimization<sup>19-21</sup>. However, during drug optimization, drug candidates with high exposure in the plasma are often selected, which may have either low elimination that is preferred, or low tissue distribution which is not preferred since it may result in low concentration in the target tissues (Figure 1.2). In contrast, drug with low plasma exposure is often eliminated, which may be due to either high elimination (and low bioavailability) that is not preferred and often eliminated correctly, or high tissue distribution that may be preferred depends on the tissue exposure (Figure 1.2).

Tissues drug exposure (total or unbound drug) has been considered during the selection of drug candidates in certain diseases related to brain, tumor, and lung, et al<sup>19-21</sup>. For instance, the drug level in cerebrospinal fluid (CSF) and even directly in brain have been measured and considered as a selection criterion for optimization of drugs targeting central nerve system (CNS)<sup>20, 22-25</sup>. Various of anticancer nanomedicine are developed based on enhanced drug tumor exposure but reduced vital organ exposure, in which a quantification of drug concentration in tumor is always performed in preclinical studies and been evaluated in some clinical studies<sup>26-31</sup>. Many methods have been used to estimate drug concentrations of anti-infective agents in the lung to study their the corresponding impact on disease modulation and treatment<sup>21, 32</sup>. Although it is well accepted free drug concentrations in tissues correlated to therapeutic effects, the current method to estimate free drug fraction in tissue ( $f_u$ ) most commonly using tissue homogenates, which destroys all subcellular structures, and not truly represents free drug concentration at the site of action<sup>12, 20</sup>. Instead, many preclinical and clinical studies directly used total tissue exposure or  $K_p$  (total drug in tissue/plasma ratio) to screen drug candidates and evaluate dose dependent efficacy/toxicity<sup>22-31, 33</sup>. It has been proved that transport of both free unbound drugs and protein-bound drugs are presented in normal tissues and disease-targeted tissues<sup>19-21</sup>. Previous study found that albumin-bound small molecules (tyrosine kinase inhibitors), interacting with albumin-binding proteins on vascular and in tissues and mediates tissue accumulation of these small molecules in normal tissues, which is associated with their toxicity<sup>16</sup>. In addition, the clinical

development group from AstraZeneca dedicated years to develop translational Pharmacokinetics and Pharmacodynamic (PK/PD) models, which suggested that total drug levels were preferred over free drug level in these PK/PD relationships<sup>18, 33</sup>.

However, drug exposure in disease tissues or vital organs have not been routinely applied as a criterion in drug optimization and lead compound selection for most of the drugs<sup>34</sup>. Many clinical failures of drug candidates, either due to lack of efficacy or unmanageable toxicity, may be resulted from inadequate drug exposure in target tissues, or unexpected drug accumulation in the vital organs, since the structure-tissue exposure/selectivity relationship (STR) and its correlation to efficacy/toxicity is rarely optimized. Drug candidates with similar structure but slight modifications, similar IC<sub>50</sub> to inhibit the molecular target, and similar plasma PK profile may have distinct tissue exposure/selectivity properties, which may be associated with their different clinical efficacy, different indications, and distinct toxicity profiles. Most importantly, current screening based on plasma exposure cannot provide the detail information of drug exposure in disease-targeted tissues and healthy tissues. Thus, the balance of drug exposure in disease-targeted tissues vs. healthy tissues is generally overlooked during drug screening and dose optimization. However, once these drug candidates are advanced to clinical trials, one of the most important questions is whether patient could tolerate the toxicity when the adequate efficacy is achieved. Therefore, in addition to structure-activity-relationship (SAR), understanding the structure-tissue exposure/selectivity relationship (STR) is critical to improve success rate in drug discovery and development.

In this study, we aimed to investigate the structure-tissue exposure/selectivity relationship (STR), which is correlated with observed clinical efficacy/toxicity profiles, by using a series of drug candidates that have similar or different structures, same molecular target, similar or different PK profiles in plasma. We chose seven selective estrogen receptor modulators (SERMs) in this study<sup>35</sup>, since there have been large number of SERMs with similar or different structures studied in over 600 clinical trials (<https://clinicaltrials.gov/>) for various indications including breast cancer, osteoporosis, and menopausal symptoms, where eleven of them have been approved while many others were failed in the clinical trials<sup>36, 37</sup>. We have investigated the discrepancy among the selectivity/potency (such as Ki or IC<sub>50</sub>), plasma pharmacokinetics, and distinct clinical

efficacy/toxicity of these SERMs (Table 4.S1). Furthermore, we studied tissue selectivity of these SERMs in transgenic mice bearing spontaneous breast cancer, which were associated with their distinct clinical efficacy/toxicity as observed in clinical trials. We also investigated distinct structure-tissue exposure/selectivity relationship (STR) for drugs with similar plasma PK profiles and slight structure modifications. Particularly, an enhanced tumor accumulation of the 7 small molecular SERMs compared to surrounding normal tissue was also observed. Finally, we used principal component analysis (PCA) and ordinary least squares (OLS) model to analyze the structure-tissue selectivity relationship. These data highlighted the importance of structure-tissue exposure/selectivity relationship (STR), which may correlate with drugs' clinical efficacy and toxicity profiles to improve success rate of clinical drug development.

### 4.3 Results and Discussion

**Drug exposure in tissue, but not in plasma, was associated with their clinical efficacy/toxicity.** Drug exposure in plasma was not correlated with drug exposure in target tissues in most cases. In drug development process, drug exposure in plasma (drug concentration and area under the curve, AUC) is often used as a surrogate of drug exposure in the target tissue. Drug candidate with high plasma drug exposure is often selected for further clinical studies<sup>10</sup>. To verify if drug exposure in plasma was correlated with drug exposure in target tissues, we measured the drug concentration and AUC in plasma and target tissues (tumor, fatpad, bone) after oral administration of 7 SERMs (Figure 4.1A) in transgenic mice with spontaneous breast cancer (MMTV-PyMT). As shown in Figure 4.1B to D, plasma AUCs of these seven SERMs were not correlated with AUCs in the target tissues (tumor, fatpad, bone). Three different scenarios were observed among the seven drugs: (1) nafoxidine had higher drug concentration in both the plasma and tumors than raloxifene (Figure 4.1E); (2) tamoxifen and raloxifene had similar plasma drug concentration, whereas tumor concentration of tamoxifen was 4-fold higher than raloxifene (Figure 4.1F); (3) toremifene had 1.5 to 2-fold lower plasma drug concentration than raloxifene, but 1.5-fold higher drug concentration in the tumor with raloxifene (Figure 4.1G).



Drug exposure in the tissues, not in the plasma, was correlated with drug clinical efficacy/safety. To demonstrate if drug exposure in the target tissue was better than plasma exposure to correlate with drug clinical efficacy/safety, we compared two FDA approved SERMs (tamoxifen and raloxifene) with similar plasma drug exposure and well-documented distinct efficacy/toxicity profiles<sup>38, 39</sup>. Although tamoxifen and raloxifene had similar drug exposure in the plasma (Figure 4.1E), tamoxifen exposure in the tumor and fatpad was 4 and 9 fold higher than raloxifene, respectively (Figure 4.2A). Clinically, tamoxifen was widely used in breast cancer treatment<sup>38</sup>, while raloxifene showed modest or no response in a therapeutic clinical study of breast cancer<sup>40, 41</sup>, and was only approved for breast cancer prevention in clinic (Table S1)<sup>39</sup>. A long-term observation with 81-month follow-up, a higher dose of raloxifene (60 mg/day) only retained 76% and 78% of the effectiveness of a lower dose of tamoxifen (20 mg/day) in preventing invasive disease and noninvasive disease (STAR trial, Figure 4.2B and Table S2)<sup>39, 42</sup>. Clearly, the structure-activity relationship (SAR) alone of these SERMs could not fully explain their distinct clinical efficacy (Table 4.S1). For instance, raloxifene (Ki~0.4 nM)<sup>43</sup> has around 20-fold higher binding affinity with the molecular target (human ER $\alpha$ ) and about 100-fold higher potency in inhibiting breast cancer cells (MCF-7) than tamoxifen (Ki~10nM)<sup>44-46</sup>. Even compared with the active form of tamoxifen in vivo, 4-hydroxytamoxifen, raloxifene also demonstrated similar IC50 in MCF-7 cell line<sup>45, 47, 48</sup>. Besides the discrepancy in the clinical efficacy, raloxifene (60 mg/day) has fewer risk of uterine cancer and other symptoms related to uterus (Table 4.2C). The decreased uterus toxicity of raloxifene was hypothesized that raloxifene had more estrogen antagonist properties in uterus, while tamoxifen was partial estrogen agonist<sup>36</sup>. However, raloxifene was not a complete ER antagonist in uterus since it still increased uterine weight in some preclinical studies<sup>49, 50</sup>. Our data found that raloxifene has less drug accumulation in the uterus, which may partially explain the decreased side effect in uterus (Figure 4.2C)<sup>39</sup>. Furthermore, raloxifene has lower side effects compared to tamoxifen in skin, stomach, lung and brain<sup>39</sup> (Figure 4.2C), which is in consistent with less drug accumulation in those organs(Figure 4.2A).

Drug exposure in the tissue is determined by drug exposure in the plasma and tissue:plasma partition coefficient (Kp)<sup>51</sup> (Equation 1).

$$\text{Drug exposure in the tissue} = \text{Drug exposure in the plasma} * K_p \quad (\text{Eq 1})$$

Where drug exposure in the plasma and tissue can be calculated by drug concentration vs. time curve, and  $K_p$  values can be calculated by  $C_{\text{tissue}}/C_{\text{plasma}}$  or  $AUC_{\text{tissue}}/AUC_{\text{plasma}}$ <sup>51</sup>. As shown in Table 4.1, 4.S3 and 4.S4,  $K_p$  ( $AUC_{\text{tissue}}/AUC_{\text{plasma}}$  ratio) in tissues related to clinical efficacy such as tumor, fatpad and bone were significantly different among seven SERMs despite some drugs had similar plasma AUCs. Thus, drug exposure in the plasma exposure as a surrogate of drug exposure in the target tissue was not appropriate since it neglected the differences of  $K_p$  values in various tissues for different drug candidates. For instance, although tamoxifen and raloxifene had similar drug exposure in the plasma, (Figure 4.1E), the  $K_p$  of tamoxifen in tumor and fatpad were 4 and 10-fold higher than that of raloxifene (Table 4.1), which determined its significantly higher exposure in both organs. It is worth noting that  $K_p$  can be calculated by the ratio of free fraction of drug in plasma ( $f_u$ ) vs. free fraction of drugs in tissues ( $f_{ut}$ ) at steady state ( $f_u/f_{ut}$ ). However, this calculation is based on the “free drug hypothesis” assuming that free drug concentration in tissue is equals to that in plasma<sup>11, 12</sup>, which may not be applicable here since many drugs may have an asymmetric free drug distribution between plasma and tissue even at steady state<sup>12-18</sup>.

**Drug tissue selectivity is a critical parameter that tips the balance of dose-dependent efficacy/toxicity, which was often overlooked in lead compound selection during drug development.** Dose escalation was always performed in clinical phase I/II trials where MTD is normally used for cancer treatment. MTD is often associated with the drug exposure in certain toxicity related organs<sup>52</sup>. Elevating dose can certainly reach adequate drug exposure in the target tissue, but it may also increase drug exposure in the vital organs or blood cells causing adverse effects in these healthy organs. Drug tissue selectivity is an important parameter that determines the balance among dose, efficacy, and toxicity. Drug selectivity can be described by equation 2.

$$\text{Drug tissue selectivity} = C_{\text{tissue}} / \sum C_{\text{tissue}} \text{ or } AUC_{\text{tissue}} / \sum AUC_{\text{tissue}} \quad (\text{Eq. 2})$$

where sum of  $C_{\text{tissue}}$  or  $AUC_{\text{tissue}}$  is total drug concentration or AUC in different tissues.

The ideal drug candidate is expected to have high tissue selectivity and exposure in the targeted organ for better efficacy (such as tumors) but low tissue selectivity and exposure in vital healthy organs to reduce toxicity. In contrast, if a drug candidate has high selectivity and high exposure in healthy vital organs but low in disease targeted ones, it may not be able to reach its therapeutic concentration with MTD. Further, if a drug has low selectivity and exposure in both disease targeted and healthy vital organs, it may be safe even with high drug exposure in the plasma in phase I studies, but it may lack efficacy in phase II/III studies. This dilemma should be avoided during lead compound selection in drug development to refrain from high clinical study cost. As shown in Figure 4.3A and B, the tissue exposure and selectivity were compared between tamoxifen and raloxifene. Particularly, tamoxifen selectivity in fatpad and tumor was 3-fold and 1.5-fold of raloxifene, whereas both drugs had similar bone selectivity (Figure 4.3B). Due to the different tissue selectivity, higher dose of raloxifene (60 mg QD) would only achieve 34% and 77% of exposure in fatpad and tumor compared to lower dose of tamoxifen (20 mg QD), although they could achieve similar drug exposure in the bone (Table 4.S5). This may at least partially explain why raloxifene (60 mg QD) was still less effective than tamoxifen (20 mg QD) in treatment or prevention of breast cancer although raloxifene showed higher specificity/potency against estrogen receptor (ER) from enzymatic assay or cell-based assay (lower  $K_i$  or  $IC_{50}$ )<sup>43, 45</sup>, while both drugs were effective in treating osteoporosis<sup>36</sup>.

Another example is tamoxifen vs toremifene that were both approved for treatment of breast cancer<sup>38, 53</sup>. Tamoxifen had higher tumor and fatpad tissue exposure than toremifene (Figure 4.3C), but similar selectivity in the two tissues (Figure 4.3D) and similar cytotoxicity against breast cancer cell line MCF-7 and MDA-231<sup>47, 54</sup>. Therefore, higher dose of toremifene (60 mg QD) could achieve similar drug exposure levels as compared to lower dose of tamoxifen (20 mg QD, Table 4.S6) and also demonstrated similar clinical anticancer efficacy. However, lung selectivity of toremifene were 2-fold of tamoxifen (Figure 4.3D, with same dose), thus the high dose of toremifene (60 mg QD) in clinic may lead to a 2-fold increment of drug exposure in lung compared to tamoxifen (20 mg QD, Table 4.S6). This is consistent with the clinical observation of

toremifene (60 mg QD) with an increased incidence of pulmonary embolism compared with tamoxifen (20 mg QD)<sup>53</sup>.

Dosage selection without considering tissue selectivity and exposure may lead to the failure in balancing clinical efficacy/toxicity. Typically, MTD is used in clinical trials especially for cancer patients. However, dose escalation based on MTD without considering drug exposure/selectivity in tissues may increase the failure rate of clinical trials. For instance, nafoxidine has similar binding affinity to ER with tamoxifen, and also showed efficacy in treating ER positive breast cancer<sup>55</sup>. However, nafoxidine was terminated due to its dermatologic toxicity in most patients, such as ichthyosis, cutaneous photosensitivity, and cutaneous erythema after 4 to 8 weeks of treatment<sup>56, 57</sup>. It is interesting that high dose of nafoxidine (180-270 mg daily) was used in these clinical trials to achieve clinical anticancer efficacy, while such high dose also caused chronic side effects in skin<sup>57, 58</sup>. In contrast, tamoxifen which was efficacious to treat breast cancer with 20-40 mg daily administration, caused similar but manageable skin toxicity under this low dose<sup>38</sup>. By analyzing the tissue exposure and selectivity of these two drugs (Figure 4.3E and F), we found that nafoxidine has similar or higher exposure and selectivity in tumor and fatpad, and similar exposure and selectivity in skin. Since tamoxifen (20-40 mg daily) was efficacious and safe in treating breast cancer, it would be interesting to investigate if low dose of nafoxidine could achieve similar efficacy and manageable toxicity as two drugs had comparable binding affinity to ER and similar tissue exposure and selectivity, while 10-fold higher MTD dose (180-270 mg) was clearly not optimal for nafoxidine to balance its efficacy/safety in clinical trials.

**Slight structure modification altered drug exposure and selectivity in various tissues despite similar drug exposure in the plasma.** Slight structure modifications are often performed to optimize lead compounds since these small structure changes may impact binding affinity to the molecular target and pharmacokinetics. However, it is not known if these small changes in structure may alter drug exposure in the tissues, which may impact their clinical efficacy/toxicity. Therefore, we compared the exposure and tissue selectivity in various tissues of four SERMs with very similar chemical structure: tamoxifen, toremifene, afimoxifene and droloxifene (Figure 4.4). Only one substitution is

added in toremifene (-Cl), afimoxifene (-OH) and droloxifene (-OH) compared to tamoxifen (Figure 4.4A), while afimoxifene (-OH) and droloxifene (-OH) are isomers with same -OH substitution in two different positions. The structure similarity of these four drugs were further quantitated by the euclidean distance between these molecule descriptors (Figure 4.S3).

First, we compared plasma and tissue concentration after oral administration of the four drugs, and the data shows that slight structure modification drastically altered drug bioavailability, plasma exposure, tissue exposure and selectivity (Figure 4.S4). It is not surprising that bioavailability (F) changes may change drug exposure in the plasma and in the tissues comparing tamoxifen (F 39.4%) vs. toremifene (18.5%) and droloxifene (45.3%) vs. afimoxifene (32.4 %). However, it is surprising that tamoxifen and droloxifene had similar bioavailability and exposure in the plasma, but they have distinct tissue exposure and selectivity in the lung, fatpad, fat, and tumor.

To exclude the impact of different bioavailability on tissue exposure, we further compared the tissue exposure/selectivity after the I.V administration of these four drugs with similar structure. As shown in in Figure 4.4B and C after IV injection, all four drugs had similar drug exposure in the plasma or blood, but distinct tissue exposure in most organs, such as brain, fat, fatpad, heart, intestine, kidney, liver, lung, muscle, pancreas, skin, spleen, stomach, tumor and uterus (Figure 4.4B). Tamoxifen and toremifene have over 2-fold exposure difference in the fat, intestine and skin. The exposure of tamoxifen is 26 and 4-fold higher in fat and fatpad than that of afimoxifene (Figure 4.4C). In addition, two isomers afimoxifene and droloxifene showed 4.8 and 6.8-fold exposure difference in the kidney and liver (Figure 4.4C). Moreover, tissue selectivity of these four drugs were also different as shown in Figure 4.4D. When compared tamoxifen and toremifene, tamoxifen had higher selectivity in fat, skin and intestine, whereas toremifene had higher selectivity in uterus, spleen, kidney and lung. Two isomers afimoxifene and droloxifene also showed different tissue selectivity, where droloxifene had higher selectivity in heart, uterus, spleen and tumor but lower selectivity in the liver, kidney, stomach and brain than afimoxifene. Both afimoxifene and droloxifene showed higher lung but lower pancreas selectivity compared to tamoxifen and toremifene. These data clearly suggested that slight structure modifications might drastically alter drug exposure

and selectivity in different tissues despite similar exposure in the plasma. However, these phenomena are often overlooked in lead compound selection in drug discovery and development.

However, it is worth noting that slight structure modification may also completely alter exposure and selectivity in plasma and various tissues regardless after oral or IV administration. For instance, lasofoxifene (-OH) and nafoxidine (-OMe) have slightly different substitutions at the same position (Figure 4.5A). It is not surprising that nafoxidine achieved a higher drug exposure in the plasma and in most of the tissues than lasofoxifene after oral administration since nafoxidine (83.4%) has 3-fold higher oral bioavailability than lasofoxifene (F 26.9%). (Figure 4.S5B). However, IV administration of these two drugs also showed that that slight structure modification may also alter drug exposure in both plasma and tissues. As shown in Figure 5, nafoxidine had a 2 to 3-fold higher exposure in the plasma and 6 and 8-fold higher exposure in the spleen and fat than that of lasofoxifene. In addition, two drugs also showed different tissue selectivity after i.v and p.o injection (Figure 4.5D and 4.S6). Nafoxidine had higher selectivity in stomach, liver, fat, fatpad, spleen, kidney, but lower selectivity in heart, tumor and pancreas compared to lasofoxifene.

**An enhanced tumor accumulation of small molecular drug compared to normal tissue.** We observed that all the 7 SERMs has higher drug level in tumor at the first 4 hours compared to surrounding normal tissues (fatpad) after i.v injection (Figure 4.6A-G). In particular, the tumor AUC of afimoxifene, droloxifene, lasofoxifene, raloxifene is 2.2, 3.1, 2.8 and 3.1 fold higher than normal fatpad (Table 4.S7). It is well known that tumor contains many leaky vasculatures, which lead to an enhanced infiltration of nanoparticles and small molecular binding to serum protein, such as Evan blue and doxorubicin (Figure 4.6H)<sup>26-31</sup>. Thus, the enhanced tumor infiltration at the first 4 hours of the 7 SERMs are probability due to the accumulation of protein/drug complex in addition to free drugs via leaky tumor vascular since all the hydrophobic drugs tend to have high level of protein binding.

**Principal component analysis (PCA) and ordinary least squares (OLS) analysis of structure-tissue partition relationship.** Understanding the relationship between drug structure descriptors and drug exposure in the tissues may provide guidance for drug optimization. However, current knowledge for such relationship is very limited. It has been hypothesized that drug physicochemical properties such as lipophilicity (logP), solubility, ionization (pKa), polarity (such as polar surface area, PSA), plasma protein or tissue binding, and molecular weight (MW) may influence drug exposure in the tissues<sup>59-61</sup>. This concept has been confirmed by numbers of compounds with very different structures and distinct physicochemical properties<sup>59</sup>. However, the six SERMs in our study had very similar physiochemical properties (Table 4.2). For instance, droloxifene and afimoxifene had almost the same solubility, TPSA, logP, plasma protein binding and equal molecular weight, but distinct drug exposure in various tissues. Likewise, lasofoxifene and nafoxidine had similar logP, logS, protein binding, and pKa, but they exhibit as large as 5-fold difference in fat and spleen accumulation. Thus, the commonly used physicochemical properties may not explain the difference in the drug exposure and selectivity in tissues.

To better dissect molecular structure descriptors of these drugs that may be associated with drug exposure and tissue selectivity in various tissues, we used RDKit API to collect more than 300 molecular structure descriptors (Table 4.S8) and decomposed them into 3 components through PCA analysis (Figure 4.7A). By using components instead of traditional physicochemical properties, the variance among drugs with similar structure could be better captured. More than 80% of property variance existing among these compounds has been captured by three components (Figure 4.7B). To avoid the risk of overfitting due to limited number of drugs, a simple ordinary least squares (OLS) model was used to describe the possible correlation between molecule structure properties (represented by components) and partition coefficient in different tissues (represented by  $K_p = AUC_{tissue}/AUC_{plasma}$ ). As shown in IV data from Figure 4.7C, a good linear correlation existed in several tissues including spleen, uterus, fatpad and skin by using only component 1. Higher r-square scores were observed as more components were fitted into this model, in which 11 of 17 tissues showed good linear relation when considering all three components. Similar conclusion could also be drawn

from the tissue partition coefficient  $K_p$  after oral administration (Figure 4.7C). The analysis confirmed good performance of OLS model in correlating molecular structure properties and drug's tissue partition coefficient  $K_p$  within the structure-similar drugs.

Univariate feature analysis showed that drug's tissue partition coefficient  $K_p$  correlated with different molecular properties dependent on tissues (Figure 4.S6 and Figure 4.7D). Three representative descriptors were selected to demonstrate such tissue-dependent correlations (Figure 4.7E). AUTOCORR2D\_95 had good linear relation with  $K_p$  in fatpad ( $R^2 = 0.95$ ), but not with  $K_p$  in the tumor ( $R^2 = 0.66$ ) or bone ( $R^2 = 0.23$ ). AUTOCORR2D\_36 was correlated well with  $K_p$  in tumor ( $R^2 = 0.96$ ), but not  $K_p$  in fatpad or bone. AUTOCORR2D\_43 was correlated well with  $K_p$  in bone ( $R^2 = 0.98$ ), but not  $K_p$  in fatpad or tumors. It is worth noting that these analyses are preliminary due to the limited number of compounds, more comprehensive descriptors can be inferred from these 2D or 3D descriptors to better predict the relationship between molecule structure descriptors and drug exposure in the tissues using data from more compounds in the future<sup>62, 63</sup>.

**Discussion.** The ideal lead compound for advancing to clinical studies should have two properties: (1) It has high specificity and potency against molecular target with low  $K_i$  (or low  $IC_{50}$ ) and without nonspecific binding to other irrelevant molecular targets, where structure-activity-relationship (SAR) has been well performed in drug optimization process; (2) It has high tissue exposure/selectivity in disease target tissues to exert efficacy, but low tissue exposure/selectivity in healthy tissues to reduce side effect, where the structure-tissue exposure/selectivity-relationship (STR) has been overlooked during drug optimization. Instead, the drug exposure in the plasma is often used as a surrogate of drug exposure in the targeted tissues for efficacy. Drug candidates with high plasma exposure are often selected for further clinical development while those with low plasma exposure are often terminated in early step. This selection strategy may be only appropriate for some drug candidates but not for others<sup>7</sup>. In this paper, we studied seven SERMs with similar or different structures as an example to show that drug exposure in the plasma was not correlated with drug exposure/selectivity in the targeted tissues (tumor, fatpad and bone) for most compounds (Figure 4.1). Although some compounds



(such as tamoxifen and raloxifene) had similar exposure in the plasma, their exposure/selectivity in the tissues were very different that were associated with their clinical efficacy/toxicity profiles (Figure 4.2 and 4.3). Therefore, using drug exposure in plasma to select lead compound to advance to clinical studies may significantly contribute to the high failure rate (90%) in drug development. The lack of efficacy in clinical failure may be due to the lack of drug exposure/selectivity in the disease target tissue, while unmanageable toxicity in clinical studies may be due to the high drug exposure/selectivity in the healthy vital organs in clinical dose escalation studies. However, there is no technology to directly investigate tissue exposure/selectivity in clinical patients, while tissue exposure/selectivity in preclinical model is often overlooked due to labor intensive nature of these types of studies. Furthermore, PD marker in blood cells is often used as surrogate markers for efficacy in drug development (e.g., anticancer drugs), which may also mislead the clinical studies if the disease targets are not in blood cells.

Drug exposure/selectivity in tissues that are associated with drug efficacy/toxicity should be evaluated in drug development process. In this study, we highlighted three important PK parameters (drug exposure, partition coefficient  $K_p$ , and drug selectivity in tissues), which were closely associated with drug efficacy/toxicity. Drug exposure ( $AUC_{tissue}$ ) and drug partition coefficient ( $K_p$ ) in the tissues determined the amount of drug accumulated in certain tissue (Table 4.1), while drug tissue selectivity may impact the drug's therapeutic window among efficacy, toxicity and dose (Figure 4.3). In addition, we observed that tumor has higher accumulation of the 7 SERMs compared to normal surrounding tissues (fatpad), consistently with our further observation for other small molecular compounds<sup>30</sup>. It is either because that leaky tumor vasculatures leads to an enhanced infiltration of drug/protein complex, or tumor alters the tissue affinity of drugs, which requires further investigation (Figure 4.6H)<sup>26-31</sup>.

Interestingly, drugs inhibiting the same target are often used in different clinical indications. Evaluation of drug exposure in the tissue may guide to decide which indications should be studied in clinical trial. For instance, tamoxifen and raloxifene both target to estrogen receptor, but tamoxifen is used for breast cancer treatment<sup>38</sup>, while raloxifene is approved for osteoporosis and breast cancer prevention<sup>39</sup>. Raloxifene was

initially developed for breast cancer treatment but failed in clinical trial<sup>64</sup>; and it was later tested and approved to treat osteoporosis<sup>39</sup>. Raloxifene showed more potent cytotoxicity against breast cancer cell lines compared to tamoxifen<sup>45, 65</sup> and shared a very similar plasma exposure to tamoxifen, and it is not surprising raloxifene was initially developed to treat breast cancer. However, the raloxifene exposure in the tumor and fatpad is 4 and 9-fold lower of tamoxifen; raloxifene selectivity in the tumor and fatpad is also 3 and 1.5-fold less than tamoxifen (Figure 4.2A). Although dose of raloxifene was 3-fold of tamoxifen, raloxifene could not reach the similar concentration in tumor and fatpad as compared to tamoxifen, which may at least partially explain the lack of efficacy in breast cancer patients despite its high in vitro potency. If drug exposure and selectivity in tissues were tested in early development of raloxifene, the clinical failure of raloxifene in breast cancer patients may be avoided. Similarly, lasofoxifene was approved in Europe for osteoporosis treatment in postmenopausal women at increased risk of fracture. Lasofoxifene are currently being investigated in a phase II trial for ER+, ESR1-mutant metastatic breast cancer and granted fast track designation by FDA (<https://www.targetedonc.com/view/fda-grants-fast-track-designation-to-lasofoxifene-for-er-esr1-mutant-metastatic-breast-cancer>). The initiation of clinical investigation was based on lasofoxifene's ability as an antagonist of ER $\alpha$  with Y537S mutations, its long half-life and good bioavailability, as well as better anti-tumor activity in mouse xenograft models of endocrine therapy-resistant breast cancer compared to fulvestrant. However, our data showed that the exposure of lasofoxifene in tumor and fatpad is 3.6 and 8.5-fold lower than that of tamoxifen despite a similar plasma exposure (Table 4.1)<sup>66</sup>. Thus, the clinical dose regimen of lasofoxifen should be carefully adjusted to consider the drug exposure in the fatpad/tumor rather than in plasma exposure for clinical efficacy.

It is worth noting that STR is not the only determining factor for dose-dependent clinical efficacy/toxicity, all other criteria to select drug candidates for clinical trials are also critical. Therefore, rather than focusing on either SAR or STR, the structure-tissue exposure/selectivity-activity (efficacy/toxicity) relationship (STAR) should be considered in drug optimization and lead compound selection to improve success rate of clinical drug development.

#### 4.4 Conclusion

The clinical success rate of current drug development remains to be low (<10 %) despite of significant effort to optimize each step of drug development process. During drug optimization and lead compound selection process, SAR has been rigorously performed to select high specific and potent compounds to inhibit the molecular target. In addition, drug-like properties were extensively optimized to achieve high drug exposure in the plasma. However, drug exposure in the plasma as a surrogate of therapeutic exposure in disease target tissue may mislead the selection of drug candidate and contribute to the high rate of clinical failure. In contrast, drug optimization to achieve high drug exposure/selectivity in disease target tissues may have often been overlooked in lead compound selection process. In this study, we investigated the structure-tissue exposure/selectivity relationship (STR), which was correlated with observed clinical efficacy/toxicity profiles, by using a series of clinical approved or tested drug candidates (seven selective estrogen receptor modulators, SERMs). These studied compounds have similar or slightly different structures, same molecular target, similar or different PK profiles in plasma and tissues. The results showed that drug exposure in plasma of seven SERMs was not correlated with drug exposure in the target tissues (tumor, fatpad and bone) in most cases. Drug exposure in the tissues (tumor, fatpad, bone, uterus and liver), not in the plasma, was correlated with drug clinical efficacy/toxicity. Three important pharmacokinetic parameters may impact STR that was often overlooked in lead compound selection during drug development: Drug exposure and tissue:plasma partition coefficient ( $K_p$ ) determines absolute amount of drug accumulated in certain tissue; drug tissue selectivity is a critical parameter to tip the balance among dose, efficacy, and toxicity. In addition, slight structure modification of the compounds altered drug exposure and selectivity in various tissues despite similar drug exposure in the plasma. Tumor has higher drug accumulation compared to normal surrounding tissues. Principal component analysis (PCA) and ordinary least squares (OLS) model showed decomposed molecular descriptor components may distinguish structure-tissue exposure/selectivity-relationship. These data highlighted the importance of structure-tissue exposure/selectivity relationship (STR) in drug optimization and lead compound selections to improve success rate of clinical drug development.

## 4.5 Experimental Section

**Chemicals and reagents.** Tamoxifen, toremifene and afimoxifene were purchased from Sigma-Aldrich (St. Louis, MO, USA). Droloxifene, lasofoxifene and nafoxidine were purchased from Santa Cruz Biotechnology (Dallas, TX, USA). Acetonitrile of LC-MS grade was purchased from Sigma-Aldrich (St. Louis, MO, USA). Ultrapure deionized water was obtained from a Milli-Q water system from Millipore (Bedford, MA, USA).

**Animal experiments.** Animal study were performed on female MMTV-PyMT mice (FVB/NJ background)<sup>67</sup> established by crossing FVB/NJ females (Stock No. 001800) with hemizygous FVB/N-Tg (MMTV-PyMT) 634Mul/J males (Stock No: 002374) purchased from the Jackson Laboratory (Bar Harbor, ME, USA). Female MMTV-PyMT mice, 8-12 weeks old with tumor sizes of 150-500 mm<sup>3</sup>, were dosing with tamoxifen, toremifene, afimoxifene, droloxifene, lasofoxifene or nafoxidine at 5 mg/kg by oral (P.O) or 2.5 mg/kg by i.v injection, respectively. At each time point post dosing (0.08, 0.5, 1, 2, 4, 7 h), samples of blood, plasma, bone, tumor, brain, fat, fatpad, heart, skin, uterus, intestine, kidney, liver, lung, muscle, pancreas, spleen, stomach were collected from each mouse to measure the drug concentration by LC-MS/MS. All animal experiments were performed in accordance with University of Michigan guidelines covering the humane care and use of animals in research. All animal procedures used in this study were approved by the University Committee on Use and Care Animals at the University of Michigan.

**Tissue samples preparation.** Aliquot of plasma or blood sample (40  $\mu$ L) was dispensed into a Fisher Scientific 96-well plate (Hampton, NH, USA), then mixed with 40  $\mu$ L of ice-cold acetonitrile (100%) and 120  $\mu$ L of internal standard solution (25 nM CE302 in ACN). After being vortexed for 10 min, the plate was centrifuged at 3500 revolutions per minute (rpm) for 10 min at 4 °C to precipitate the protein, and the supernatant was taken for analyze. Other tissue samples were weighed and suspended in 20% acetonitrile (80% water; 1:5 w/v), and then homogenized 4 times for 20 s each time at 6500 RPM in a Precellys Evolution system (Montigny-le-Bretonneux, France). Aliquot of the extraction

from tissue samples (40  $\mu$ L) were mixed with 40  $\mu$ L of ice-cold acetonitrile (100%) and 120  $\mu$ L of internal standard solution for analysis in the same manner as plasma samples.

**LC-MS/MS analysis of drug concentration.** The LC-MS/MS analysis was performed on ABI-5500 Qtrap (Sciex, Ontario, Canada) mass spectrometer with electrospray ionization source, interfaced with a Shimadzu high performance liquid chromatography (HPLC) system. LC system parameters were set with separation performed on a Waters Xbridge C18 column (Milford, MA, USA) (50  $\times$  2.1 mm ID, 3.5  $\mu$ m), mobile phase composed by A (100% H<sub>2</sub>O with 0.1% formic acid) and B (100% acetonitrile with 0.1% formic), and the flow rate set at 0.4 mL/min. The mass spectrometer was operated in a positive mode with multiple reaction monitoring (MRM) for analysis. The MRM transitions (Q1/Q3) were monitored with 372.2/71.5 for tamoxifen, 406.2/72 for toremifene, 388.2/71.8 for afimoxifene, 388.2/71.8 for droloxifene, 414.2/98.2 for lasofoxifene, 426.2/98 for nafoxidine or 474.2/269.2 for raloxifene. The acquisition and processing of data were conducted by Analyst Software version 1.6 from Applied Biosystems (MDS SCIEX; Carlsbad, CA, USA). The analytical assay was validated according to FDA guidance for linearity (2 to 5000 ng/mL), matrix effect, recovery, low detection limit, Quality control (QC) in different biological matrix, including plasma, blood, tumor, and each different organ homogenates.

**Pharmacokinetic.** Non-compartment model was used to calculate plasma or tissue AUC for each drug with Phoenix/WinNonlin software (version 6.4; Pharsight, Mountain View, CA, U.S.A.). AUC<sub>total</sub> (AUC<sub>last/72 h</sub> + AUC<sub>inf</sub>) was used for the comparison among different drugs and calculation of K<sub>p</sub>.

**Principal component analysis (PCA) and ordinary least squares (OLS) model.**

Molecule descriptors about different SERMs including autocorrelation descriptors, charge descriptors, logP descriptors, refractivity descriptors, compositional descriptors, topological descriptors, connectivity descriptors, composite descriptors from VOE and Kappa shape indices were collected from the open RDkit API. Descriptors were normalized and then processed by PCA analysis through scikit-learn API (module PCA

with component numbers set as 3). The OLS model to describe the correlation between components or specific descriptors (univariate feature analysis) and drug's tissue partition coefficient  $K_p$  was processed through the Linear Regression module from scikit-learn API.

#### **4.6 Figures and Tables**

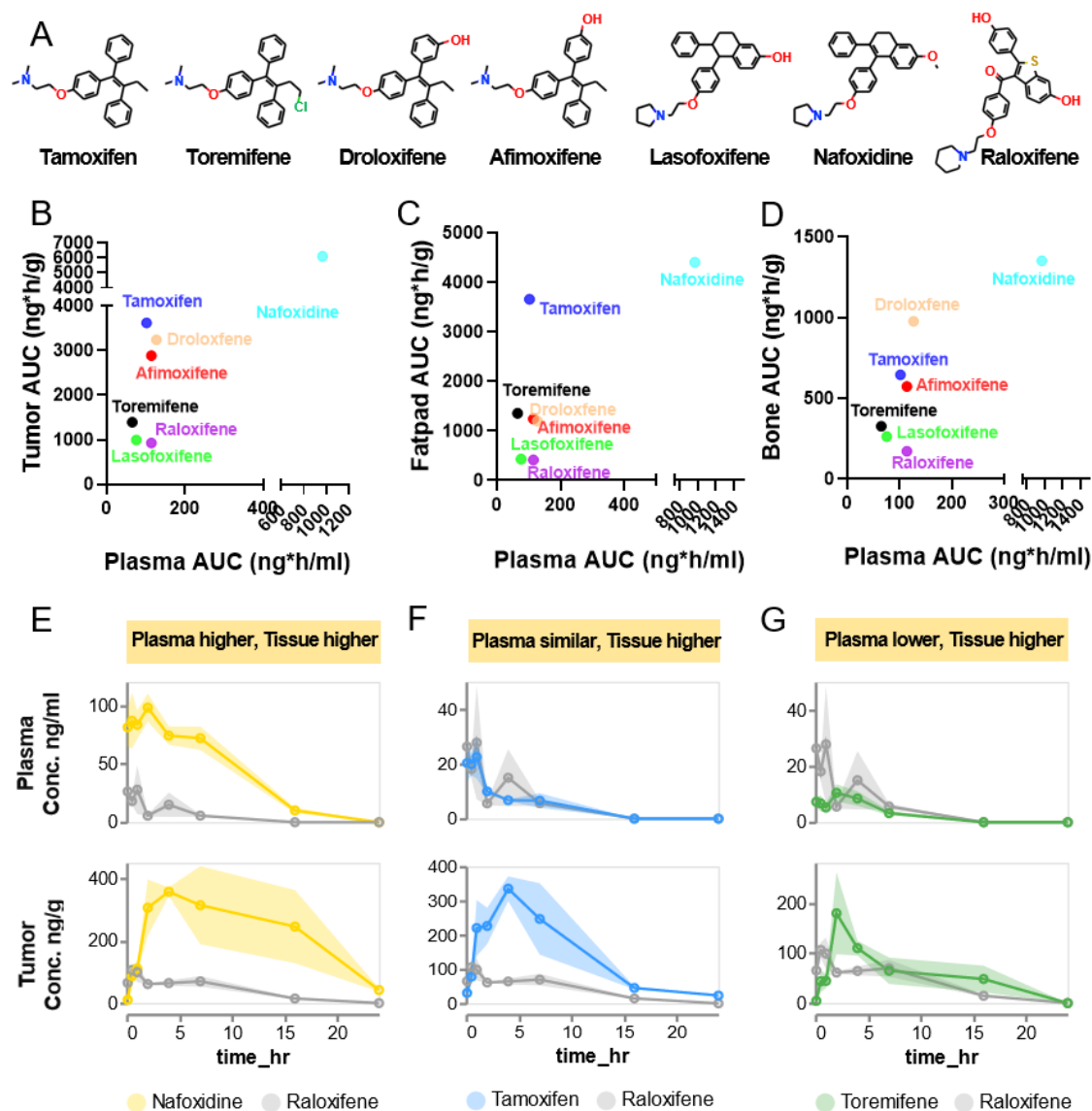
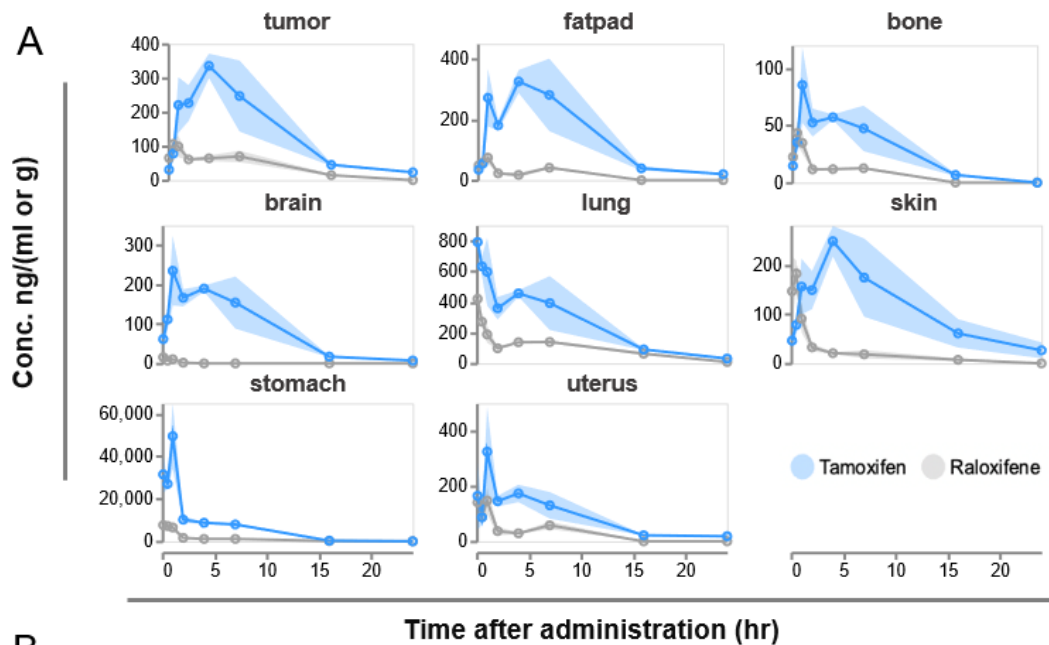


Figure 4.1. Drug exposure in the plasma was not correlated with drug exposure in the target tissue among seven SERMs with different or similar chemical structures. (A) Structures of seven SERMs. (B-D) Plasma AUC vs tissue AUC of tumor (B), fatpad (C) and bone (D). (E) Concentration-time curve of nafoxidine vs raloxifene, in which nafoxidine had higher drug concentration in the plasma and tumor. (F) Concentration-time curve of tamoxifen vs raloxifene, in which two drugs had similar plasma concentration, but tamoxifen had much higher tumor concentration. (G) Concentration-time curve of toremifene vs raloxifene, in which toremifene had lower plasma concentration, but higher drug concentration in the tumor with raloxifene. MMTV-PyMT transgenic mice with spontaneous breast cancer were orally administered with tamoxifen, toremifene, afimoxifene, droloxifene, lasofoxifene, nafoxidine and raloxifene (5.0 mg/kg). Three mice were sacrificed at each time point to collect plasma and other tissues. The drug concentration in all samples and their calculated AUC by non-compartment model were compared among different compounds (Figure S2, S3). Data in E, F, G were presented as mean  $\pm$  SD (n=3).



**B** Clinical efficacy of Tamoxifen and Raloxifene in prevention of breast cancer (STAR trial)

Outcomes	Events, n		RR*	RR (95% CI)
	Tamoxifen, 20 mg QD (n=9726)	Raloxifene, 60 mg QD (n=9745)		
<b>Invasive breast cancer</b>	247	310	1.24	1.05-1.47
<b>Noninvasive breast cancer</b>	111	137	1.22	0.95-1.59

**C**

	Uterus	Skin	Stomach	Lung	Brain
<b>Tamoxifen (20 mg QD)</b>	Uterine cancer, Endometrial hyperplasia, Vaginal bleeding, Vaginal discharge, Vaginal dryness, Altered menses, Pruritus vulvae.	Hair thinning and/or partial hair loss, Skin changes, Erythema multiforme, Stevens-Johnson syndrome, Bullous pemphigoid.	Distaste for food, Nausea and vomiting, Other gastrointestinal disorders.	Pulmonary embolism, Respiratory, Thoracic, Mediastinal disorders, Interstitial pneumonitis, Cough.	Depression, Dizziness, Light headedness, Headache.
<b>Raloxifene (60 mg QD)</b>	Vaginitis, Leukorrhea.	Rash.	-	Pulmonary embolism, Pneumonia, Laryngitis.	Vertigo, Neuralgia.

Figure 4.2. Drug exposure in the tissue, not in the plasma, was correlated with drug clinical efficacy/safety. (A) Concentration-time curve of tamoxifen vs raloxifene, in which two drugs had similar plasma concentration, but tamoxifen had much higher concentration in tumor, fatpad, bone, uterus, skin, stomach, lung and brain. (B) Clinical efficacy of tamoxifen (20mg/d) vs raloxifene (60mg/d). (C) Comparison of clinical adverse effects associated with different organs. Data of (C) and (D) were summarized from FDA labels of both drugs<sup>38, 39</sup>.



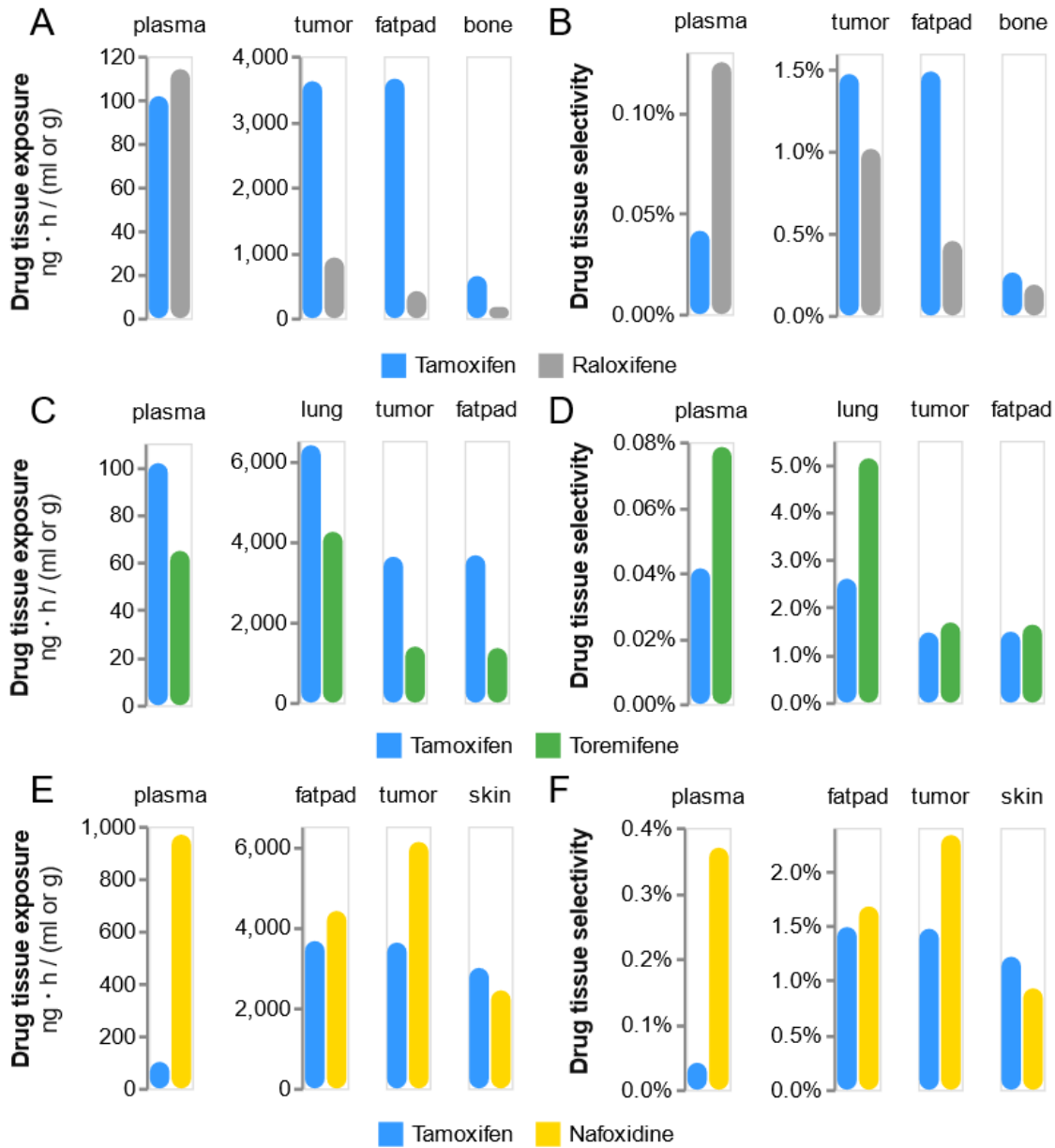


Figure 4.3. Drug tissue selectivity is a critical parameter that tips the balance of dose-dependent efficacy/toxicity. (A-B) Comparison of drug exposure (A) and selectivity (B) in tissues like tumor, fatpad and bone between tamoxifen and raloxifene after oral administration (5 mg/kg). (C-D) Comparison of drug exposure (C) and selectivity (D) in tissues like lung, tumor and fatpad between tamoxifen and toremifene after oral administration (5 mg/kg). (E-F) Comparison of drug exposure (E) and selectivity (F) in tissues like fatpad, tumor and skin between tamoxifen and nafoxidine after oral administration (5 mg/kg) in MMTV-PyMT transgenic mice with spontaneous breast cancer.

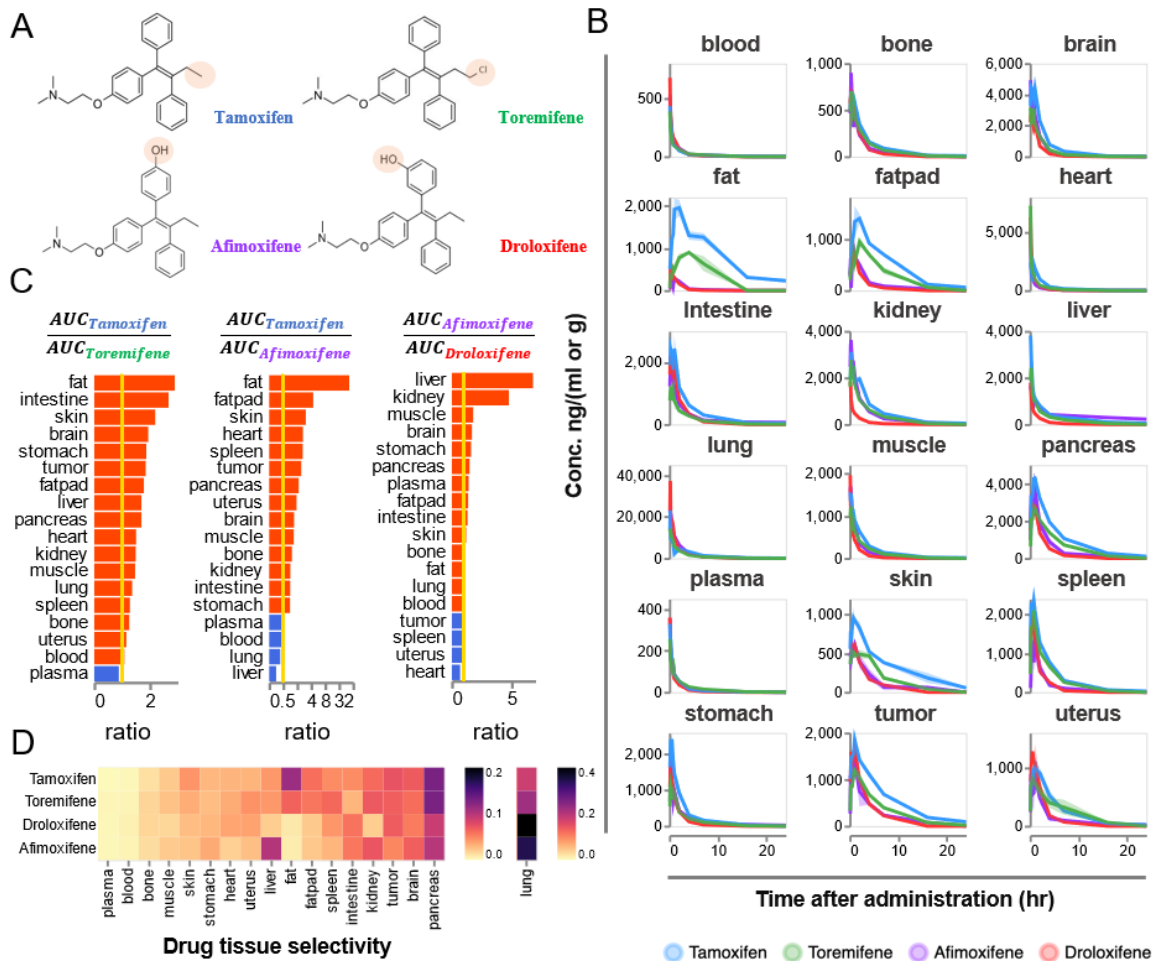


Figure 4.4. Slight structure modification altered drug exposure and selectivity in tissues despite similar exposure in the plasma. (A) The chemical structure of afimoxifene, droloxifene, tamoxifen and toremifene. (B) Concentration-time curve after I.V administration of afimoxifene, droloxifene, tamoxifen and toremifene (I.V. 2.5 mg/kg) on MMTV-PyMT transgenic mice with spontaneous breast cancer (n=3 at each time point). (C) AUC comparison of tamoxifen vs toremifene, tamoxifen vs afimoxifene and afimoxifene vs droloxifene. (D) Drug tissue selectivity calculated by  $AUC_{tissue}/AUC_{total}$  using data collected in (B).

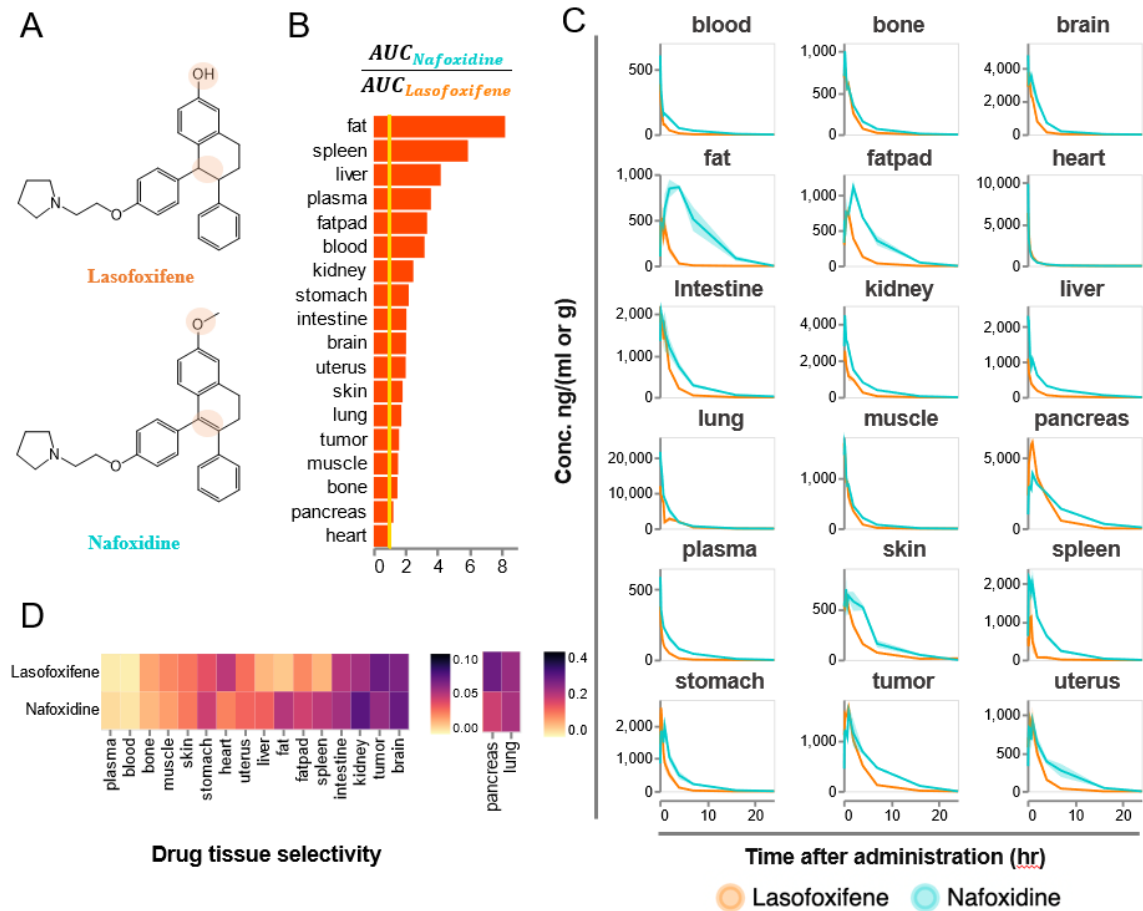


Figure 4.5. Slight structure modification altered drug exposure and selectivity in both plasma and tissues. (A) The chemical structure of lasofoxifene and nafoxidine. (B) Concentration-time curve after I.V administration of lasofoxifene and nafoxidine (IV 2.5 mg/kg) on MMTV-PyMT transgenic mice with spontaneous breast cancer (n=3 at each time point). (C) AUC comparison of nafoxidine vs lasofoxifene. (D) Drug tissue selectivity calculated by  $AUC_{tissue}/AUC_{total}$  using data collected in (B).

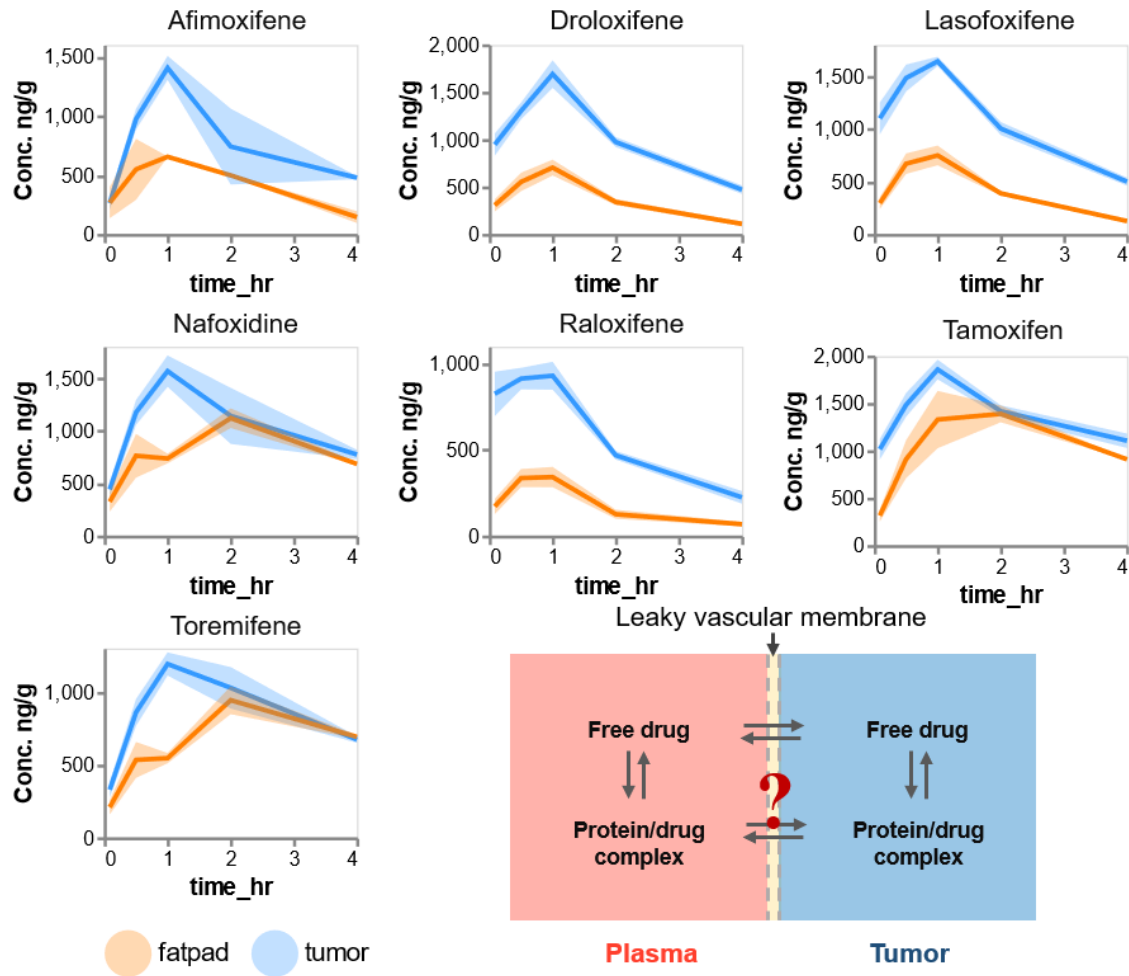


Figure 4.6 An enhanced tumor accumulation of small molecular drug compared to normal tissue. (A to G) Concentration-time curve of tumor and fatpad (normal tissue surrounding tumors) after I.V administration of different drugs (2.5 mg/kg) on MMTV-PyMT transgenic mice with spontaneous breast cancer (n=3 at each time point); (H) An illustration of mechanism of enhanced tumor accumulation. Tumor vascular are abnormal and leaky compared to vascular in normal tissue which allows more protein/drug complex enters to tumors resulting an enhanced drug accumulation in first four hours of drug distribution.

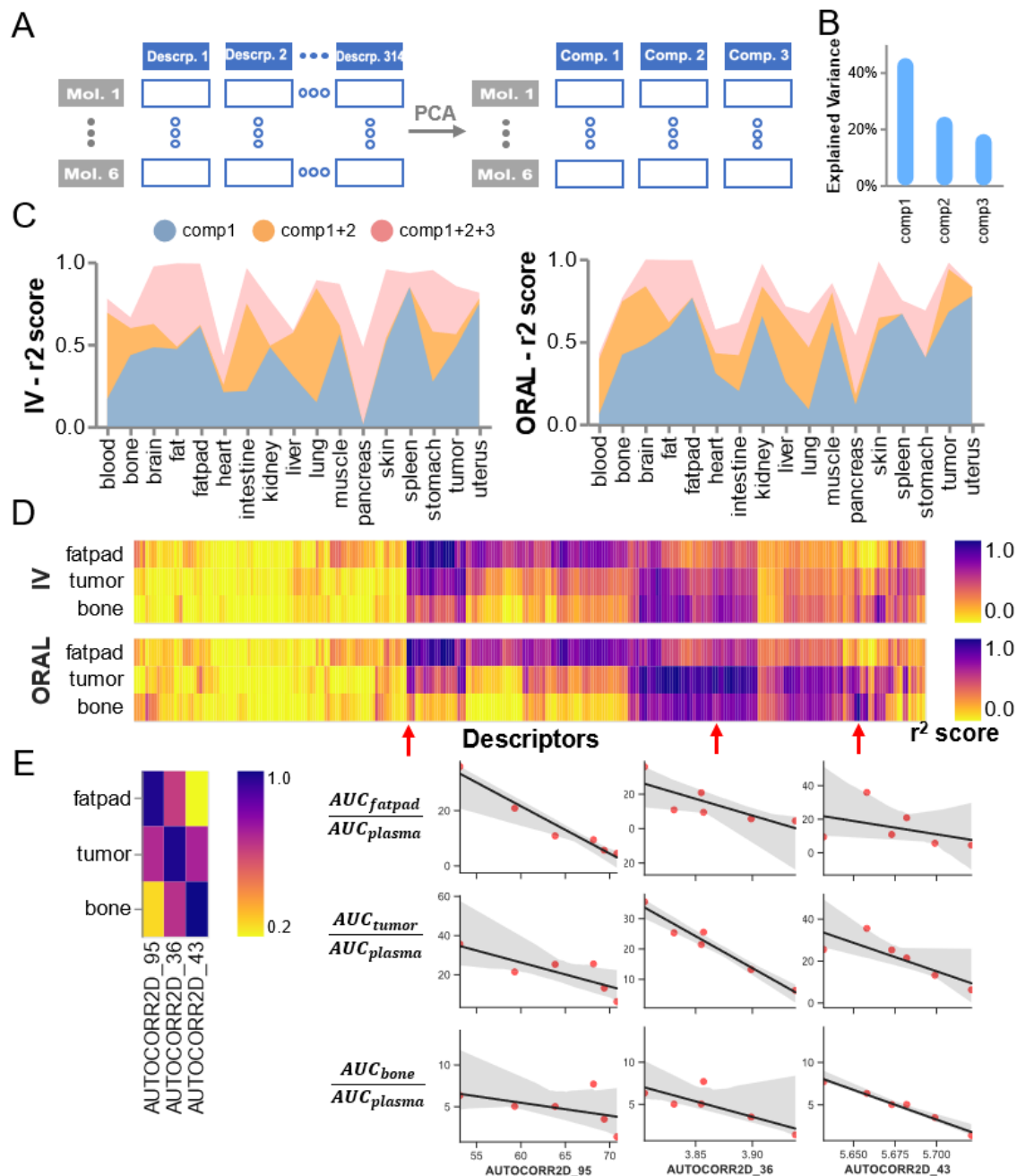


Figure 4.7. Molecular structure descriptors influence drug exposure in tissues. (A) PCA analysis to decompose molecule structure descriptors to 3 components. (B) Percentage of molecule property variance explained by components. (C) Ordinary least squares analysis of drug's partition coefficient in tissue (represented by  $K_p = AUC_{tissue}/AUC_{plasma}$ ) against molecule structure (represented by components) for both iv and oral data. (D) Univariate feature analysis of collected descriptors (clustered) in target tissues including fatpad, tumor and bone. (E) Representative descriptors selected from (D, oral) to explain the difference tissue of properties correlated to different tissues.

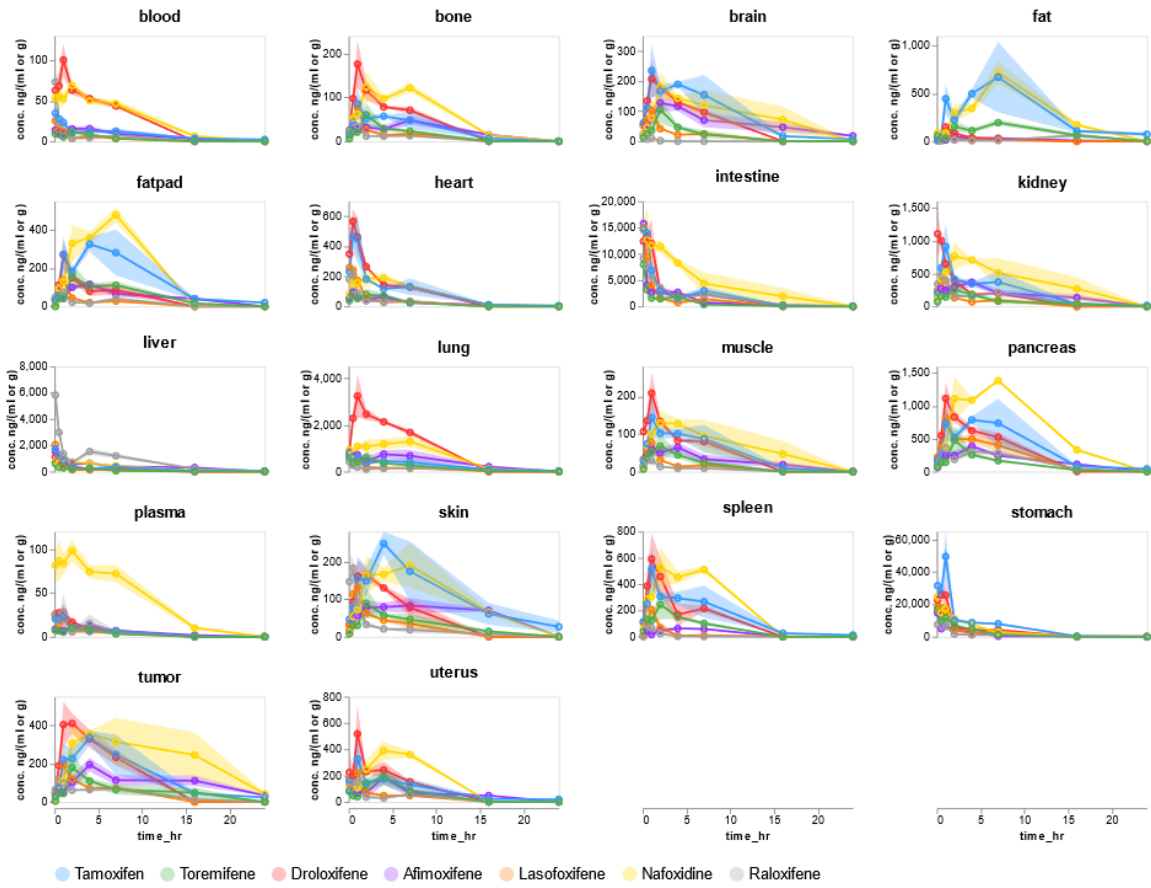


Figure 4.S1. The concentration-time curve of 7 SERMS in 18 different tissues of MMTV-PyMT transgenic mice with spontaneous breast cancer after oral administration of tamoxifen, toremifene, afimoxifene, droloxifene, lasofoxifene, nafoxidine and raloxifene (5mg/kg).

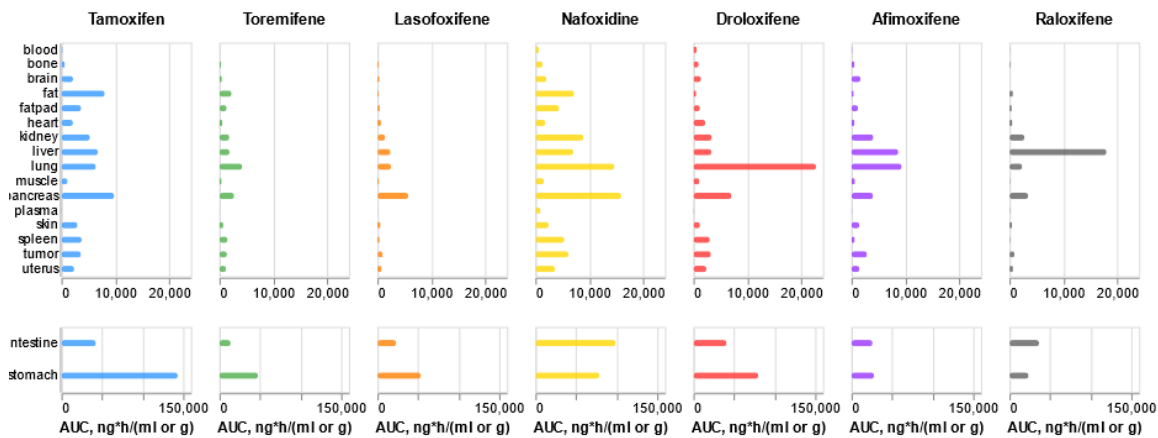


Figure 4.S2. Tissue AUC of 7 SERMs in 18 different tissues of MMTV-PyMT transgenic mice with spontaneous breast cancer after oral administration of tamoxifen, toremifene, afimoxifene, droloxifene, lasofoxifene, nafoxidine and raloxifene (5mg/kg). AUC was calculated by non-compartment model.

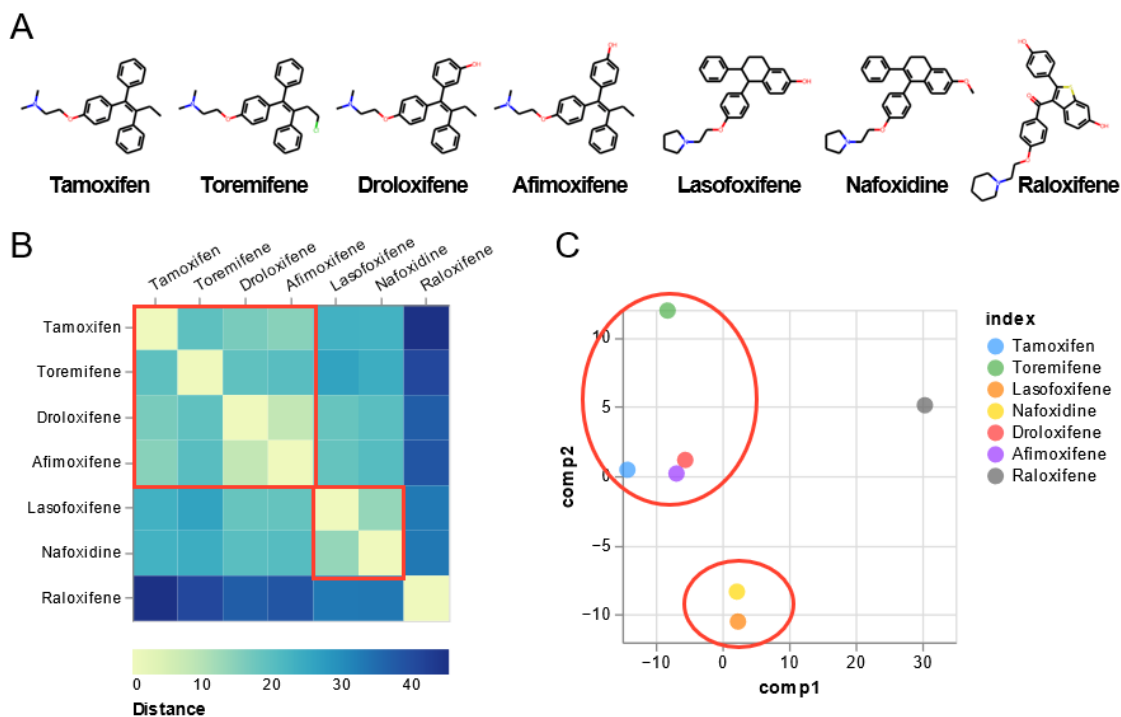


Figure 4.S3. Analysis the similarity of 7 SERMs. (A) Chemical structures; (B) Euclidean distance between molecule descriptors collected from RDkit API; (C) Distribution of 7 SERMs based on first two PCA components of descriptors from 7 SERMs.

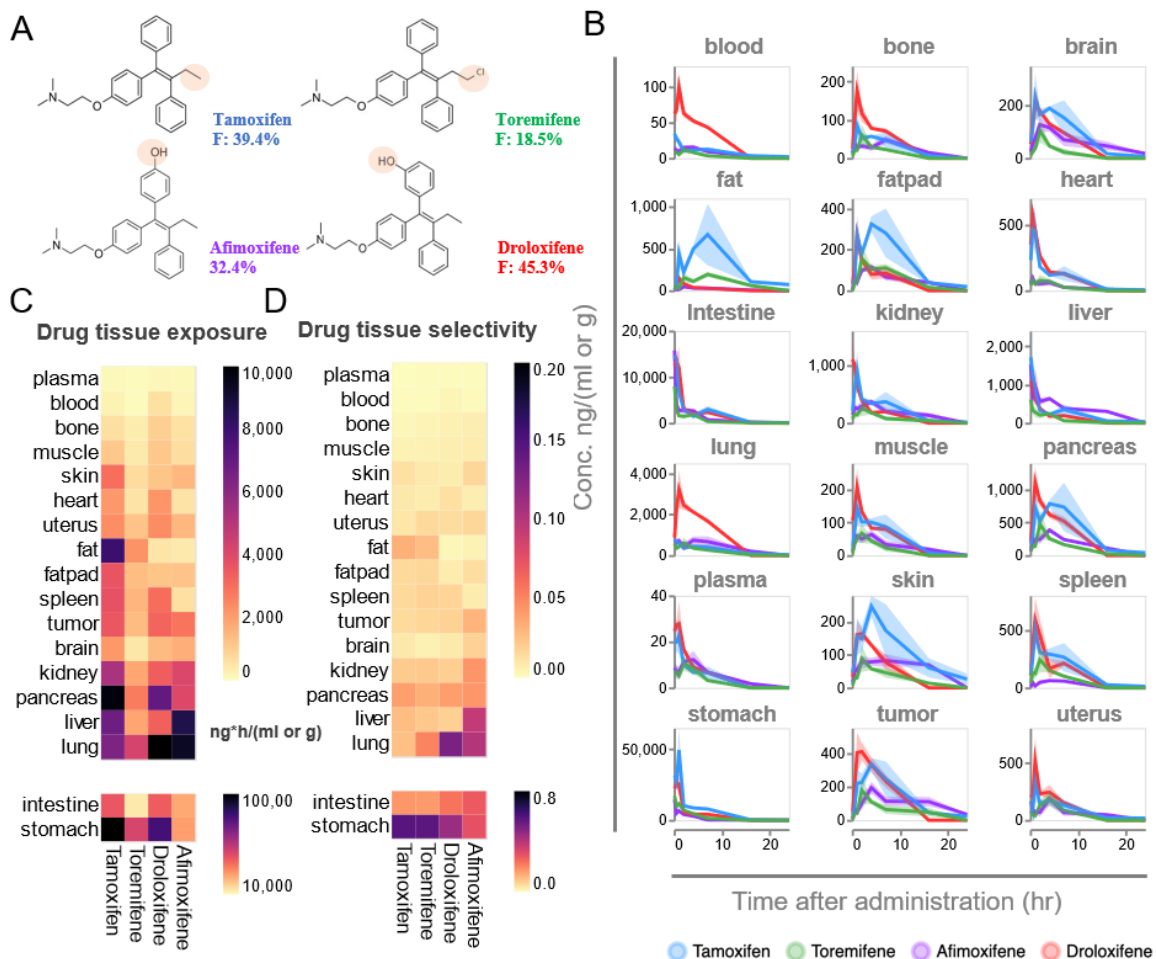


Figure 4.S4. Slight structure modification altered drug exposure and selectivity in tissues for tamoxifen, toremifene, afimoxifene and droloxifene. (A) Chemical structure; (B) Concentration-time curve after oral administration of afimoxifene, droloxifene, tamoxifen and toremifene (5 mg/kg) on MMTV-PyMT transgenic mice with spontaneous breast cancer (n=3 at each time point); (C-D) Comparison of drug tissue exposure, calculated by AUC (C) and drug tissue selectivity, calculated by  $AUC_{tissue}/AUC_{total}$  (D) among four compounds.



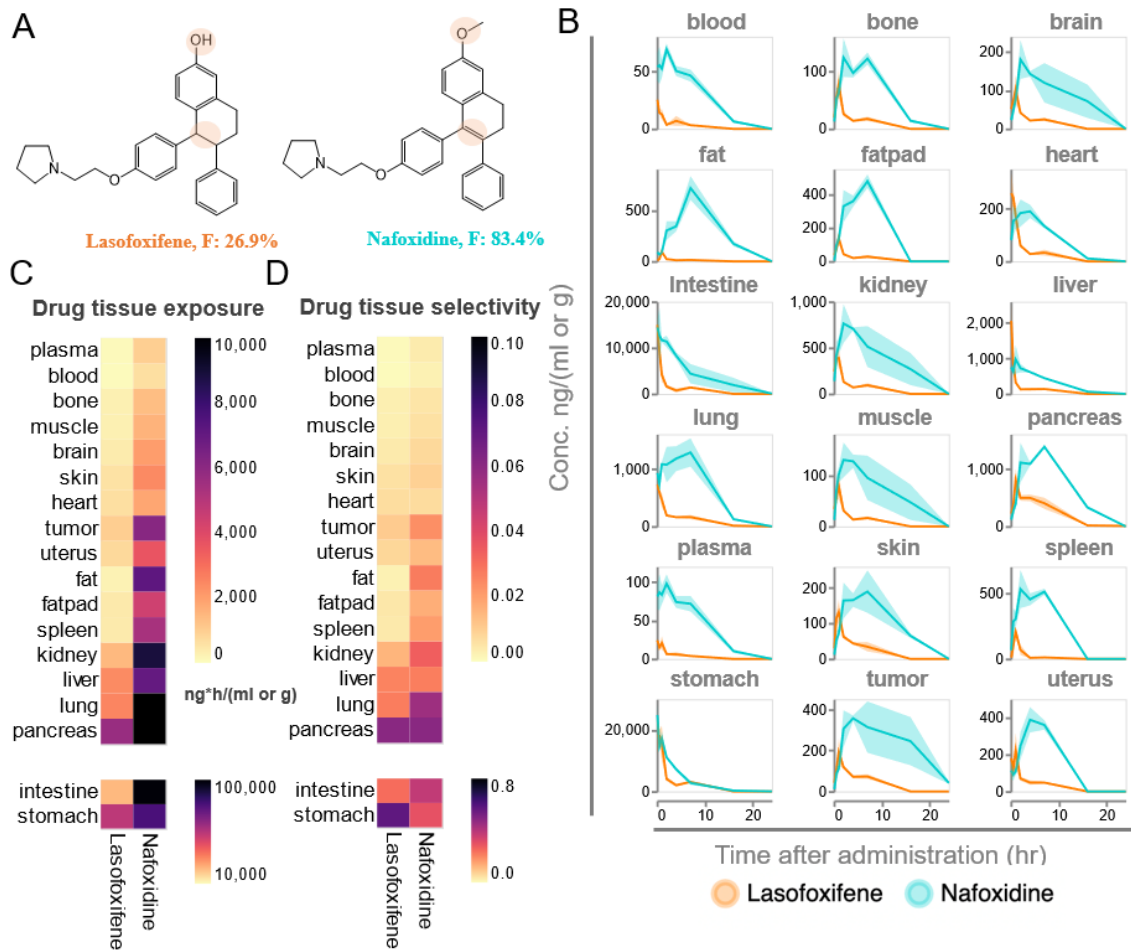


Figure 4.S5. Slight structure modification altered drug exposure and selectivity in tissues for lasofoxifene and nafoxidine. (A) Chemical structure; (B) Concentration-time curve after oral administration of lasofoxifene and nafoxidine (5 mg/kg) on MMTV-PyMT transgenic mice with spontaneous breast cancer (n=3 at each time point); (C-D) Comparison of drug tissue exposure, calculated by AUC (C) and drug tissue selectivity, calculated by  $AUC_{tissue}/AUC_{total}$  (D) among these two compounds.

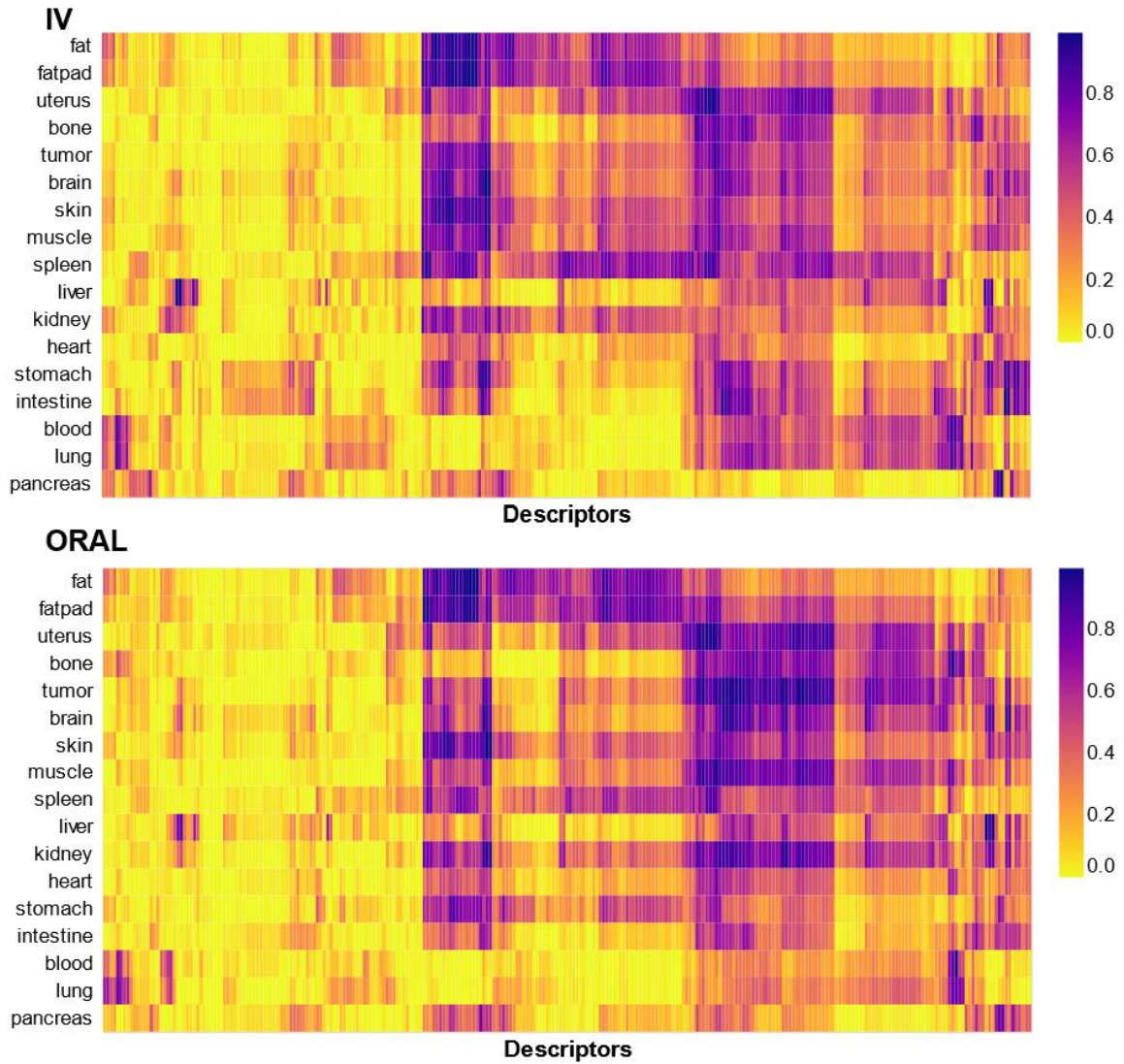


Figure 4.S6. Univariate feature analysis of collected descriptors in different tissues from mice administered by iv and oral

	<b>Toremifen</b>	<b>Lasofloxifene</b>	<b>Afimoxifene</b>	<b>Tamoxifen</b>	<b>Raloxifene</b>	<b>Droloxifene</b>	<b>Nafoxidine</b>
<b>AUC<sub>plasma</sub></b>	64.9	75.4	114	101.8	114.2	126.7	969
<b>AUC<sub>tumor</sub></b>	1393	996	2886.5	3621.3	929.4	3238.8	6118.7
<b>AUC<sub>fatpad</sub></b>	1356.2	429.8	1242.8	3660.1	416.2	1201.5	4404.8
<b>AUC<sub>bone</sub></b>	327.6	264.6	573.9	646.4	172.8	978.5	1353.1
<b>Kp<sub>tumor</sub></b>	21.5	13.2	25.3	35.6	8.1	25.6	6.3
<b>Kp<sub>fatpad</sub></b>	20.9	5.7	10.9	36	3.6	9.5	4.5
<b>Kp<sub>bone</sub></b>	5.1	3.5	5	6.3	1.5	7.7	1.4

Table 4.1. Summary of plasma and target tissues distribution kinetic parameters. Kp values were calculated by AUC<sub>tissue</sub>/AUC<sub>plasma</sub>.

	<b>Tamoxifen</b>	<b>Toremifene</b>	<b>Droloxifene</b>	<b>Afimoxifene</b>	<b>Lasofloxifene</b>	<b>Nafoxidine</b>
<b>logP</b>	5.93	5.65	5.43	5.44	6.36	6.36
<b>logS</b>	-5.6	-6	-5.1	-5.1	-6	-5.91
<b>pKa (strongest basic)</b>	8.76	8.76	8.49	8.66	8.98	8.95
<b>TPSA</b>	12.47	12.47	32.7	32.7	32.7	21.7
<b>Protein binding</b>	98%	92%	N/A	99%	99%	N/A
<b>MW</b>	371.524	405.969	387.523	387.523	413.561	425.572

Table 4.2. Physicochemical properties among SERMs with similar structure. The source of data comes from Drugbank database (go.drugbank.com).

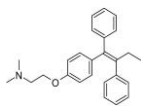
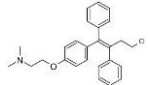
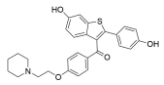
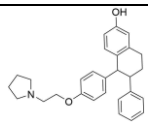
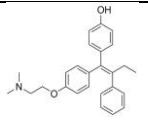
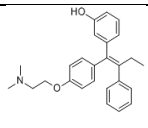
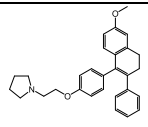
	Structure	ER binding affinity (Ki)	Indications	Status
Tamoxifen		~ 10 nM (J. Med. Chem. 1997, 40, 2117-2122)	(1) treatment of adult patients with estrogen receptor-positive metastatic breast cancer. (2) adjuvant treatment of adult patients with early-stage estrogen receptor positive breast cancer. (3) reduce risk of invasive breast cancer following breast surgery and radiation in adult women with ductal carcinoma in situ (DCIS). (4) reduce the incidence of breast cancer in adult women at high risk. (Ref: FDA label)	approved by FDA
Toremifene		N.A.	treatment of metastatic breast cancer in postmenopausal women with estrogen-receptor positive or unknown tumors. (Ref: FDA label)	approved by FDA
Raloxifene		~0.4 nM (Bioorg. Med. Chem. Lett. 2003, 13, 1907-10)	(1) treatment and prevention of osteoporosis in postmenopausal women. (2) reduction in risk of invasive breast cancer in postmenopausal women with osteoporosis. (3) reduction in risk of invasive breast cancer in postmenopausal women at high risk for invasive breast cancer. (Ref: FDA label)	approved by FDA
Lasofloxifene		1 - 10 nM (Ref: J. Med. Chem. 1998, 41, 2928-2931)	prevention and treatment of osteoporosis and for the treatment of vaginal atrophy. (Ref: <a href="https://go.drugbank.com/drugs/DB06202">https://go.drugbank.com/drugs/DB06202</a> )	approved by EMA
Afimoxifene		~0.5 nM (J. Med. Chem. 1997, 40, 2117-2122)	topical use for treatment and prevention of breast cancer, cyclic breast pain, cyclic mastalgia, atypical hyperplasia. (Ref: <a href="https://clinicaltrials.gov/">https://clinicaltrials.gov/</a> )	under clinical trails
Droloxifene		1 - 10nM (Cancer letters 1994, 84, 101-16.)	breast cancer, osteoporosis in men and postmenopausal women, and cardiovascular disorders; The drug was found to be significantly less effective than tamoxifen in the treatment of breast cancer in two phase III clinical trials. (Ref: <a href="https://en.wikipedia.org/wiki/Droloxifene">https://en.wikipedia.org/wiki/Droloxifene</a> )	abandoned
Nafoxidine		~40nM (Ref: J. Med. Chem. 1998, 41, 2928-2931)	advanced breast cancer. Effective in clinical trials but it produced side effects including ichthyosis, partial hair loss, and phototoxicity of the skin in almost all patients. (Ref: <a href="https://en.wikipedia.org/wiki/Nafoxidine">https://en.wikipedia.org/wiki/Nafoxidine</a> )	abandoned

Table 4.S1. Summary of the indications and status of 7 SERMs.

Outcomes	Events, n	
	Toremifene, 60 mg/d n=221(%)	Tamoxifen, 20 mg/d n=215(%)
<b>Response</b>		
CR <sup>1</sup> +PR <sup>2</sup>	14 + 33	11 + 30
RR <sup>3</sup> (CR+PR) %	21.3	19.1
Difference in RR	2.2	
95% CI <sup>4</sup> for Difference in RR	-5.8 to 10.2	
<b>Time to progression (TTP)</b>		
Median TTP (mo.)	5.6	5.8
Hazard Ratio (TAM/TOR)	1.01	
95% CI <sup>4</sup> for Hazard Ratio (%)	0.81 to 1.26	
<b>Survival (S)</b>		
Median S (mo.)	33.6	34.0
Hazard Ratio (TAM/TOR)	0.94	
95% CI <sup>4</sup> for Hazard Ratio (%)	0.74 to 1.24	
<b>Adverse reactions</b>		
<b>Elevated Liver Test<sup>4</sup></b>		
AST	11 (5)	4 (2)
Alkaline Phosphatase	41 (19)	24 (11)
Bilirubin	3 (1.5)	4 (2)
Hypercalcemia	6 (3)	6 (3)
Pulmonary Embolism	4 (2)	2 (1)
Vomiting	4%	2%

<sup>1</sup> CR = complete response; <sup>2</sup> PR = partial response; <sup>3</sup> RR = response rate; <sup>4</sup> CI = confidence interval; <sup>4</sup>Elevated defined as follows: North American Study: AST >100 IU/L; alkaline phosphatase >200 IU/L; bilirubin > 2 mg/dL. Eastern European and Nordic studies: AST, alkaline phosphatase, and bilirubin – WHO Grade 1 (1.25 times the upper limit of normal).

Table 4.S2. Clinical efficacy and adverse reactions of Toremifene (60 mg QD) and Tamoxifen (20 mg QD) in prevention of breast cancer (STAR trial)

	Afimoxifene	Droloxifene	Lasofloxifene	Nafoxidine	Raloxifene	Tamoxifen	Toremifene
blood	156.7	609.0	63.2	637.0	89.8	223.6	69.1
bone	573.9	978.5	264.6	1353.1	172.8	646.4	327.6
brain	1678.3	1407.2	385.5	2044.2	22.7	2151.7	456.3
fat	418.4	519.6	228.4	7176.8	696.8	8032.0	2258.1
fatpad	1242.8	1201.5	429.8	4404.8	416.2	3660.1	1356.2
heart	565.8	2199.9	654.3	1856.6	543.1	2145.8	535.6
intestine	26033.4	41065.5	23156.5	99123.8	36601.1	42602.3	13883.1
kidney	4071.5	3415.2	1458.4	8892.3	2797.6	5287.9	1839.4
liver	8685.2	3344.2	2422.7	7024.3	17985.4	6775.8	1869.7
lung	9309.9	22720.2	2538.5	14656.3	2367.4	6389.8	4240.9
muscle	657.5	1129.3	270.8	1592.0	133.0	1153.5	406.0
pancreas	4032.2	7069.4	5714.9	15911.0	3493.5	9798.6	2731.8
plasma	114.0	126.7	75.4	969.0	114.2	101.8	64.9
skin	1475.6	1209.5	567.9	2436.6	455.6	2993.1	712.9
spleen	618.5	3039.7	406.7	5361.6	184.6	3750.3	1512.6
stomach	27935.1	80074.0	53671.4	78908.4	23672.3	143714.4	47752.5
tumor	2886.5	3238.8	996.0	6118.7	929.4	3621.3	1393.0
uterus	1492.5	2398.2	770.9	3653.0	656.6	2367.2	1242.7

Table 4.S3. Tissue AUC, ng·h/(ml or g), after oral administration of 7 SERMS on MMTV-PyMT transgenic mice with spontaneous breast cancer.

	Afimoxifene	Droloxifene	Lasofloxifene	Nafoxidine	Raloxifene	Tamoxifen	Toremifene
blood	1.4	4.8	0.8	0.7	0.8	2.2	1.1
bone	5.0	7.7	3.5	1.4	1.5	6.3	5.0
brain	14.7	11.1	5.1	2.1	0.2	21.1	7.0
fat	3.7	4.1	3.0	7.4	6.1	78.9	34.8
fatpad	10.9	9.5	5.7	4.5	3.6	36.0	20.9
heart	5.0	17.4	8.7	1.9	4.8	21.1	8.3
intestine	228.4	324.1	307.1	102.3	320.5	418.5	213.9
kidney	35.7	27.0	19.3	9.2	24.5	51.9	28.3
liver	76.2	26.4	32.1	7.2	157.5	66.6	28.8
lung	81.7	179.3	33.7	15.1	20.7	62.8	65.3
muscle	5.8	8.9	3.6	1.6	1.2	11.3	6.3
pancreas	35.4	55.8	75.8	16.4	30.6	96.3	42.1
plasma	1.0	1.0	1.0	1.0	1.0	1.0	1.0
skin	12.9	9.5	7.5	2.5	4.0	29.4	11.0
spleen	5.4	24.0	5.4	5.5	1.6	36.8	23.3
stomach	245.0	632.0	711.8	81.4	207.3	1411.7	735.8
tumor	25.3	25.6	13.2	6.3	8.1	35.6	21.5
uterus	13.1	18.9	10.2	3.8	5.7	23.3	19.1

Table 4.S4. AUC<sub>tissue</sub>/AUC<sub>plasma</sub> ratio after oral administration of 7 SERMS on MMTV-PyMT transgenic mice with spontaneous breast cancer.

		Fatpad	Tumor	Bone
Raloxifene	AUC	416.2	929.4	172.8
	<b>AUC<sub>ral</sub> * 3</b>	<b>1248.6</b>	<b>2788.2</b>	<b>518.4</b>
Tamoxifen	<b>AUC</b>	<b>3660.1</b>	<b>3621.3</b>	<b>646.4</b>

Table 4.S5. Comparison of 3-fold AUC of Raloxifene and AUC of Tamoxifen in fatpad, tumor and bone. The clinical dose of Raloxifene and Tamoxifen is 60 mg, QD and 20mg, QD.

		Fatpad	Tumor	Lung
Toremifene	AUC	1356.2	1393	4240.9
	<b>AUC<sub>tor</sub> * 3</b>	<b>4068.6</b>	<b>4179</b>	<b>12722.7</b>
Tamoxifen	<b>AUC</b>	<b>3660.1</b>	<b>3621.3</b>	<b>6389.8</b>

Table 4.S6. Comparison of 3-fold AUC of Toremifene and AUC of Tamoxifen in fatpad, tumor, liver, lung and stomach. The clinical dose of Toremifene and Tamoxifen is 60 mg, QD and 20mg, QD.

	Afimoxifene	Droloxifene	Lasofloxifene	Nafoxidine	Raloxifene	Tamoxifen	Toremifene
blood	499.9	495.9	265.2	843.9	265.8	468.6	433.0
bone	1642.2	1489.3	1578.8	2346.2	644.9	2534.0	2016.0
brain	8136.6	4842.2	5392.3	10924.5	446.6	13982.6	7207.6
fat	858.9	790.2	963.1	7924.6	240.0	22680.6	7832.4
fatpad	2720.2	1990.2	2077.0	6949.4	983.6	12044.4	6756.1
heart	2305.2	3321.7	4115.2	4116.6	1388.8	6154.4	4097.0
intestine	6789.6	5174.6	4201.3	8608.0	14133.4	9628.8	3606.9
kidney	8739.7	1826.7	4634.6	11489.6	3268.4	12473.3	8385.5
liver	12189.5	1791.0	1266.2	5313.6	12847.2	8598.0	5074.8
lung	41505.8	38757.9	19349.0	33516.5	8713.3	35859.4	26323.8
muscle	2637.9	1473.5	2095.7	3195.5	879.8	4455.2	3035.6
pancreas	12016.2	8100.2	22986.0	28237.0	10191.4	26006.5	15350.6
plasma	367.8	262.1	322.0	1153.3	262.7	365.4	414.1
skin	2879.3	2409.0	2435.0	4401.6	411.9	8854.0	4041.1
spleen	3652.0	3834.5	1309.6	7729.3	275.9	9630.0	7518.1
stomach	4254.5	2639.0	3212.5	7043.6	2948.7	5993.8	3205.6
tumor	6041.5	6129.5	5787.3	9196.2	3031.4	14837.2	8031.8
uterus	3200.2	3417.3	2554.5	5115.8	732.0	6216.1	5395.4

Table 4.S7. Tissue AUC, ng·h/(ml or g), after i.v administration of 7 SERMS on MMTV-PyMT transgenic mice with spontaneous breast cancer.









Chi1	Connectivity descriptor	13.69	14.19	14.08	14.08	15.28	15.81
Chi1n	Connectivity descriptor	9.907	9.967	10.04	10.04	11.60	11.73
Chi1v	Connectivity descriptor	9.907	10.50	10.04	10.04	11.60	11.73
Chi2n	Connectivity descriptor	7.115	7.201	7.300	7.296	8.883	8.664
Chi2v	Connectivity descriptor	7.115	7.579	7.300	7.296	8.883	8.664
Chi3n	Connectivity descriptor	4.790	4.781	4.863	4.884	6.931	6.668
Chi3v	Connectivity descriptor	4.790	4.970	4.863	4.884	6.931	6.668
Chi4n	Connectivity descriptor	3.348	3.331	3.405	3.372	5.348	4.969
Chi4v	Connectivity descriptor	3.348	3.520	3.405	3.372	5.348	4.969
EState_VSA1	Electrotopological State Indices, Surface descriptor	0.000	0.000	0.000	0.000	0.000	0.000
EState_VSA2	Electrotopological State Indices, Surface descriptor	0.000	0.000	5.750	5.750	5.918	0.000
EState_VSA3	Electrotopological State Indices, Surface descriptor	6.607	12.49	6.607	6.607	11.67	0.000
EState_VSA4	Electrotopological State Indices, Surface descriptor	18.72	18.72	35.42	29.84	31.74	37.49
EState_VSA5	Electrotopological State Indices, Surface descriptor	27.84	27.84	11.14	16.71	48.18	59.33
EState_VSA6	Electrotopological State Indices, Surface descriptor	0.000	0.000	6.066	12.13	0.000	7.110
EState_VSA7	Electrotopological State Indices, Surface descriptor	0.000	26.23	44.43	44.43	12.13	0.000
EState_VSA8	Electrotopological State Indices, Surface descriptor	110.8	77.70	54.29	48.22	65.56	77.70
EState_VSA9	Electrotopological State Indices, Surface descriptor	4.737	16.34	4.737	4.737	4.737	9.474
EState_VSA10	Electrotopological State Indices, Surface descriptor	0.000	0.000	5.107	5.107	5.107	0.000
EState_VSA11	Electrotopological State Indices, Surface descriptor	0.000	0.000	0.000	0.000	0.000	0.000
ExactMolWt	Compositional descriptor	371.2	405.2	387.2	387.2	413.2	425.2
FpDensityMorgan1	Topological descriptor	0.714	0.759	0.828	0.793	0.871	0.781
FpDensityMorgan2	Topological descriptor	1.250	1.310	1.517	1.379	1.645	1.531
FpDensityMorgan3	Topological descriptor	1.786	1.862	2.138	1.931	2.419	2.281
FractionCSP3	Compositional descriptor	0.231	0.231	0.231	0.231	0.357	0.310
HeavyAtomCount	Compositional descriptor	28.00	29.00	29.00	29.00	31.00	32.00
HeavyAtomMolWt	Compositional descriptor	342.3	377.7	358.3	358.3	382.3	394.3
Ipc	Topological descriptor	2692338	4344521	3748661	3819393	27302344	4737378
Kappa1	Kappa Shape Indices	19.91	21.17	20.69	20.69	20.14	20.84
Kappa2	Kappa Shape Indices	9.911	10.848	9.944	9.944	9.152	9.621
Kappa3	Kappa Shape Indices	5.114	5.962	5.489	5.489	4.472	4.441
LabuteASA	Surface descriptor	168.6	179.0	173.4	173.4	184.9	190.8
MaxAbsEStateIndex	Electrotopological State Indices	5.871	6.215	10.07	9.744	10.01	6.047
MaxAbsPartialCharge	Charge descriptor	0.492	0.492	0.508	0.508	0.508	0.497
MaxEStateIndex	Electrotopological State Indices	5.871	6.215	10.07	9.744	10.01	6.047
MaxPartialCharge	Charge descriptor	0.119	0.119	0.119	0.119	0.119	0.119
MinAbsEStateIndex	Electrotopological State Indices	0.692	0.576	0.271	0.274	0.283	0.750
MinAbsPartialCharge	Charge descriptor	0.119	0.119	0.119	0.119	0.119	0.119
MinEStateIndex	Electrotopological State Indices	0.692	0.576	0.271	0.274	0.283	0.750
MinPartialCharge	Charge descriptor	-0.492	-0.492	-0.508	-0.508	-0.508	-0.497
MolLogP	LogP descriptor	5.996	6.215	5.702	5.702	5.729	6.075
MolMR	Refractivity descriptor	119.6	124.6	121.2	121.2	125.1	131.3
MolWt	Compositional descriptor	371.5	406.0	387.5	387.5	413.6	425.6
NHOHCount	Compositional descriptor	0.000	0.000	1.000	1.000	1.000	0.000
NOCCount	Compositional descriptor	2.000	2.000	3.000	3.000	3.000	3.000
NumAliphaticCarbocycles	Compositional descriptor	0.000	0.000	0.000	0.000	1.000	1.000
NumAliphaticHeterocycles	Compositional descriptor	0.000	0.000	0.000	0.000	1.000	1.000
NumAliphaticRings	Compositional descriptor	0.000	0.000	0.000	0.000	2.000	2.000
NumAromaticCarbocycles	Compositional descriptor	3.000	3.000	3.000	3.000	3.000	3.000
NumAromaticHeterocycles	Compositional descriptor	0.000	0.000	0.000	0.000	0.000	0.000
NumAromaticRings	Compositional descriptor	3.000	3.000	3.000	3.000	3.000	3.000
NumHAcceptors	Compositional descriptor	2.000	2.000	3.000	3.000	3.000	3.000
NumHDonors	Compositional descriptor	0.000	0.000	1.000	1.000	1.000	0.000

NumHeteroatoms	Compositional descriptor	2.000	3.000	3.000	3.000	3.000	3.000
NumRadicalElectrons	Compositional descriptor	0.000	0.000	0.000	0.000	0.000	0.000
NumRotatableBonds	Compositional descriptor	8.000	9.000	8.000	8.000	6.000	7.000
NumSaturatedCarbocycles	Compositional descriptor	0.000	0.000	0.000	0.000	0.000	0.000
NumSaturatedHeterocycles	Compositional descriptor	0.000	0.000	0.000	0.000	1.000	1.000
NumSaturatedRings	Compositional descriptor	0.000	0.000	0.000	0.000	1.000	1.000
NumValenceElectrons	Compositional descriptor	144.0	150.0	150.0	150.0	160.0	164.0
PEOE_VSA1	Charge and surface descriptor	9.637	9.637	14.74	14.74	9.843	9.474
PEOE_VSA2	Charge and surface descriptor	0.000	0.000	0.000	0.000	4.900	4.900
PEOE_VSA3	Charge and surface descriptor	0.000	0.000	0.000	0.000	0.000	0.000
PEOE_VSA4	Charge and surface descriptor	0.000	0.000	0.000	0.000	0.000	0.000
PEOE_VSA5	Charge and surface descriptor	0.000	11.60	0.000	0.000	0.000	0.000
PEOE_VSA6	Charge and surface descriptor	79.72	72.80	61.52	61.52	48.53	48.53
PEOE_VSA7	Charge and surface descriptor	60.49	60.49	72.62	72.62	91.21	96.44
PEOE_VSA8	Charge and surface descriptor	6.545	12.42	6.545	6.545	12.46	6.545
PEOE_VSA9	Charge and surface descriptor	0.000	0.000	0.000	0.000	0.000	7.110
PEOE_VSA10	Charge and surface descriptor	12.36	12.36	18.11	18.11	18.11	18.11
PEOE_VSA11	Charge and surface descriptor	0.000	0.000	0.000	0.000	0.000	0.000
PEOE_VSA12	Charge and surface descriptor	0.000	0.000	0.000	0.000	0.000	0.000
PEOE_VSA13	Charge and surface descriptor	0.000	0.000	0.000	0.000	0.000	0.000
PEOE_VSA14	Charge and surface descriptor	0.000	0.000	0.000	0.000	0.000	0.000
RingCount	Compositional descriptor	3.000	3.000	3.000	3.000	5.000	5.000
SMR_VSA1	Refractivity and Surface descriptor	4.737	4.737	9.843	9.843	9.843	9.474
SMR_VSA2	Refractivity and Surface descriptor	0.000	0.000	0.000	0.000	0.000	0.000
SMR_VSA3	Refractivity and Surface descriptor	4.900	4.900	4.900	4.900	4.900	4.900
SMR_VSA4	Refractivity and Surface descriptor	0.000	0.000	0.000	0.000	0.000	0.000
SMR_VSA5	Refractivity and Surface descriptor	13.34	6.42	13.34	13.34	37.52	25.68
SMR_VSA6	Refractivity and Surface descriptor	27.25	33.13	27.25	27.25	26.24	33.35
SMR_VSA7	Refractivity and Surface descriptor	101.6	101.6	95.55	95.55	95.05	95.05
SMR_VSA8	Refractivity and Surface descriptor	0.000	0.000	0.000	0.000	0.000	0.000
SMR_VSA9	Refractivity and Surface descriptor	5.750	5.750	11.50	11.50	11.50	11.50
SMR_VSA10	Refractivity and Surface descriptor	11.15	22.75	11.15	11.15	0.00	11.15
SlogP_VSA1	LogP and Surface descriptor	4.737	4.737	4.737	4.737	4.737	9.474
SlogP_VSA2	LogP and Surface descriptor	32.15	38.03	37.25	37.25	36.25	38.25
SlogP_VSA3	LogP and Surface descriptor	0.000	0.000	0.000	0.000	6.421	6.421
SlogP_VSA4	LogP and Surface descriptor	0.000	0.000	0.000	0.000	0.000	0.000
SlogP_VSA5	LogP and Surface descriptor	30.03	23.11	30.03	30.03	53.35	41.52
SlogP_VSA6	LogP and Surface descriptor	84.93	84.93	78.86	78.86	72.80	72.80
SlogP_VSA7	LogP and Surface descriptor	0.000	0.000	0.000	0.000	0.000	0.000
SlogP_VSA8	LogP and Surface descriptor	11.15	11.15	11.15	11.15	0.000	11.15
SlogP_VSA9	LogP and Surface descriptor	0.000	0.000	0.000	0.000	0.000	0.000
SlogP_VSA10	LogP and Surface descriptor	0.000	0.000	0.000	0.000	0.000	0.000
SlogP_VSA11	LogP and Surface descriptor	5.750	5.750	11.50	11.50	11.50	11.50
SlogP_VSA12	LogP and Surface descriptor	0.000	11.60	0.000	0.000	0.000	0.000
TPSA	Surface descriptor	12.47	12.47	32.70	32.70	32.70	21.70
VSA_EState1	Surface descriptor, Electrotopological State Indices	5.871	5.871	5.850	5.854	6.032	11.53
VSA_EState2	Surface descriptor, Electrotopological State Indices	2.123	2.114	2.102	2.105	2.479	2.485
VSA_EState3	Surface descriptor, Electrotopological State Indices	0.000	0.000	10.07	9.744	10.005	0.000
VSA_EState4	Surface descriptor, Electrotopological State Indices	6.369	6.043	5.690	5.890	5.299	7.926
VSA_EState5	Surface descriptor, Electrotopological State Indices	0.913	1.466	1.135	1.147	2.018	1.869
VSA_EState6	Surface descriptor, Electrotopological State Indices	29.82	29.44	26.15	26.22	25.44	25.91

VSA_EState7	Surface descriptor, Electrotopological State Inidices	0.968	0.802	0.885	0.904	4.715	4.688
VSA_EState8	Surface descriptor, Electrotopological State Inidices	3.826	1.569	3.708	3.729	4.175	4.187
VSA_EState9	Surface descriptor, Electrotopological State Inidices	4.110	4.094	4.073	4.077	0.000	1.735
VSA_EState10	Surface descriptor, Electrotopological State Inidices	0.000	6.215	0.000	0.000	0.000	0.000

Table 4.S8. Descriptors collected from RDKit, an open-source cross-platform cheminformatics toolkit, among SERMs with similar structures.

## 4.7 Bibliography

1. Dowden, H. & Munro, J. Trends in Clinical Success Rates and Therapeutic Focus. *Nat. Rev. Drug Discov.* 18, 495-496 (2019).
2. Takebe, T., Imai, R. & Ono, S. The Current Status of Drug Discovery and Development as Originated in United States Academia: The Influence of Industrial and Academic Collaboration on Drug Discovery and Development. *Clin Transl Sci* 11, 597-606 (2018).
3. Harrison, R.K. Phase II and Phase III Failures: 2013-2015. *Nat. Rev. Drug Discov.* 15, 817-818 (2016).
4. Wassermann, A.M., Wawer, M. & Bajorath, J. Activity Landscape Representations for Structure–Activity Relationship Analysis. *J. Med. Chem.* 53, 8209-8223 (2010).
5. Mager, D.E. Quantitative Structure-Pharmacokinetic/Pharmacodynamic Relationships. *Advanced drug delivery reviews* 58, 1326-1356 (2006).
6. Di, L., Kerns, E.H. & Carter, G.T. Drug-like Property Concepts in Pharmaceutical Design. *Current pharmaceutical design* 15, 2184-2194 (2009).
7. Davies, M. et al. Improving the Accuracy of Predicted Human Pharmacokinetics: Lessons Learned from the AstraZeneca Drug Pipeline Over Two Decades. *Trends. Pharmacol. Sci.* 41, 390-408 (2020).
8. Benet, L.Z., Hosey, C.M., Ursu, O. & Oprea, T.I. BDDCS, the Rule of 5 and Drugability. *Advanced drug delivery reviews* 101, 89-98 (2016).
9. Yusof, I. & Segall, M.D. Considering the Impact Drug-like Properties Have on the Chance of Success. *Drug discovery today* 18, 659-666 (2013).
10. Muller, P.Y. & Milton, M.N. The Determination and Interpretation of the Therapeutic Index in Drug Development. *Nat. Rev. Drug Discov.* 11, 751-761 (2012).
11. Bohnert, T. & Gan, L.S. Plasma protein binding: from discovery to development. *J Pharm Sci* 102, 2953-2994 (2013).
12. Zhang, D. et al. Drug Concentration Asymmetry in Tissues and Plasma for Small Molecule-Related Therapeutic Modalities. *Drug Metab Dispos* 47, 1122-1135 (2019).
13. Shitara, Y., Horie, T. & Sugiyama, Y. Transporters as a determinant of drug clearance and tissue distribution. *Eur J Pharm Sci* 27, 425-446 (2006).
14. Giacomini, K.M. et al. Membrane transporters in drug development. *Nature Reviews Drug Discovery* 9, 215-236 (2010).
15. Abdallah, M. et al. Lymphatic targeting by albumin-hitchhiking: Applications and optimisation. *J Control Release* 327, 117-128 (2020).
16. Ghinea, N. Anti-Angiogenic Therapy: Albumin-Binding Proteins Could Mediate Mechanisms Underlying the Accumulation of Small Molecule Receptor Tyrosine Kinase Inhibitors in Normal Tissues with Potential Harmful Effects on Health. *Diseases* 9 (2021).
17. Poulin, P., Burczynski, F.J. & Haddad, S. The Role of Extracellular Binding Proteins in the Cellular Uptake of Drugs: Impact on Quantitative In Vitro-to-In Vivo Extrapolations of Toxicity and Efficacy in Physiologically Based Pharmacokinetic-Pharmacodynamic Research. *J Pharm Sci* 105, 497-508 (2016).

18. Hendrickx, R. et al. Translational model to predict pulmonary pharmacokinetics and efficacy in man for inhaled bronchodilators. *CPT Pharmacometrics Syst Pharmacol* 7, 147-157 (2018).
19. Hammarlund-Udenaes, M. Active-site concentrations of chemicals - are they a better predictor of effect than plasma/organ/tissue concentrations? *Basic Clin Pharmacol Toxicol* 106, 215-220 (2010).
20. Gonzalez, D., Schmidt, S. & Derendorf, H. Importance of relating efficacy measures to unbound drug concentrations for anti-infective agents. *Clin Microbiol Rev* 26, 274-288 (2013).
21. Rizk, M.L., Zou, L., Savic, R.M. & Dooley, K.E. Importance of Drug Pharmacokinetics at the Site of Action. *Clin Transl Sci* 10, 133-142 (2017).
22. Charvériat, M., Lafon, V., Mouthon, F. & Zimmer, L. Innovative approaches in CNS drug discovery. *Thérapie* 76, 101-109 (2021).
23. Ghosh, K.K. et al. Positron emission tomographic imaging in drug discovery. *Drug Discov Today* (2021).
24. Smith, T.R.F. et al. Immunogenicity of a DNA vaccine candidate for COVID-19. *Nat Commun* 11, 2601 (2020).
25. Tonge, P.J. Drug-Target Kinetics in Drug Discovery. *ACS Chem Neurosci* 9, 29-39 (2018).
26. Dai, Q. et al. Quantifying the Ligand-Coated Nanoparticle Delivery to Cancer Cells in Solid Tumors. *ACS Nano* 12, 8423-8435 (2018).
27. Northfelt, D.W. et al. Doxorubicin encapsulated in liposomes containing surface-bound polyethylene glycol: pharmacokinetics, tumor localization, and safety in patients with AIDS-related Kaposi's sarcoma. *J Clin Pharmacol* 36, 55-63 (1996).
28. Harrington, K.J. et al. Effective targeting of solid tumors in patients with locally advanced cancers by radiolabeled pegylated liposomes. *Clin Cancer Res* 7, 243-254 (2001).
29. Arrieta, O. et al. High liposomal doxorubicin tumour tissue distribution, as determined by radiopharmaceutical labelling with (99m)Tc-LD, is associated with the response and survival of patients with unresectable pleural mesothelioma treated with a combination of liposomal doxorubicin and cisplatin. *Cancer Chemother Pharmacol* 74, 211-215 (2014).
30. Luan, X. et al. Reappraisal of anticancer nanomedicine design criteria in three types of preclinical cancer models for better clinical translation. *Biomaterials* 275, 120910 (2021).
31. Sun, D., Zhou, S. & Gao, W. What Went Wrong with Anticancer Nanomedicine Design and How to Make It Right. *ACS Nano* 14, 12281-12290 (2020).
32. Davies, M. et al. Improving the Accuracy of Predicted Human Pharmacokinetics: Lessons Learned from the AstraZeneca Drug Pipeline Over Two Decades. *Trends in Pharmacological Sciences* 41, 390-408 (2020).
33. Kuepfer, L. et al. Applied Concepts in PBPK Modeling: How to Build a PBPK/PD Model. *CPT Pharmacometrics Syst Pharmacol* 5, 516-531 (2016).
34. Rizk, M.L., Zou, L., Savic, R.M. & Dooley, K.E. Importance of Drug Pharmacokinetics at the Site of Action. *Clinical and translational science* 10, 133-142 (2017).



35. Martinkovich, S., Shah, D., Planey, S.L. & Arnott, J.A. Selective Estrogen Receptor Modulators: Tissue Specificity and Clinical Utility. *Clinical interventions in aging* 9, 1437-1452 (2014).
36. Komm, B.S. & Mirkin, S. An Overview of Current and Emerging SERMs. *J. Steroid Biochem. Mol. Biol.* 143, 207-222 (2014).
37. Maximov, P.Y., Lee, T.M. & Jordan, V.C. The Discovery and Development of Selective Estrogen Receptor Modulators (SERMs) for Clinical Practice. *Curr. Clin. Pharmacol.* 8, 135-155 (2013).
38. U. S. Food and Drug Administration. SOLTAMOX® (tamoxifen citrate) oral solution. Initial U.S. Approval: 1977.
39. U. S. Food and Drug Administration. EVISTA (raloxifene hydrochloride) Tablet for Oral Use. Initial U.S. Approval: 1997.
40. Buzdar, A.U., Marcus, C., Holmes, F., Hug, V. & Hortobagyi, G. Phase II Evaluation of Ly156758 in Metastatic Breast Cancer. *Oncology* 45, 344-345 (1988).
41. Gradishar, W. et al. Effects of High Dose Raloxifene in Selected Patients with Advanced Breast Carcinoma. *Cancer* 88, 2047-2053 (2000).
42. Vogel, V.G. et al. Update of the National Surgical Adjuvant Breast and Bowel Project Study of Tamoxifen and Raloxifene (STAR) P-2 Trial: Preventing breast cancer. *Cancer Prev. Res. (Phila)* 3, 696-706 (2010).
43. Wallace, O.B., Lauwers, K.S., Jones, S.A. & Dodge, J.A. Tetrahydroquinoline-Based Selective Estrogen Receptor Modulators (SERMs). *Bioorganic & medicinal chemistry letters* 13, 1907-1910 (2003).
44. Gauthier, S. et al. (S)-(+)-4-[7-(2,2-dimethyl-1-oxopropoxy)-4-methyl-2-[4-[2-(1-piperidinyl)-ethoxy]phenyl]-2H-1-benzopyran-3-yl]-phenyl 2,2-dimethylpropanoate (EM-800): a Highly Potent, Specific, and Orally Active Nonsteroidal Antiestrogen. *J. Med. Chem.* 40, 2117-2122 (1997).
45. Renaud, J. et al. Estrogen Receptor Modulators: Identification and Structure-Activity Relationships of Potent ERalpha-Selective Tetrahydroisoquinoline Ligands. *J. Med. Chem.* 46, 2945-2957 (2003).
46. Callis, R. et al. A Screening Assay Cascade to Identify and Characterize Novel Selective Estrogen Receptor Downregulators (SERDs). *Journal of biomolecular screening* 20, 748-759 (2015).
47. Chang, B.Y., Kim, S.A., Malla, B. & Kim, S.Y. The Effect of Selective Estrogen Receptor Modulators (SERMs) on the Tamoxifen Resistant Breast Cancer Cells. *Toxicological research* 27, 85-93 (2011).
48. De Savi, C. et al. Optimization of a Novel Binding Motif to (E)-3-(3,5-Difluoro-4-((1R,3R)-2-(2-fluoro-2-methylpropyl)-3-methyl-2,3,4,9-tetrahydro-1H-pyrido[3,4-b]indol-1-yl)phenyl)acrylic Acid (AZD9496), a Potent and Orally Bioavailable Selective Estrogen Receptor Downregulator and Antagonist. *J. Med. Chem.* 58, 8128-8140 (2015).
49. Sato, M., Rippy, M.K. & Bryant, H.U. Raloxifene, Tamoxifen, Nafoxidine, or Estrogen Effects on Reproductive and Nonreproductive Tissues in Ovariectomized Rats. *Faseb J.* 10, 905-912 (1996).

50. Crabtree, J.S. et al. Activity of Three Selective Estrogen Receptor Modulators on Hormone-Dependent Responses in the Mouse Uterus and Mammary Gland. *Molecular and cellular endocrinology* 287, 40-46 (2008).
51. Schmitt, W. General Approach for the Calculation of Tissue to Plasma Partition Coefficients. *Toxicol. In Vitro* 22, 457-467 (2008).
52. Koyfman, S.A. et al. Risks and Benefits Associated with Novel Phase 1 Oncology Trial Designs. *Cancer* 110, 1115-1124 (2007).
53. U. S. Food and Drug Administration. FARESTON® (toremifene citrate) , Initial U.S. Approval: 1997.
54. Xu, Z., Zhao, S.J. & Liu, Y. 1,2,3-Triazole-containing Hybrids as Potential Anticancer Agents: Current Developments, Action Mechanisms and Structure-Activity Relationships. *European journal of medicinal chemistry* 183, 111700 (2019).
55. Rosati, R.L. et al. Discovery and Preclinical Pharmacology of a Novel, Potent, Nonsteroidal Estrogen Receptor Agonist/Antagonist, CP-336156, a Diaryltetrahydronaphthalene. *J. Med. Chem.* 41, 2928-2931 (1998).
56. Legha, S.S., Slavik, M. & Carter, S.K. Nafoxidine--an antiestrogen for the treatment of breast cancer. *Cancer* 38, 1535-1541 (1976).
57. Jain, J., Samal, B., Singhakowinta, A. & Vaitkevicius, V.K. Clinical Trial of Nafoxidine in Adrenalectomized Patients with Advanced Breast Cancer. *Cancer* 40, 2063-2066 (1977).
58. Moseson, D.L. et al. The Use of Antiestrogens Tamoxifen and Nafoxidine in the Treatment of Human Breast Cancer in Correlation with Estrogen Receptor Values. A Phase II Study. *Cancer* 41, 797-802 (1978).
59. Harrell, A.W. et al. Interrogating the Relationship between Rat In Vivo Tissue Distribution and Drug Property Data for >200 Structurally Unrelated Molecules. *Pharmacology research & perspectives* 3, e00173 (2015).
60. Lombardo, F. & Jing, Y. In Silico Prediction of Volume of Distribution in Humans. Extensive Data Set and the Exploration of Linear and Nonlinear Methods Coupled with Molecular Interaction Fields Descriptors. *Journal of chemical information and modeling* 56, 2042-2052 (2016).
61. van De Waterbeemd, H., Smith, D.A., Beaumont, K. & Walker, D.K. Property-Based Design: Optimization of Drug Absorption and Pharmacokinetics. *J. Med. Chem.* 44, 1313-1333 (2001).
62. Meyer, J.G., Liu, S., Miller, I.J., Coon, J.J. & Gitter, A. Learning Drug Functions from Chemical Structures with Convolutional Neural Networks and Random Forests. *Journal of chemical information and modeling* 59, 4438-4449 (2019).
63. Mak, K.K. & Pichika, M.R. Artificial Intelligence in Drug Development: Present Status and Future Prospects. *Drug discovery today* 24, 773-780 (2019).
64. Wisinski, K.B., Tevaarwerk, A.J. & O'Regan, R.M. in *The Breast (Fifth Edition)*. (eds. K.I. Bland, E.M. Copeland, V.S. Klimberg & W.J. Gradishar) 907-923.e906 (Elsevier, 2018).
65. Sato, M., Glasebrook, A.L. & Bryant, H.U. Raloxifene: A Selective Estrogen Receptor Modulator. *J. Bone Miner. Metab.* 12, S9-S20 (1994).
66. Lainé, M. et al. Lasofoxifene as a Potential Treatment for Therapy-Resistant ER-Positive Metastatic Breast Cancer. *Breast Cancer Res.* 23, 54 (2021).

67. Guy, C.T., Cardiff, R.D. & Muller, W.J. Induction of Mammary Tumors by Expression of Polyomavirus Middle T Oncogene: a Transgenic Mouse Model for Metastatic Disease. *Mol. Cell Biol.* 12, 954-961 (1992).

## CHAPTER V - Conclusions

Based on the fact that more than 90% of drug candidates fail during clinical trials, we attempted to determine whether some crucial aspects in the current strategies for selecting clinical candidates have been overlooked, particularly related to efficacy and safety issues. Using plasma exposure of drug candidates to represent their targeted tissue exposure level and indicate their potential of clinical efficacy or toxicity may have some limitations. To explain these limitations, we started by investigating different formulations of the same compound ( e.g., APG-1252). The new formulation of APG-1252 was found to have low systemic exposure but high accumulation in target tissues such as the spleen and BM. This discrepancy was possibly caused by the influence of the formulation on biodistribution of the compound, which is more obvious in special formulations such as nanoformulations. Next, we investigated similar compounds with different metabolic stabilities (remdesivir and its analogs as an example). Owing to the high stability of the synthesized remdesivir analogs, high systemic exposure of the prodrug and active metabolite NTP was observed in analogs. However, this phenomenon was not universal to other tissues when considering the amount of NTP generated. Instead, in most tissues, stable remdesivir analogs showed a lower exposure to NTP. It was found that the high concentration of NTP in the blood was attributed to the preferred accumulation of analogs (lipid modification) in the circulation system. Other tissues with increased accumulation of analogs included the lung, which showed a 4- to 5-fold higher exposure to NTP. It was the increased blood or lung selectivity of remdesivir analogs rather than their improved stability that primarily contributed to higher NTP generation in these tissues. Finally, we investigated different compounds with the same target (e.g., SERMs). Upon analyzing drug exposure in the plasma and target tissues (tumor, fatpad, and bone) for selected SERMs (tamoxifen, toremifene, droloxifene, afimoxifene,

lasofoxifene, nafoxidine, and raloxifene), we did not find a correlation between them. The comparison between tamoxifen and raloxifene further confirmed that drug exposure in the tissues, not in the plasma, was correlated with drug clinical efficacy and safety.

Throughout our studies, we focused on the investigation of tissue selectivity. The contents of chapter II describe improvement of tissue selectivity through special formulation; the contents of chapter III describe improvement in tissue selectivity through structural modification; and chapter IV presents the study of STR.

As described in chapter II (Figure 5.1), *Nanomedicine of BCL-2/BCL-XL Inhibitors Improve Tissue Targeting, Reduce Platelet Toxicity, and Enhance Anticancer Efficacy in Myeloproliferative Neoplasm and Lymphoma*, an albumin-based nanoformulation of APG-1252 was successfully prepared in this study using the nab® technology. Nano-1252 showed encouraging results in terms of both decreased thrombocytopenia and enhanced accumulation in target tissues such as the spleen and BM. The in vivo performance of nano-1252 was mainly attributed to its high formulation stability. Because of this, nano-1252 maintained the forms of nanoparticles after administration, functioning to protect its fast metabolism to APG-1244 in the blood. On the other hand, in nano-1252, the biodistribution of APG-1252 was remarkably altered. Owing to the biological function of MPS in engulfing external particles, a large amount of nano-1252 was trapped in the spleen and BM, resulting in high accumulation in these tissues and low concentration in the circulation system. The low blood exposure to nano-1252, together with its protective action on APG-1252 and APG-1244, explains why nano-1252 could reduce platelet toxicity. The high accumulation of nano-1252 in tissues such as the spleen and BM, particularly its diffusive distribution in the red pulp area and mantle cell zone of the spleen, could benefit the treatment of different diseases such as MPNs and mantle cell lymphoma. In our tumor mouse models, nano-1252 prolonged the survival rate, delayed paralysis occurrence, and reduced tumor infiltration in the spleen and BM when compared to clinical-1252.

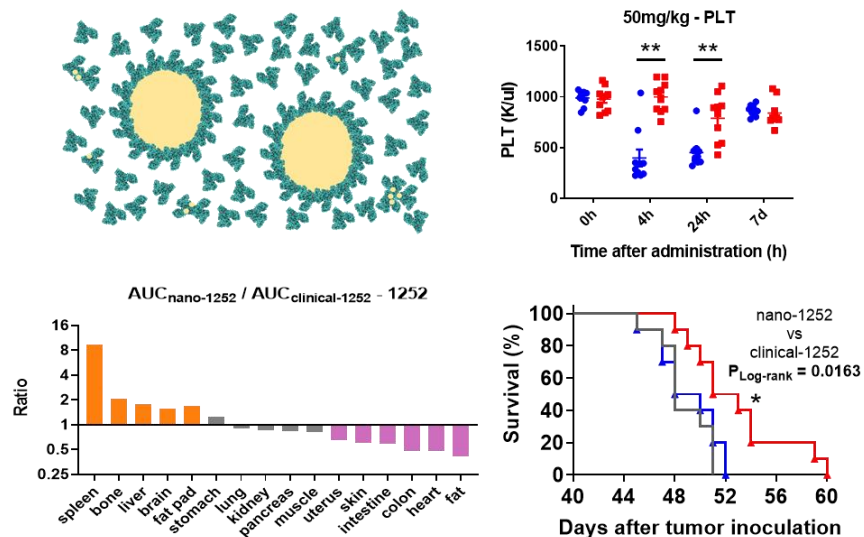


Figure 5.1. Summary of Chapter II

As described in chapter III (Figure 5.2), *Drug Optimization of Anti-SARS-Cov-2 Candidate to Improve Lung Targeting and Enhance Efficacy in Treatment of COVID-19*, we could successfully improve the in-vitro and in-vivo stability of remdesivir by optimizing the ester moiety with long lipid chains and the phenyl moiety with a naphthyl group. In comparison with remdesivir, our best compound MMT5-14, with an LA modification in the ester showed (1) 5-fold better stability in human and hamster plasma, (2) over 4-fold improvement in the antiviral activities against all SARS-CoV-2 variants, and (3) 5-fold higher NTP accumulation in the lung tissue. To the best of our knowledge, this study is the first to explore the biodistribution of remdesivir and its metabolites in detail. It becomes clearer that NUC behaves as the major metabolite of remdesivir, and its toxicity in the liver and kidney could be related to high accumulation of NUC and NTP in these tissues (Figure 3.S2). Notably, MMT5-14 showed a relatively lower exposure of NUC and NTP in toxicity-related tissues (Figure 3.3A), suggesting a possible lower toxicity profile. From the whole picture of the biodistribution of remdesivir and MMT5-14, two major conclusions can be drawn regarding our analog: 1) MMT5-14 delayed the fast metabolism of the parent compound to NUC, and 2) MMT5-14 altered the tissue distribution of remdesivir and specifically tilted slightly more towards the lung (around 1%), which in turn resulted in a 5- to 10-fold higher drug exposure (compared to 0.17% with remdesivir).

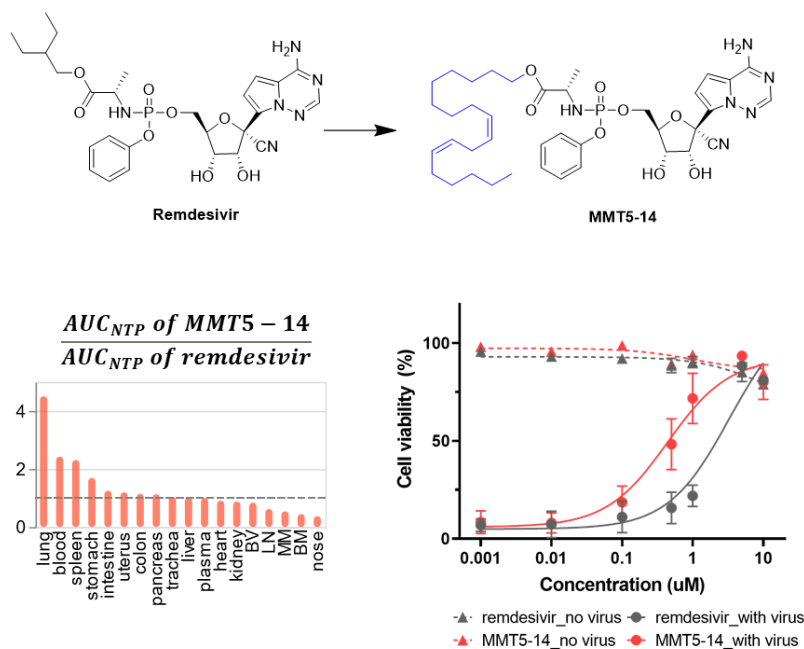


Figure 5.2. Summary of Chapter III

As described in chapter IV (Figure 5.3), *Structure-Tissue Exposure/Selectivity Relationship (STR) May Correlate with Dose-Dependent Clinical Efficacy/Safety*, we investigated the STR, which was correlated with the observed clinical efficacy/toxicity profiles, using a series of clinically approved or tested drug candidates (seven SERMs). These compounds have similar or slightly different structures, molecular targets, and PK profiles in the plasma and tissues. The results showed that drug exposure in the plasma of seven SERMs was not correlated with drug exposure in the target tissues (tumor, fatpad, and bone) in most cases. Drug exposure in the tissues (tumor, fatpad, bone, uterus, and liver), but not in the plasma, was correlated with drug clinical efficacy/toxicity. Three important pharmacokinetic parameters may impact STR, which is often overlooked in lead compound selection during drug development. Drug exposure and the tissue:plasma partition coefficient ( $K_p$ ) determine the absolute amount of drug accumulated in a certain tissue; drug tissue selectivity is a critical parameter for determining the balance among dose, efficacy, and toxicity. In addition, slight structural modification of the compounds altered drug exposure and selectivity in various tissues despite similar drug exposure in the plasma. Tumors exhibit higher drug accumulation than the normal surrounding tissues. These data highlight the importance of the STR in drug optimization and lead compound selection to improve the success rate of clinical drug development.

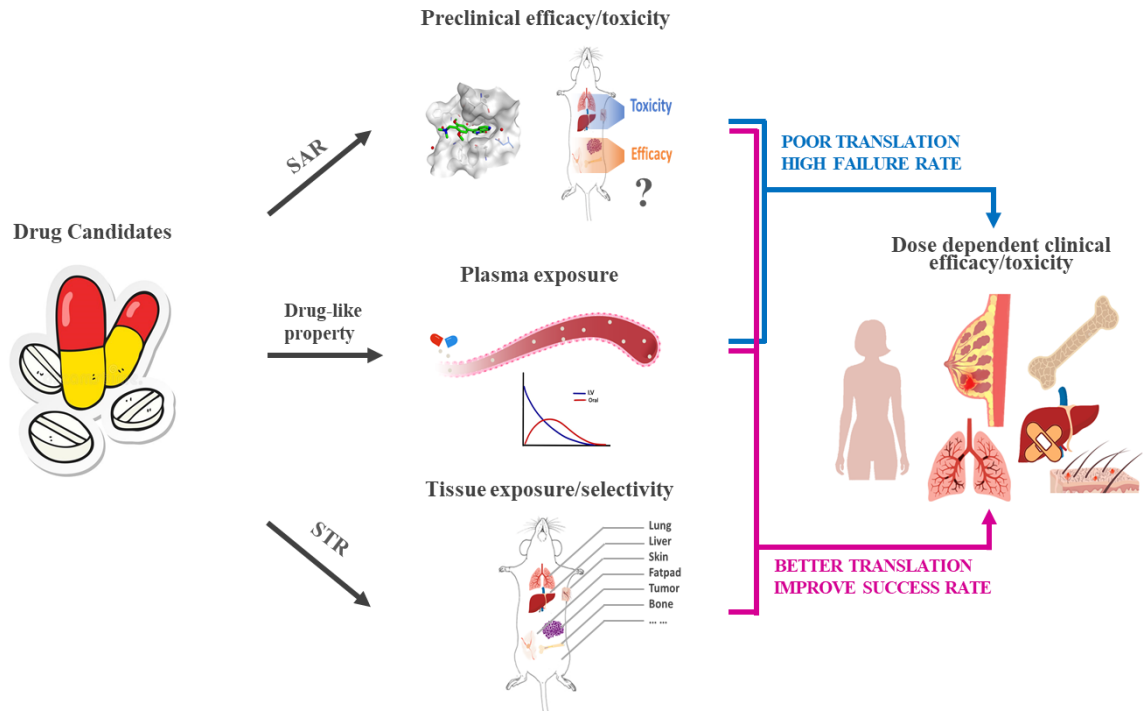


Figure 5.3. Summary of Chapter IV.